technische universität
dortmund

Universitätsmedizin Essen
Westdeutsches
Protonentherapiezentrum (WPE)

Milli, micro, nano: Venturing to small scales in proton beam therapy physics for radiobiological research

DISSERTATION

Zur Erlangung des Doktorgrades
der Naturwissenschaften (Dr. rer. nat.)

Fakultät Physik
Technische Universität Dortmund

vorgelegt von

Carina Behrends
aus Bremen

Düsseldorf, 2023

Von der Fakultät Physik der Technischen Universität Dortmund am 20. Januar 2023 zur Veröffentlichung angenommene Dissertation zur Erlangung des akademischen Grades Doctor rerum naturalium (Dr. rer. nat.).

Erstgutachter:	PD Dr. Christian Bäumer
Zweitgutachter:	Jun.-Prof. Dr. Armin Lühr
Vorsitzender der Prüfungskommission:	Prof. Dr. Marc Aßmann
Vertreter der Wissenschaftlichen Mitarbeiter:	Dr. Ulf Berges
Tag der mündlichen Prüfung:	03. März 2023

Diese Dissertation basiert auf Veröffentlichungen von Teilergebnissen, die zu Beginn der entsprechenden Kapitel explizit kenntlich gemacht sind. Eine Liste der Publikationen ist angehängt.

Abstract

In radiotherapy, it is fundamental to manage the radiation damage in terms of tumor control and normal tissue complications. Thus, therapeutic strategies aim to find a compromise between the applicable dose for clonogenic cell death of the tumor cells and possible side effects. Radiobiological experiments may provide further insight into the damaging effects of radiation.

Here, three different and independent research approaches in proton therapy physics from the millimeter to nanometer scale are introduced to improve radiobiological experiments and thus long-term therapeutic outcome.

The first project presents a method to optimize field shaping in the treatment modality of proton pencil beam scanning in combination with collimating apertures. The fundamental relationship between spot position and aperture edge with respect to the maximization of the dose gradient is investigated in detail analytically, experimentally and in simulations. It has been shown that positioning the outer spots beyond the aperture edge and further combined with fluence modulation can obtain a sharper dose gradient. Thus, a lateral dose fall-off from 80% to 20% of the relative dose profile can be achieved within a few millimeters.

In a second project, an experimental setup is developed and optimized to deliver protons originally accelerated to clinical energies as efficiently as possible with an arbitrary energy down to only a few MeV. The analysis of energy spectra, which are affected by range scattering and fluence loss especially for low-energy protons, shows that there is an optimal material thickness for decelerating protons to a required energy. This allows the provision of proton fields of all energies relevant to radiobiology, especially down to a few MeV with high linear energy transfer and ranges on the scale of 100 µm, for performing radiobiological experiments.

The third project investigates the radiosensitizing effect of platinum nanoparticles (PtNPs) in proton therapy, which can potentially induce increased tumor control during treatment. Promising results have been reported in the use of metal nanoparticles in radiotherapy in terms of increased treatment efficacy. However, the underlying mechanism of the radiosensitizing effect of PtNPs in proton therapy remains unclear. Experiments on tissue-like samples with and without PtNPs have demonstrated no difference on a macroscopic

scale in the stopping power or energy deposition of protons in the presence of PtNPs. Thus, the project provides experimental evidence that the radiosensitizing effect of PtNPs in proton therapy is not due to an enhanced energy deposition, thereby directing the research focus of this effect to the chemical and biological phase of the radiation effect.
Accordingly, the projects investigated in this work provide individual contributions to the radiobiological research and thus to the improvement of the radiation effect in proton beam therapy.

Kurzzusammenfassung

In der Strahlentherapie ist es fundamental den Strahlenschaden im Hinblick auf die Tumorkontrolle und auf Normalgewebskomplikationen zu steuern. Somit müssen Therapieansätze einen Kompromiss zwischen der applizierbaren Dosis für den klonogenen Zelltod der Tumorzellen und möglichen Nebenwirkungen finden. Mithilfe von strahlenbiologischen Experimenten können weitere Erkenntnisse über die schädigende Strahlenwirkung gewonnen werden.

Diese Arbeit stellt drei unterschiedliche und unabhängige Forschungsansätze in der Physik der Protonentherapie von der Größenordnung Millimeter bis zu Nanometer vor, um strahlenbiologische Experimente und damit den langfristigen Therapieerfolg zu verbessern.

Im ersten Projekt wird eine Methode zur Optimierung der Feldformung bei der Behandlungsmodalität von gescannten Protonennadelstrahlen in Kombination mit kollimierenden Aperturen präsentiert. Dabei wird die fundamentale Beziehung zwischen Spotposition und Aperturkante im Hinblick auf die Maximierung des Dosisgradienten im Detail analytisch, experimentell und in Simulationen untersucht. Es hat sich gezeigt, dass die Positionierung der äußeren Spots über den Aperturrand hinaus sowie weiterhin kombiniert mit Fluenzmodulation einen schärferen Dosisgradienten erzielen kann. So kann ein lateraler Dosisabfall von 80% auf 20% des relativen Dosisprofils von wenigen Millimetern erreicht werden.

In einem zweiten Projekt wird ein Versuchsaufbau entwickelt und optimiert, um Protonen, die ursprünglich auf klinische Energien beschleunigt wurden, so effizient wie möglich mit einer beliebigen Energie bis hinunter zu wenigen MeV bereitzustellen. Die Analyse von Energiespektren, die besonders für niederenergetische Protonen von Reichweitenstreuung und Fluenzverlust beeinflusst sind, zeigt, dass es eine optimale Materialdicke für die Abbremsung von Protonen auf eine gewünschte Energie gibt. Damit können Protonenfelder aller strahlenbiologisch relevanten Energien, vor allem runter bis zu ein paar MeV mit hohem linearen Energietransport und Reichweiten im Bereich von 100 µm, zur Durchführung von strahlenbiologischen Experimenten bereitgestellt werden.

Das dritte Projekt untersucht den strahlensensitiven Effekt von Platinnanopartikeln (PtNPs) in der Protonentherapie, der potentiell eine erhöhte Tumorkontrolle bei der Behandlung bewirken kann. Bei der Anwendung von Metallnanopartikeln in der Strahlentherapie sind vielversprechende Ergebnisse im Hinblick auf eine erhöhte Therapieeffizienz bekannt. Allerdings ist der zugrundeliegende Mechanismus des strahlensensitiven Effekts von PtNPs in der Protonentherapie bisher ungeklärt. Experimente an gewebeähnlichen Proben mit und ohne PtNPs haben auf makroskopischer Skala keinen Unterschied im Stoßbremsvermögen oder der Energiedeposition von Protonen bei der Anwesenheit von PtNPs gezeigt. Damit liefert das Projekt den experimentellen Beweis, dass der strahlensensitive Effekt von PtNPs in der Protonentherapie nicht in einer erhöhten Energiedeposition begründet liegt und lenkt dabei den Forschungsfokus des Effekts auf die chemische und biologische Phase der Strahlenwirkung.
Dementsprechend liefern die in dieser Arbeit untersuchten Projekte individuelle Beiträge zur strahlenbiologischen Forschung und damit zur Verbesserung der Strahlenwirkung in der Protonentherapie.

Contents

1. Introduction

Radiation therapy is an important mainstay in the treatment of malignant tumors. Thereby, ionizing radiation is specifically directed onto tumor cells and its destructive effect on the deoxyribonucleic acid (DNA) is exploited. While induced irreversible double-strand breaks may lead to clonogenic tumor cell death, normal tissue cells should be protected as best as possible from the exposure to high-energy radiation.
This damaging effect of ionizing radiation on cells depends mainly on the amount of radiation delivered, i.e. the deposited energy in the tissue. The radiation effects on a biological system consist of a variety of complex physical, chemical and biological processes, which can be described in successive phases [Schlegel et al. (2018)]: Physical interactions of the radiation and the cell's molecules cause chemically altered molecules through ionization or generate damaging free radicals. Interactions of these very reactive free radicals with biomolecules also cause them to change chemically. Biological processes for radiation damage regulation and enzyme reactions induce repair mechanisms, cell divisions or initiate programmed cell death (apoptosis).

The cells of a human body respond to the absorbed dose in different ways, represented by simplified dose-response curves for tumors and normal tissue cells in Figure 1.1. The illustrated biological endpoints, the tumor control probability (TCP) and the normal tissue complication probability (NTCP), approximately show a sigmoid dependence as a function of the absorbed dose [Bentzen (2009); Baumann and Grégoire (2009)]. The optimization of the physical and biological factors affecting TCP and NTCP may enable a wider therapeutic window, increasing the probability of a successful radiotherapy. Thus, an increase of tumor cell killing could be achieved through a more efficacious radiation delivery or a more precise tumor targeting. This procedure, as well as an improved sparing of normal tissue, would reduce the probability of complications in therapy and highlights the substantial need for radiobiological and physical research. This goal is addressed in this thesis in particular for proton therapy.

Proton therapy has its beginnings in the 1950s after Wilson introduced the use of protons in radiation therapy in his pioneering work [Wilson (1946)]. Compared to conventional

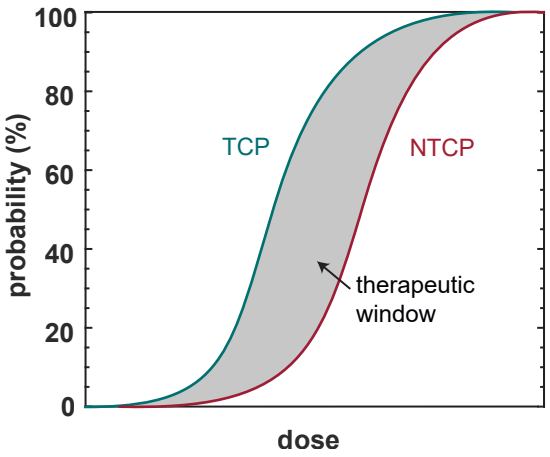

Figure 1.1.: Simplified schematic representation of the dose-response curves for tumors and normal tissue as a function of dose. Tumor control probability (TCP) and normal tissue complication probability (NTCP) are shown as typical endpoints. The gray shaded area between the curves indicates the therapeutic window. Figure based on [Baumann and Grégoire (2009)].

photon-based radiotherapy, whose depth dose distribution follows roughly an exponential decay, the interactions of protons or ions with matter result in a uniform low entrance dose rising to a maximum dose deposition at a characteristic penetration depth, called Bragg peak, followed by a sharp dose fall-off. This allows a dose escalation within the tumor and at the same time sparing of normal tissue, especially beyond the tumor. Already in 1954, the first patient was treated with protons at Lawrence Berkeley Laboratory (Berkeley, California), using the uniform low entrance dose (Section 2.1.4.1) [Lawrence (1957)]. Already in 1958, a fractionated-based therapy concept and proton stopping in the tumor was realized by Tobias et al. (1958). Since then, the number of proton therapy facilities as well as treated patients with protons has increased nearly exponentially, due to the promising physical properties for the radiotherapy [Jermann (2015)].

This work deals with physical challenges on very small scales to improve the radiobiological effect of proton therapy. Following three different research approaches, the efficiency of proton radiation in the tumor and a better sparing of normal tissue is investigated.

The structure of this thesis is the following: Chapter 2 gives an overview of the fundamental aspects of proton therapy. Beginning with the interactions of protons with matter, biological and technical fundamentals are presented.

The first research project deals with the formation of collimated scanned proton fields (Chapter 3). It is studied to what extent the spot position optimization relative to an aperture in the pencil beam scanning technique can sharpen the lateral field gradient. An optimized field design is presented, which achieves lateral penumbras of a few

*milli*meters, allowing for a more targeted dose delivery and better sparing of the normal tissue.

In the second research project (Chapter 4), an experimental setup is developed for performing radiobiological studies with clinical protons at the few-MeV level. The particular challenge consists in the provision of protons with residual ranges in the *micro*meter range, which requires an optimization of the field design. The method developed here allows cell experiments of high radiobiological interest, i.e. experiments with a high linear energy transfer. In this way, important insights into the biological effects of particle radiation can be gained.

The last project presented in Chapter 5 is based on a novel therapeutic approach for tumor control in which the tumor is enriched with metal nanoparticles. Here, the radiosensitizing effect of platinum *nano*particles (PtNPs) in combination with proton radiation is investigated. To analyze the interactions of protons with PtNPs, the protons' energy deposition downstream of tissue-like samples spiked with PtNPs is explored. The local enhancing radiation effect of these high-Z nanoparticles allows the tumor tissue to be treated more aggressively, i.e. leading to a higher TCP.

Each individual project is based on a component of particularly small scale. Therefore, the title *Milli, micro, nano: Venturing to small scales in proton beam therapy physics for radiobiological research* has been chosen for this thesis. All results contribute to the understanding of proton radiation effects, which are summarized in Chapter 6.

2. Principles of proton beam therapy

2.1. Proton interactions in matter

When proton radiation penetrates matter, protons interact with the absorber atoms, resulting in energy loss and scattering due to a variety of mechanisms. Since protons are charged particles, these interactions are dominated by Coulomb fields [Palmans (2015); Newhauser and Zhang (2015); Attix (2004)]: The energy loss is mainly due to Coulomb interactions with atomic electrons, leading to atomic excitation or secondary electron emission (collision loss). Elastic Coulomb interactions due to scattering in the electromagnetic field of the nucleus (Rutherford scattering) deflect the protons and become important for proton energy loss at low kinetic energies. These electromagnetic interactions - collision loss and scattering - occur very frequently and define the proton stopping power as described in Section 2.1.2. Additional to the deceleration process, infrequent energy losses due to non-elastic nuclear interactions result in the generation of secondary particles and a partial loss of the primary protons leading to a slightly attenuated primary proton beam (Section 2.1.3).
Compared to the bound electron, the proton mass and its momentum is high, while compared to heavy ions, it is low. Therefore, protons as projectiles behave physically between electrons and heavy ions. The interaction processes presented below refer to protons with therapeutic energies up to 250 MeV.

2.1.1. Definition of quantities

In order to characterize an irradiation field, the quantity **fluence** Φ is introduced. It is defined as the number of protons $\mathrm{d}N$ per unit area $\mathrm{d}A$, $\Phi = \frac{\mathrm{d}N}{\mathrm{d}A}$. Describing the interactions of protons with matter, the negatively defined mean energy loss $\mathrm{d}E$ per path length $\mathrm{d}x$ is defined as the **linear stopping power** $S = \frac{\mathrm{d}E}{\mathrm{d}x}$. Usually given normalized to the material

mass density ρ, it is the **mass stopping power**

$$\frac{S}{\rho} = -\frac{1}{\rho}\frac{\mathrm{d}E}{\mathrm{d}x}. \tag{2.1}$$

Furthermore, the mass stopping power for charged particles is the sum of the mass electronic stopping power $\left(\frac{S}{\rho}\right)_{\mathrm{el}} = -\frac{1}{\rho}\left(\frac{\mathrm{d}E}{\mathrm{d}x}\right)_{\mathrm{el}}$ due to atomic shell interactions (subscript 'el'), the mass radiative stopping power $\left(\frac{S}{\rho}\right)_{\mathrm{rad}} = -\frac{1}{\rho}\left(\frac{\mathrm{d}E}{\mathrm{d}x}\right)_{\mathrm{rad}}$ caused by emitted bremsstrahlung (subscript 'rad') and the mass nuclear stopping power $\left(\frac{S}{\rho}\right)_{\mathrm{nuc}} = -\frac{1}{\rho}\left(\frac{\mathrm{d}E}{\mathrm{d}x}\right)_{\mathrm{nuc}}$ arising from elastic Coulomb interactions with the nuclei (subscript 'nuc'):

$$\frac{S}{\rho} = -\frac{1}{\rho}\left(\frac{\mathrm{d}E}{\mathrm{d}x}\right)_{\mathrm{el}} - \frac{1}{\rho}\left(\frac{\mathrm{d}E}{\mathrm{d}x}\right)_{\mathrm{rad}} - \frac{1}{\rho}\left(\frac{\mathrm{d}E}{\mathrm{d}x}\right)_{\mathrm{nuc}}.$$

Since the radiative stopping power is only relevant for electrons or extremely high-energetic ions, i.e. not for protons in the therapeutic energy range, only the electronic and nuclear stopping power are described in more detail in Section 2.1.2.

To quantify the local ionization density, which also impacts the biological effect of protons traversing through material, the **linear energy transfer (LET)** is introduced as the restricted linear electronic stopping power, LET_Δ. It describes the mean deposited energy due to electronic interactions of charged particles (Section 2.1.2) - primary protons and secondary particles from the nuclear interactions (Section 2.1.3) - to the material per path length dx minus the energy deposition $\frac{\mathrm{d}E_{\mathrm{ke},\Delta}}{\mathrm{d}x}$ of interactions producing secondary electrons with kinetic energies above an energy limit Δ [International Commission on Radiation Units and Measurements (2014)]:

$$LET_\Delta = \left(\frac{\mathrm{d}E}{\mathrm{d}x}\right)_{\mathrm{el}} - \frac{\mathrm{d}E_{\mathrm{ke},\Delta}}{\mathrm{d}x} = \frac{\mathrm{d}E_\Delta}{\mathrm{d}x}. \tag{2.2}$$

Thus, the LET is restricted to a region around the proton's trajectory, with the radius corresponding to the range of secondary electrons with the energy Δ. If no energy limit is specified ($\Delta \to \infty$, $\frac{\mathrm{d}E_{\mathrm{ke},\Delta}}{\mathrm{d}x} = 0$), all secondary electrons are considered and the LET equals the electronic stopping power.

The **absorbed dose** D is the mean energy dE imparted in a mass element dm,

$$D = \frac{\mathrm{d}E}{\mathrm{d}m},$$

also written as the product of the fluence Φ and the mass stopping power S/ρ:

$$D = \Phi\frac{S}{\rho}.$$

2.1.2. Electromagnetic interactions and energy loss

The energy loss due to electromagnetic interactions occurs when protons penetrate matter. This depends on the relation of the closest distance between the incident proton and the nucleus s to the atomic radius r_{atom}. Thereby, the energy loss scales inversely with the squared distance. If $s \gg r_{\text{atom}}$, the protons transfer a small amount of energy while interacting with the whole atom, leading to atomic excitation or ionization (soft collision). So-called hard collisions with large energy transfer arise when $s \approx r_{\text{atom}}$ holds. In this case, the protons interact with individual electrons, leading to secondary electron ejections, that are important for the definition of the LET (Section 2.1.1) and often known as δ-electrons. The transferred energy to the electrons W can be described by the Rutherford cross section σ differential in energy, $\frac{\mathrm{d}\sigma}{\mathrm{d}W} \propto \frac{1}{E}\frac{m_\mathrm{p}}{m_\mathrm{e}}\frac{1}{W^2}$ [Rudd et al. (1992); Palmans (2015)], with the electron mass $m_\mathrm{e} \approx 511\,\frac{\mathrm{keV}}{c^2}$ and the proton energy E and mass $m_\mathrm{p} \approx 938\,\frac{\mathrm{MeV}}{c^2}$. This relation is obtained from the usual expression of the Rutherford cross section (Equation 2.4). Thus, the cross section as a function of the transferred energy W is higher for lower energetic protons as well as for generating low energetic secondary electrons. The maximum secondary electron energy in a hard collision is given as [Gottschalk (2012); Palmans (2015)]

$$W_{\max} \approx 2m_\mathrm{e}c^2\frac{\beta^2}{1-\beta^2}, \tag{2.3}$$

with the electron rest energy is $m_\mathrm{e}c^2 \approx 0.511\,\mathrm{MeV}$ and the projectile velocity is given in units of the speed of light $\beta = \frac{v}{c}$. This energy transfer is nevertheless relatively low: For a proton energy of 200 MeV, for example, secondary electrons of approximately 256 keV are emitted, which are important for the biological effect (Section 2.2.2). As a rule of thumb, classically speaking, $W_{\max}$ roughly corresponds to $4\left(\frac{m_\mathrm{e}}{m_\mathrm{p}}\right)E \approx \frac{E}{500}$ with the proton energy E, and the mass ratio $\frac{m_\mathrm{e}}{m_\mathrm{p}} \approx 0.0005$.

Beside these two processes of collision loss with the atomic shell, elastic Coulomb scattering at the nuclei defines the nuclear stopping power for $s \ll r_{\text{atom}}$. More precisely, it specifies the scattering of a proton due to the electromagnetic field of the atomic nucleus. In this single scattering process, the proton is changing its direction while losing a very small amount of energy due to the recoil to the nucleus. This recoil energy is negligible for proton energies higher than 1 MeV and is only important at very low proton energies. The single scattering angle is described by the Rutherford cross section,

$$\frac{\mathrm{d}\sigma}{\mathrm{d}\Omega} \propto \frac{Z^2}{E^2}\cdot\frac{1}{\sin^4\left(\frac{\theta}{2}\right)}, \tag{2.4}$$

with the atomic number Z of the target material [Palmans (2015); Rutherford (1911)]. This shows that the scattering cross section, i.e. the probability of proton scattering by the

nuclear Coulomb field into a given solid angle element $d\Omega$, increases with lower proton energy E as well as for smaller scattering angles θ. Since such a single scattering event occurs very frequently and the deflection of the proton is very small, multiple scattering events have to be considered [Gottschalk (2012)]. This so-called **multiple Coulomb scattering** (MCS) is approximated by a Gaussian distribution for the mean scattering angle

$$\theta_0 = \sqrt{\overline{\theta_0^2}(x)} = \frac{14.1\,\mathrm{MeV}}{pv} z \sqrt{\frac{x}{X_\mathrm{R}}} \left[1 + \frac{1}{9}\log_{10}\left(\frac{x}{X_\mathrm{R}}\right)\right] \text{[rad]}, \tag{2.5}$$

where X_R is the material-specific radiation length (Highland formula) [Highland (1975); Gottschalk (2009)]. The mean scattering angle is smaller for a higher projectile velocity v or momentum p (and mass), and increases for a larger thickness x of the absorbing material and with the projectile charge z, which equals 1 for protons. In comparison to other projectiles, the momentum with the high velocity is decisive, which is why carbon ions undergo less scattering than protons.

This Gaussian approximation underestimates the number of single scattering events with larger angles described by Rutherford (Equation 2.4). Taking this large-angle scattering tail into account, more accurate but also more complicated theories of the angular distribution were introduced by Molière [Molière (1948); Gottschalk (2012)] or Goudsmit and Saunderson (1940).

The strength of the protons being scattered away from the initial beam direction is described by the scattering power $T = \frac{\mathrm{d}\theta_0}{\mathrm{d}x}$ [Newhauser and Zhang (2015)]. In analogy to the stopping power, it describes the change in mean scattering angle within a certain material thickness.

Although the electromagnetic interactions with the shell and the nucleus are the most dominant interactions of protons with matter, the nuclear stopping power only contributes at low proton energies ($< 1\,\mathrm{MeV}$) to the proton energy loss. Therefore, the mass stopping power in the therapeutic energy range is approximated by the mass electronic stopping power $\frac{S}{\rho} \approx \frac{1}{\rho}\left(\frac{\mathrm{d}E}{\mathrm{d}x}\right)_\mathrm{el}$.

Based on the first-order Born approximation [Bethe (1930)], the so-called Bethe-Bloch formula expresses the **mass electronic stopping power** for charged particles. Theoretically, the formula is extended by some corrections for very low and very high particle energies, which are described in more detail in Leo (1994), Attix (2004), Bloch (1933), International Commission on Radiation Units and Measurements (1993) and Palmans (2015). For the energy range of proton therapy, the Bethe-Bloch formula can be expressed

as [Palmans (2015); Leo (1994); Gottschalk (2012)]

$$\frac{S_{\mathrm{el}}}{\rho} = \frac{4\pi r_{\mathrm{e}}^2 m_{\mathrm{e}} c^2}{\beta^2} \frac{1}{u} \frac{Z}{A} z^2 \left[\ln\left(\frac{W_{\max}}{I} \right) - \beta^2 \right] \left[\frac{\mathrm{MeV}}{\mathrm{g/cm^2}} \right] \tag{2.6}$$

with the classical electron radius r_{e} , the atomic mass unit u, the atomic number Z and the relative atomic mass of the target atom A, the charge number of the projectile z ($z = 1$ for protons, but note the squared dependence for other ions), the largest possible collision energy transfer to a free electron $W_{\max}$ (Equation 2.3) and the mean excitation energy of the target material I. There is an inverse square relationship of the proton velocity v, contained in the β: If the protons slow down, the stopping power and thus the energy deposition per path length increases strongly, reaching a characteristic depth where the protons lose their entire energy, which explains the Bragg peak (see Section 2.1.4.1 and Figure 2.1 (a)). The absorbing material contribution scales with Z/A to the mass stopping power, as well as with the mean excitation energy I in the denominator of the logarithm. Furthermore, the stopping power depends on the electron density of the material: $n = \frac{Z \cdot \rho}{A \cdot u}$.

2.1.3. Non-elastic nuclear interactions

In contrast to the Coulomb interactions, non-elastic nuclear interactions are of short range. They occur when the proton distance s to the nucleus is approximately equal to or less than the nuclear radius, $s \lesssim r_{\mathrm{nucleus}}$. For this, they must have enough energy to overcome the Coulomb barrier. There is a lower energy limit for the cross section for these interactions to take place, that for biologically relevant elements is about 8 MeV [Newhauser and Zhang (2015); Palmans (2015)]. Here, in contrast to the discussed MCS, the combined effect of elastic scattering events with the nuclei, the kinetic energy is not conserved. This non-elastic nuclear scattering is not included in the nuclear stopping power $\left(\frac{\mathrm{d}E}{\mathrm{d}x}\right)_{\mathrm{nuc}}$ introduced before.

In general, protons are removed from the primary beam during the nuclear interactions, resulting in an attenuated proton beam. At the same time, the nuclei of the material or tissue can change or remain the same under the influence of the protons (the latter, a special case of non-elastic interactions, is called inelastic). A nucleus can release the energy gained by a penetrating proton by the process of nuclear evaporation or an intranuclear cascade. Protons with low initial energies < 10 MeV are absorbed by a nucleus, leaving a highly excited nucleus (compound nucleus), which leads to the emission of particles in the form of evaporation processes. The intranuclear cascade results from the interaction with protons of higher energies, producing a spray of particles, i.e. ejecting high energetic secondary particles, such as protons or neutrons [Palmans (2015); Ipe (2012)].

Besides the emission of particles in the cascade, a lot of excited nuclei are left behind. The

excited nuclei can also evaporate light ions, so protons, neutrons, light fragments (mainly alpha particles), or they relax by an emission of gamma photons (in the following referred to as *gammas*). This evaporation of light ions or the de-excitation of highly excited nuclei happens on short time scales after the proton interaction ($< 10^{-8}$ s), which is why such emitted gamma photons are often called *prompt gammas* [Langen et al. (2015)]. In addition, inelastic proton interactions can lead to radionuclides (unstable isotopes like ^{15}O, ^{11}C, etc.), which decay for example via positron emission (β^+-decay). The following annihilation process will emit two coincident gamma photons of 511 keV. These decay processes are very slow due to the half-lives of the unstable isotopes (order of seconds and minutes).
Both, the 511 keV gammas and the prompt gammas, can be applied for in vivo dose verification: In a positron emission tomography (PET) scanner, the origins of the annihilated gammas and thus the distribution of the primary proton absorption in the tissue can be verified after the treatment. Prompt gamma imaging during a treatment with a slit camera has shown the possibility to obtain prompt gamma detection profiles in dependence of the depth in the patient [Smeets et al. (2012)].

2.1.4. Absorbed dose distribution of proton beams

2.1.4.1. Depth dose distribution

The three interaction processes, stopping, scattering and nuclear interactions, result in a depth dose distribution of protons in matter, the so-called Bragg peak. The depth in a tissue is usually referred to the depth in water, the **water-equivalent depth** (WED) (Section 2.4.1). Figure 2.1 (a) shows the shape of the Bragg peak with characteristic regions [Newhauser and Zhang (2015)]:
The *electronic and nuclear buildup* region is the dose deposition at the absorber surface, when the proton beam penetrates the material. Its characteristic results from the emission of δ-electrons, which emerge due to the ionization processes of the initial proton beam. Since the maximum electron energy corresponds to about 0.2% of the proton energy (Equation 2.3), the range of these δ-electrons in the above calculation example is less than 2 mm in water. Therefore, their dose is deposited close to the surface. As a result, the electronic buildup in the material is usually not detectable. There is also a small increase of the absorbed dose close to the entrance region due to the outcome of the nuclear interaction [Palmans (2015)]. Once protons interact with the material, secondary particles are generated by proton-induced non-elastic nuclear interactions, with a secondary particle equilibrium achieved in the first centimeters. Then, the primary beam has a uniform admixture of secondary particles [Gottschalk (2012)].

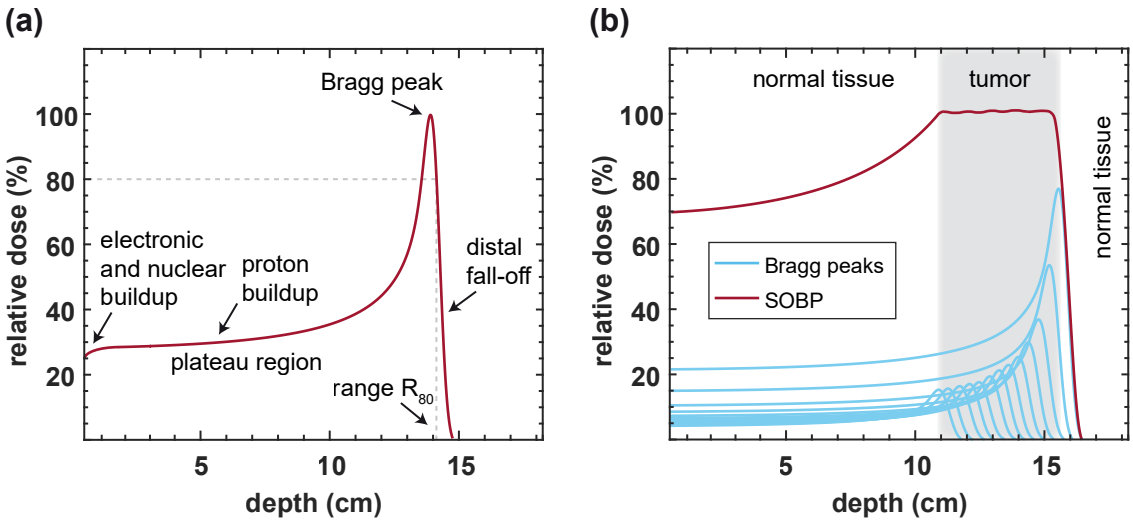

Figure 2.1.: Relative depth dose distributions of a pristine Bragg peak **(a)** and a spread-out Bragg peak (SOBP) **(b)**.

In the *plateau region*, secondary protons continuously contribute to the absorbed dose with the increasing depth, which explains the *proton buildup*. Furthermore, in the plateau, the decreasing primary proton fluence due to nuclear interactions counteracts the increase in the stopping power with depth, due to the inverse square dependence on the velocity of the protons (Equation 2.6). The increasing deceleration process leads to a sharp increase in the energy loss per path length when the protons finally deposit their kinetic energy in the environment. This results in the *Bragg peak*, at the depth of maximum dose deposition. Due to statistical energy loss fluctuations (energy straggling, Section 2.1.4.2) the peak has a certain width in distal direction. This area distal to the Bragg peak is called *distal fall-off*. It is used to define the range of the proton beam, in which not all protons stop at the same depth (range straggling, Section 2.1.4.2). Therefore, the mean projected *range* R_{80} is defined, that is the water equivalent depth at which the relative dose has dropped to 80%, corresponding to about 50% of the fluence. Consequently, the range of a proton beam is defined at the depth where half of the initial protons have stopped. It is therefore independent of the width of the Bragg peak [Paganetti (2012)].
Neglecting the lateral scattering, the mean projected range R_{80} can be numerically approximated by the integral over the energy E of the inverse linear stopping power [Newhauser and Zhang (2015)]:

$$R_{80}(E) = \int_{E} S(E\prime)^{-1} dE\prime. \tag{2.7}$$

In order to cover the tumor with a uniform proton dose, Bragg peaks for different proton energies and intensities are used. The sum of the their deposited doses creates the spread-out Bragg peak (SOBP), whereby the ranges are adapted to the tumor depth and

dimensions. This ensures a dose coverage of the tumor, while sparing normal tissue proximally and distally (Figure 2.1 (b)). The depth extension of the SOBP is called modulation width. This illustrative concept of SOBP with constant range modulation is more commonly used in conventional passive delivery techniques based on beam scattering (Section 2.3.3.1). Modern techniques, where narrow proton beamlets (*spots*) are scanned over the target volume, use the principle of intensity modulation, realized by a fluence modulation in three dimensions over the field (Section 2.3.3.2) [Lomax (2012)].

2.1.4.2. Energy and range straggling

When considering the energy loss of many protons describing the Bragg peak, the mean energy loss is the important property (as the mean range discussed above). But each individual proton interacts multiple times with the matter, which can lead to statistical fluctuations in the energy loss of this proton per path length. Therefore, as mentioned above, the energy loss determining the mass stopping power (Equation 2.1) refers to the mean energy loss of a large number of protons of the same initial energy. The statistical fluctuations thus lead to an energy loss distribution describing the probability of losing a specific amount of energy. This energy loss straggling results in a total range straggling σ_R, leading to a broadening of the Bragg peak. Based on the works of Lewis (1952) and Bohr (1915), the range straggling can be formulated as the variance of the range straggling distribution [Behrends et al. (2021)],

$$\sigma_R^2 = 4\pi n Z e^4 \int_0^{E_0} \mathrm{d}E \left(\frac{\mathrm{d}E}{\mathrm{d}x}\right)^{-3} \frac{1-\beta^2/2}{1-\beta^2}, \tag{2.8}$$

with the number of atoms per unit volume in the absorber n, the elementary charge e, the initial kinetic proton energy E_0, and $\beta = 1 - \left(1 + \frac{E}{m_\mathrm{p} c^2}\right)^{-2} = \frac{v}{c}$, as above. Further, the equation shows an increasing range straggling for a higher kinetic proton energy E, material thickness x and atomic number Z of the absorber material.

Energy spectra The shape of the statistical energy loss distribution varies with the absorber thickness and number of protons: For thin absorbers with a small number of collisions, the distribution has an asymmetrical shape, described by the theory of Landau (1944). Some protons experiencing electromagnetic hard collisions and thus high energy loss produce some high energetic secondary electrons (Equation 2.3). For thick absorbers, there are many individual interactions, so the central limit theorem holds and the energy loss distribution can be approximated by a Gaussian distribution, which is described by Bohr's theory [Bohr (1915); Newhauser and Zhang (2015)]. In general, the energy loss

probability distribution is an asymmetric Landau distribution, whose tail, however, is less pronounced with a large number of protons and thick absorbers. However, while thin or thick absorbers are distinguished in the literature, it is usually not clear to which relative thicknesses the nomenclatures refer. Also, it must be stated whether the energy loss spectrum or the resulting energy spectrum is meant.

For example, Tschalär and Maccabee (1970) and Bichsel and Hiraoka (1989) have described the dependence of the resulting energy distribution as a function of absorber thickness and energy loss as follows: For thin absorbers leading to an energy loss of 20% of the initial energy, the energy distribution can be described by Bohr's theory. Accordingly, it can be assumed that the central limit theorem would be fulfilled. With an energy loss up to 80%, the energy spectrum results in a Landau distribution (correspondingly reversed, since the energy loss spectrum follows the Landau distribution), with increasing asymmetry. An energy loss of more than 80%, where accordingly a very thick absorber must be present, results in a skewed energy distribution [Tschalär (1968)]. This is due to the fact that not all protons contribute to the energy distribution anymore, since they have already lost all their energy and are stopped in the absorber. Such skewed energy spectra become relevant for spectra with very low proton energies (Section 4).

Reconciling the various theories and laws of physics, it is generally found that the shape of the resulting energy spectrum depends strongly on the absorber thickness, the absorber material and on the number of particles. In terms of proton therapy, a beam source can accordingly have a Landau-shaped energy distribution or a Gaussian-shaped one, depending on the number of protons. For a clinical cyclotron, a Gaussian-shaped source is assumed, since the number of initial protons is large. Furthermore, a degraded beam reaches the nozzle, so a Gaussian-shaped energy distribution is applied to a patient when considering the degrader (Section 2.3.2) as a thick absorber. The width of the spectra scales with the material properties and the initial proton energy.

2.1.4.3. Lateral dose distribution and lateral penumbra

Due to the lateral scattering of the proton beam by MCS, the lateral profile of a field is smeared out. At this point Moliere's theory mentioned in Section 2.1.2 becomes important to fully describe this smearing by large scattering angles of protons from hard collisions. While a single pencil beam spot has an approximately Gaussian-shaped intensity profile,

$$s(x) = \frac{1}{\sqrt{2\pi}\sigma_s} e^{-\frac{(x-\mu_s)^2}{2\sigma_s^2}} \left[\frac{1}{\mathrm{m}}\right] \tag{2.9}$$

with the integral normalized to 1 w.l.o.g., the standard deviation σ_s and the mean spot position μ_s, an extended field with uniform dose distribution shows a smeared box-shaped

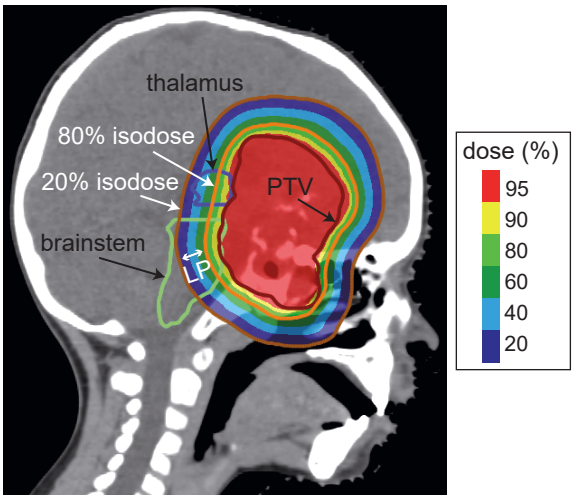

Figure 2.2.: Illustration of the lateral penumbra of an uncollimated treatment field: Sagittal view of a patient with craniopharyngioma. The relative dose distribution is shown by the color washed areas and results from two opposing beams, with one field coming from the view of the observer. The planning target volume (PTV) and the nearby risk organs brainstem and thalamus are shown. The orange line highlights the 80% isodose and the brown line highlights the 20% isodose. The lateral distance between them is defined as the lateral penumbra (white double arrow), which is here about 1 cm. Patient is from the cohort of Bäumer et al. (2021).

profile. The field size is generally defined as the distance between the lateral positions of the 50% isodose of the relative beam profile. The parameter describing the dose fall-off or field shape is the **lateral penumbra (LP)**, which is commonly defined as the distance between the lateral positions of 80% and 20% of the relative field profile [International Commission on Radiation Units and Measurements (2007)]. Figure 2.2 illustrates the LP in a proton dose distribution. The dose protrudes into the nearby organs at risk. This highlights the importance to achieve the sharpest LP as possible in radiotherapy in order to optimally protect surrounding normal tissue from the radiation. The optimization of the LP will be examined in more detail in Section 3 of this thesis. This requires more fundamental theoretical background:

In general, the LP depends on the lateral scattering power of the proton beam. This also includes the scattering in air, which depends on the airgap, i.e. the distance between scattering sources, such as exit window of the delivery nozzle, and the patient or any other absorbing material. Since the lateral scattering also increases with decreasing proton speed, MCS usually has the greatest influence on the LP, especially at larger depths in the patient (Equation 2.5). However, the treatment technique essentially determines the LP, which is why a distinction should be made between passive and active techniques when analyzing the properties in more detail.

In passive techniques, MCS has the largest effect on the LP of the proton beam. In addition to the scattering in the patient, lateral scattering occurs in all components in the beam path, for example for energy modulation, field shaping or monitoring. Collimating apertures are necessary to limit the field laterally (Section 2.3.3.1).
In active techniques, the superposition of Gaussian-shaped spots (Section 2.3.3.2) strongly influences the LP, as there are barely any scattering elements in the beam path. Therefore, a minimal initial spot size, which is commonly associated with σ_s of the Gaussian profile, is advantageous for a small LP. This also makes the LP depending on the initial energy, since the spots are smaller for higher energies due to less lateral scattering. Nevertheless, the scattering in air and in the patient also contribute to the LP.
When comparing the irradiation techniques, it has been shown that the LP of the active technique is mostly inferior to that of the passive collimated technique. However, this depends on the depth in the absorbing material: While the LP of the active technique increases much slower with depth, the LP of the passive techniques is superior at the surface and inferior at greater depths [Safai et al. (2008); Lu and Flanz (2012)].
In current researches - including Section 3 of this work - there are approaches to improve the LP in the nowadays commonly used active delivery techniques: On the one hand, the spacing and weighting of spots is investigated, whereby a higher weighting of the outer ones at the edge of the field is advantageous for a small LP [Winterhalter et al. (2018)]. On the other hand, the combination of the active technique pencil beam scanning (Section 2.3.3.2) with collimating apertures also shows promising improvements of the LP [Bäumer et al. (2019, 2021); Bues et al. (2005); Dowdell et al. (2012); Wang et al. (2015)]. Specifically, the position of the spots relative to the aperture edge is investigated in this work with regard to the LP, whereby and overscanning technique (spot position outside the opened aperture) can further sharpen the LP. Additional details and a description of the whole project can be found in Section 3 of this thesis.

2.2. Biological response of ionizing radiation

Irradiation of living organisms leads to biological reactions with complex mechanisms. The DNA damage caused by the irradiation leads to gene activation and signal transduction in the cell. As a result, there are cellular stress responses, DNA repair mechanisms, cell death, impairments in cell growth or cell cycle. Further parameters like the amount of oxygen in the cell (radiosensitivity increases with oxygen), nutrients or the influence of neighboring tumor cells can also affect the biological response after irradiation [Coleman and Harris (1998)].
From the radiotherapeutic point of view, the crucial question is: Do the irradiated tumor

cells or normal tissue cells survive? To answer this question, the linear-quadratic model describing the fraction of cell survival after irradiation is presented first. It is independent of the radiation type. Afterwards, the biological effectiveness due to the ionization density of different types of radiation is compared.

2.2.1. Cell survival and linear-quadratic model

While cell death can be defined in different ways, in radiobiology it is the loss of the cell's ability to proliferate indefinitely. Most commonly, clonogenic cell death, i.e. the loss of the ability to form at least 50 daughter cells through multiple cell divisions, is used [Herrmann et al. (2006)]. To quantify the radiation response in terms of cell survival, the so-called clonogenic assay is used, which investigates the colony formation after irradiation and provides the cell survival fraction (number of surviving cells over the number of irradiated cells) in terms of the dose. The resulting dose dependent survival curve has a characteristic linear-quadratic shape in a half logarithmic plot and is shown in Figure 2.3 (a). One mathematical description is therefore also called linear quadratic model, which is the model in widespread use [Joiner (2009)]. The data can be fitted according to the function $SF(D) = \exp(-\alpha D - \beta D^2)$. Here the function SF is the survival fraction, D is the dose, α and β are fit parameters specific to the cell type, tissue type and radiation type. In this model, the linear dependence of the dose in the half logarithmic plot, $-\alpha D$, describes the initial slope of the curve, which is based on nearby DNA double-strand breaks from a single radiation interaction. The curvature of the curve is characterized by the quadratic dependence of the dose,$-\beta D^2$, resulting from independent nearby double-strand breaks by two radiation interactions, where each individual hit is sublethal and only the combination of both hits leads to cell death. The shoulder's shape of SF is described by the $\frac{\alpha}{\beta}$-ratio in the unit Gray at which $\alpha D = \beta D^2$ holds, i.e. the linear and quadratic parts contribute equally to cell death (Figure 2.3 (a)) [Herrmann et al. (2006)]. A small $\frac{\alpha}{\beta}$-ratio is associated with a large curvature, i.e. a strongly shaped shoulder, while a large ratio implies a small curvature.

2.2.2. Ionizing density and radiation effectiveness

The large amount of relatively low energetic secondary electrons of short ranges from the electromagnetic interactions of charged particles (Section 2.1.2) influences the biological effect of the ionizing radiation. Thereby, the various types of radiation have a different biological effectiveness, based on the ionization density, which is quantified by the LET (Section 2.1.1): Photons and electrons are sparely ionizing and therefore defined as low LET radiation. Although protons have a higher LET than photons or electrons, they also

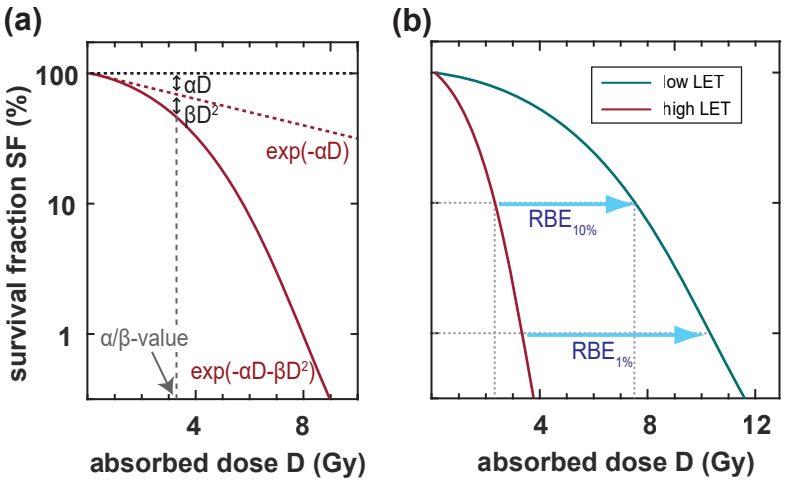

Figure 2.3.: Sketches of cell survival curves illustrating **(a)** the linear-quadratic model and **(b)** the definition of the relative biological effectiveness (RBE).

rate as low LET radiation in the therapeutic range. Densely ionizing radiation, such as heavy charged particles (alpha particles or carbon ions) are considered as high LET radiation.

The LET controls the type of radiation effect that induces a biological damage. Ionizing radiation can induce direct radiation effects, where the energy is absorbed in the target molecule itself, or indirect radiation effects, where the damage occurs through a secondary process involving intermolecular energy transfer. In the indirect effect, radiolysis of water, for example, produces radicals that induce damage via radical reactions in the target molecule. While low-LET radiation produces a uniform dose deposition due to more indirect radiation effects, high-LET radiation is more likely to induce direct radiation effects causing in a locally deposited high dose [Herrmann et al. (2006)]. Based on the simulations of Friedland et al. (2003), indirect radiation effects of protons predominate with respect to the generation of DNA single-strand breaks. This confirms the classification of clinical protons in the low-LET range. Clinical protons with a relatively high LET are produced in Section 4. In addition, the more frequent indirect radiation effects of low-LET clinical protons are discussed in Section 5 of this thesis.

Cell survival curves for a low-LET photon radiation and a high-LET ion radiation are shown in Figure 2.3 (b). Their different radiation effect leads to the **relative biological effectiveness (RBE)** defined as the ratio of the reference dose D_{ref} required for photons and the dose required for ions D_{ion} resulting in the same biological endpoint (isoeffect):

$$RBE = \left.\frac{D_{\text{ref}}}{D_{\text{ion}}}\right|_{\text{isoeffect}}. \tag{2.10}$$

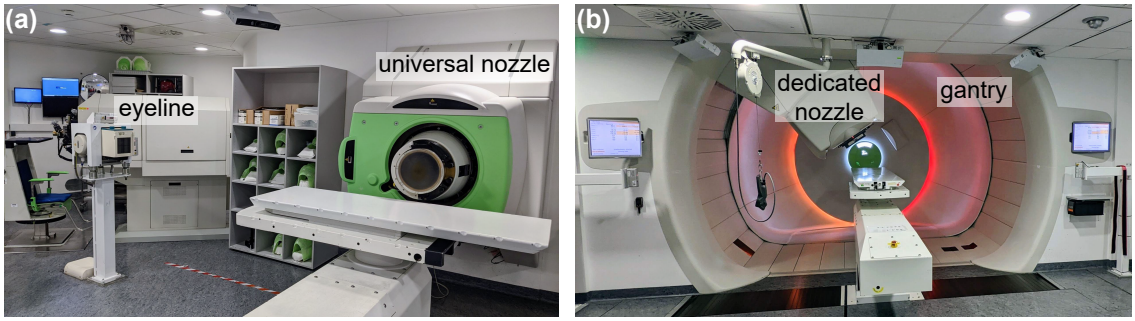

Figure 2.4.: Two treatment rooms of the proton therapy system at WPE: The fixed beam treatment room (FBTR) with the IBA universal nozzle and the dedicated eyeline in **(a)** and a treatment room equipped with a rotatable gantry with dedicated nozzle in **(b)**.

In Figure 2.3 (b), the endpoints of 10% or 1% of the cell survival level are illustrated as examples.

In general, the RBE depends on many factors such as the dose, LET, ion type, biological system and the chosen endpoints. Usually, for proton therapy treatment planning, a constant RBE of 1.1 is used [Heuchel et al. (2022)]. This assumption is made although the RBE increases at the distal end of the depth dose distribution, due to the increasing LET with depth. This makes the RBE a challenging and important measure in treatment planning [Paganetti et al. (2002); Lühr et al. (2018)].

2.3. Beam production and delivery at the WPE

The West German Proton Therapy Centre (WPE, Essen, Germany) is a clinical proton therapy facility equipped with an IBA ProteusPlus proton therapy system (IBA PT, Louvain-la-Neuve, Belgium). It consists of four treatment rooms, one fixed beam treatment room (FBTR) with a horizontal beam direction and three gantry rooms, where the gantry can be rotated by 360° around the patient. There are in total five beam lines, as the eye treatment beam line (in the following called eyeline) is located in the fixed beam room too. This eyeline is similar to the one described in Slopsema et al. (2013). Two of the four rooms have the IBA universal nozzle with the option to mount an aperture. The two other rooms are equipped with the IBA dedicated nozzle.

All rooms operate in the commonly used pencil beam scanning technique (Section 2.3.3.2). Only the eyeline uses the single scattering mode (Section 2.5). Figure 2.4 demonstrates the treatment room with the fixed beam and the eyeline in (a) and a treatment room with a rotatable gantry in (b). These three beam lines (fixed beam, eyeline and the gantry) were used for all measurements described in this thesis.

In the following, beam production and acceleration by a cyclotron, as implemented at

WPE, is described. Furthermore, the beam guiding from the cyclotron to the treatment rooms is presented, as well as the treatment techniques used in this thesis.
There are other possibilities of proton acceleration, for example by a synchrotron or the mechanism of laser-plasma acceleration. The latter is discussed in Section 4.

2.3.1. Isochronous cyclotron

The basic components of the cyclotron are a proton source, a radio frequency (rf) system with an alternating strong electric field to accelerate the protons and a high magnetic field strength for deflection of the protons.
The cyclotron at the WPE is an isochronous cyclotron with a diameter of 4.34 m accelerating protons to a fixed energy of 230 MeV [Ion Beam Applications (IBA) (2018)]. In the center is a hot filament Penning ion gauge source. Electrons are emitted by the hot filament and accelerated. They ionize hydrogen gas by electron impact in a hollow cylinder (Penning effect). The protons of the formed plasma can escape from the cylinder through a slit. If they have the right rf phase, they are accelerated by the electric field of the nearest electrode of the rf system [Schippers (2012)].
At the same time, a large magnetic field strength perpendicular to the particles' motion plane forces the accelerated protons onto a spiral-shaped trajectory due to the Lorentz force

$$\frac{mv^2}{r} = Bqv \overset{v=\frac{2\pi r}{T}}{\Longrightarrow} T = \frac{2\pi m}{qB}, \tag{2.11}$$

with the proton mass m, the magnetic field strength B and the proton charge $q = ze$. Since the orbital period T is independent of the proton beam radius r and the proton velocity v, all protons move on their circular path in the cyclotron on a line with the same azimuthal angle [Schippers (2012)]. In the azimuthal direction, the magnet has a varying thickness of four twisted pancake-shaped *hills* and *valleys* (more details below).
The proton acceleration system of the cyclotron is based on four cavities, which requires two copper high-voltage electrodes (*dees*) placed diametrically in opposite valleys of the magnet. These dees are mounted on copper pillars and, together with additional copper sheets on the valley walls (*counter dees*), they form the cavities in which rf currents are generated: The resonance frequency of the cavities is approximately 106 MHz, which corresponds to the 4^{th} harmonic of the proton orbital frequency. This accelerating voltage (here 60 kV) has to be synchronized to the azimuthal proton positions for all radii. The resulting alternating polarity of the high voltage supply causes currents flowing back and forth in the cavity. The protons experiencing this electric field are accelerated strongly in each of the four acceleration gaps between the dees and counter dees, whereby each dee consists of an upper and a lower part at the same electric potential. Also, the volumes

between the two dees are at ground potential, providing field-free areas, and making a polarity reversal straightforward [Schippers (2012, 2015)].
Taking into account the relativistic mass increase at proton velocities close to the speed of light (larger radii), the magnetic field strength increases radially from the central part of the cyclotron to the outside, enabling a constant rf and a uniform beam current. This is implemented by a decreasing distance between the magnetic poles towards the outer parts. However, the radially increasing magnetic field strength leads to vertical defocusing of the proton beam. Therefore, the hills and valleys at the poles are shaped such that a focusing followed by a defocusing force acts on the protons in a horizontal plane. Since the magnitude of the focusing force decreases with the radius, the hills and valleys as well as the dees have to be wing-shaped. These technical details ensure a vertically stabilized proton beam [Schippers (2012)].
For example, an applied voltage of 60 kV and four acceleration gaps add 240 keV per cycle to the protons' energy, so they need about 1000 cycles to reach their maximum energy of 230 MeV.
Afterwards, the protons are extracted from the cyclotron. A so-called *septum* is used to deflect the proton beam from its circular path by means of a strong radial electric field. In terms of charge carriers per time, proton currents up to 500 nA can be achieved [Ion Beam Applications (IBA) (2018)].

2.3.2. Ion-beam guiding to the treatment rooms

Since the isochronous cyclotron provides a proton beam of constant 230 MeV, the beam energy has to be reduced to the desired treatment energy. This is done with an external energy selection system. A continuous degrader consisting of a rotating cylindrical graphite (alternatively beryllium) absorber with variable thickness is used to adopt the proton energy for clinical application between 100 and 230 MeV. A collimator and slits confine a diverging beam [Ion Beam Applications (IBA) (2018)].
After the energy selection system, the beam is guided by the so-called beam line to the treatment rooms. The beam line consists of a vacuum chamber, some stainless steel tubes as well as quadrupole and dipole magnets to focus and bend the proton beam. A shaped and collimated beam with well defined parameters such as energy, energy and angular spread, spot size and intensity at the beam exit in the treatment room is of particular importance for the precise application of the field and therefore the dose to the patient's tumor.

2.3.3. Beam delivery techniques

After the beam is guided to the treatment room, it is applied to the patient using passive or active delivery techniques.
For passive techniques, the beam is laterally scattered. In addition, the depth coverage is provided by a rotating modulator wheel, which changes the energy in small steps leading to a uniform dose distribution in the SOBP (Figure 2.1 (b)). A passive modality is single scattering, in which the beam is sufficiently scattered laterally while the modulator wheel rotates so quickly that each depth is applied several times sequentially. Thus, the total dose is applied in all three dimensions simultaneously. Typically, passive techniques are combined with patient specific apertures and compensators to shape the field laterally and in depth. However, due to the field size, wedges instead of compensators are usually used for the single scattering techniques (see below).
An active technique is pencil beam scanning (PBS), in which the target is "painted" with a pencil beam. In the following, single scattering and pencil beam scanning will be discussed in more detail, as they are used in this work.

2.3.3.1. Single scattering technique

For the single scattering technique, the initial Gaussian-shaped beam is expanded by a single flat scatterer. Therefore, the technique is used for small targets (eyeline in WPE). To irradiate eye tumors and thus superficial tumors, the proton energy from the cyclotron has to be degraded, here at the eyeline to 82.5 MeV. Lucite (polymethyl methacrylate) or tantalum scattering foils spread the beam laterally. Upstream of the scatterer, exchangeable range modulator wheels create an SOBP that extends to the surface. By mounting an additional absorber of brass (*stop block*) upstream, the SOBP can be limited in proximal direction (Figure 2.5). With the various wheels, ranges (at which the dose has dropped to 90%) of $R_{90} = 35\,\text{mm}$ to $R_{90} = 5\,\text{mm}$ can be achieved. This corresponds to an energy range of approximately 22 MeV to 65 MeV. For a laterally confined beam, apertures adopted to the patient's tumor are mounted downstream. To create a sharp field, a major part of the beam is blocked, resulting in a low efficiency.
There are three commissioned wedges made of polymethyl methacrylate (PMMA) at the WPE, which can additionally be used for beam shaping [Wulff et al. (2023)].

2.3.3.2. Pencil beam scanning technique and apertures

The active delivery technique pencil beam scanning (PBS) scans a pencil beam in three dimensions across the target volume utilizing dipole magnets (Figure 2.6). A pencil beam

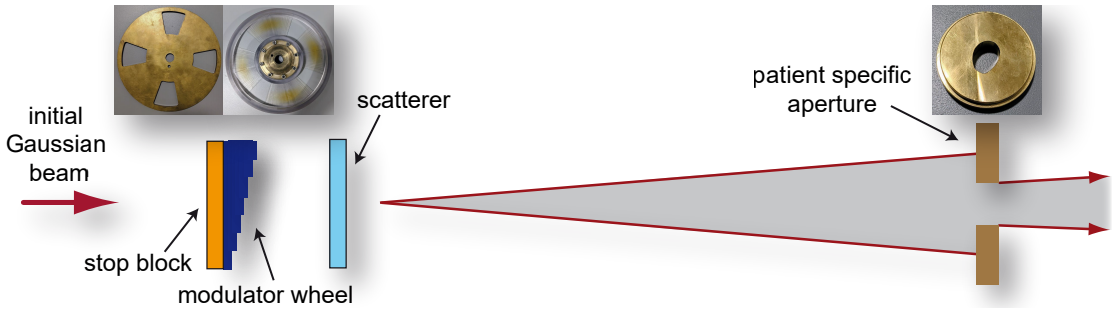

Figure 2.5.: Principle of the single scattering technique. The depth profile of an initial Gaussian-shaped beam is formed with an exchangeable range modulator wheel and an exchangeable stop block. Then the beam is laterally scattered. More downstream, the beam is laterally confined by an aperture. A more detailed description is in the main text. In addition to the sketch, photos of a stop block, a modulator wheel and a patient specific aperture are given.

emerging from the beam line already has an energy corresponding to the desired penetration depth. In contrast to the passive techniques, the energy is adjusted with the energy selection system at the cyclotron. The Gaussian-shaped spots (Equation 2.9) are then scanned laterally over the tumor volume in discrete steps using a fast-scanning and a slow-scanning dipole magnet orthogonal to the beam direction (Figure 2.6). With this principle, the so-called *step and shoot* technique can be operated, which is used at the WPE. During treatment planning, the tumor volume is divided into depth layers, which are commonly applied from the back to the front, i.e. starting with the highest energy. A scanning control system optimizes the treatment time by reordering the spot pattern in each layer from the irradiation plan. The depth modulation of the dose is again achieved by modulating the proton energy. Here, the energy switching time is an important factor, as it influences the treatment time, but also the homogeneity of the dose if the patient moves [Paganetti (2016)]. For superficial tumors, the energy can additionally be decreased with the help of a range shifting block (short: range shifter, usually made from PMMA), which is mounted in the snout. Furthermore, a collimating aperture can be additionally mounted to the snout to sharpen the lateral penumbra (Section 2.1.4.3). Since a combination of the PBS with an aperture is the basis for the project in Section 3 of this work, a typical aperture is added optionally in Figure 2.6.

The biggest advantage of the PBS technique is the optional intensity modulation that is commonly used today, the so-called intensity modulated proton therapy (IMPT). In contrast to a single field uniform dose (SFUD) concept, where each contributing field provides an individual homogeneous dose distribution to the overall homogeneous dose distribution, IMPT exploits another degree of freedom: the cross-field fluence profile modulation for each field [Lomax (2012)]. Each spot's position and intensity is optimized, resulting in a single field having an inherently inhomogeneous dose distribution.

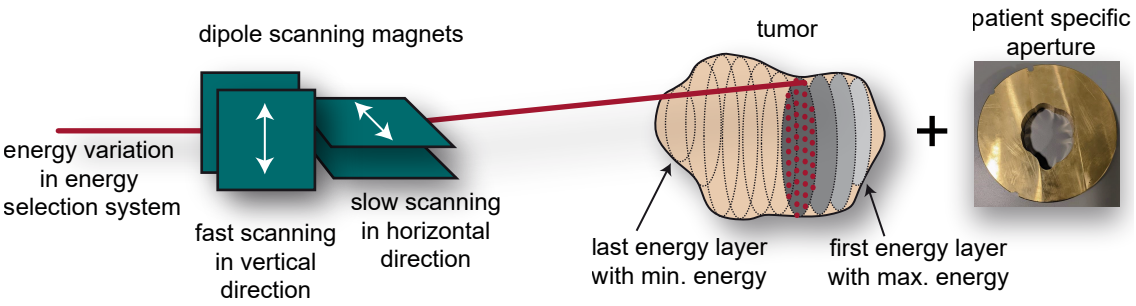

Figure 2.6.: Principle of the pencil beam scanning (PBS) technique. A fluence modulated pencil beam is scanned laterally across the target volume in multiple energy layers. The optional aperture is illustrated as a photo of a patient specific aperture [based on Krämer and Durante (2010)].

Only the combination of all contributing beams guarantees an overall homogeneous dose delivery. The three-dimensional fluence modulation makes IMPT a flexible and powerful tool to confine the radiation to target volume, as long as there is no movement of the patient between the application of the fields. As a side effect, due to intensity modulation, there is no classical SOBP as illustrated in Figure 2.1 (b) for an IMPT field.

2.4. Computational tools for proton transport

This chapter provides a brief introduction to the useful concepts of proton transport computation for proton therapy. This includes the simple, but important and frequently used concept of water-equivalent thickness. It also introduces the basic principle of a Monte Carlo simulation, which nowadays is the state-of-the-art computation method in an ion beam therapy treatment planning system (TPS).

2.4.1. Water-equivalent thickness

As already mentioned in Section 2.1.4.1, the penetration depth of protons into a material and thus the specified range is commonly given for a water equivalent. Water represents a tissue very well and is recommended as the reference medium in dosimetry for tissue-like phantoms or the characterization of detectors [International Atomic Energy Agency (IAEA) (2000)]. Therefore, the so-called **water-equivalent thickness** (WET) is used for the definition of radiological depths. Based on Zhang and Newhauser (2009), the WET of a material, WET_{mat}, is defined as follows [Newhauser and Zhang (2015)]:

$$WET_{\mathrm{mat}} = h_{\mathrm{H2O}} = h_{\mathrm{mat}} \frac{\rho_{\mathrm{mat}}}{\rho_{\mathrm{H2O}}} \frac{\overline{S_{\mathrm{mat}}}}{\overline{S_{\mathrm{H2O}}}}. \tag{2.12}$$

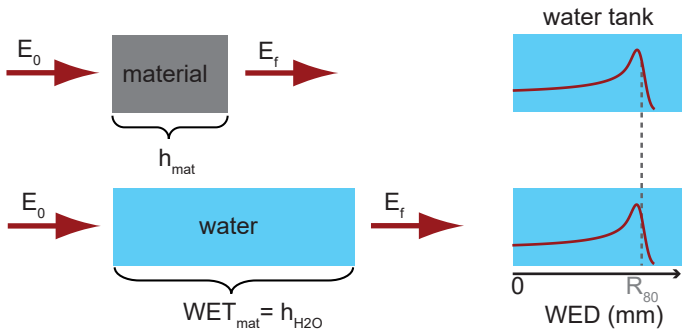

Figure 2.7.: Concept of the water-equivalent thickness (WET) and water-equivalent depth (WED) [based on Zhang and Newhauser (2009)]. The initial energy E_0, the final energy E_f, the thickness of the material h_{mat} and the water thickness h_{H2O} are relevant properties.

Here, h is the physical thickness, ρ the density and $\overline{S}$ the mean proton mass stopping power defined by $\overline{S} = \frac{\int_E S dE}{\int_E dE}$. The subscripts 'mat' and 'H2O' denote the used variables for a specific material and water, respectively. The concept is illustrated in Figure 2.7. For radiologically thin materials, with a low proton energy loss in the material, the WET can be simplified to

$$WET_{mat} = h_{H2O} = h_{mat} \frac{\rho_{mat}}{\rho_{H2O}} \frac{S_{mat}}{S_{H2O}} \tag{2.13}$$

with the mass stopping powers S_{mat} and S_{H2O} for the energy of the initial protons (Section 2.1.1) [Zhang and Newhauser (2009); Newhauser and Zhang (2015)].
Experimentally, the WET of a material is usually determined as the difference of the measured ranges in water with ($R_{80,mat}$) and without material ($R_{80,no\ mat}$) in the beam path:

$$WET_{mat} = R_{80,no\ mat} - R_{80,mat}. \tag{2.14}$$

While the WET describes the radiological thickness of beam line objects or detectors, the corresponding WED is specified for the water depth. The WED is applied, for example, to characterize a depth dose curve (DDC), or the penetration depth in a phantom or a patient. Therefore, the important concept of WET or WED is used for the quality assurance and dosimetry. There is the need for reliable methods to compute and measure the quantities. In clinical practice, a WET is traditionally measured by the range shifted in water due to presence or absence of the material in the beam path. Overall, it can be found from Equation 2.12 that the WET depends on the proton's energy, as well as on the thickness and type of the material of interest.
For the comparison of different computational or measurement methods, it is also common to specify the **water-equivalent ratio** (WER) of a material [Zhang and Newhauser

(2009)]. It is the ratio of WET_{mat} related to the physical thickness h_{mat}:

$$WER_{\text{mat}} = \frac{h_{\text{H2O}}}{h_{\text{mat}}} = \frac{R_{80,\text{no mat}} - R_{80,\text{mat}}}{h_{\text{mat}}} = \frac{WET_{\text{mat}}}{h_{\text{mat}}}. \tag{2.15}$$

These concepts of WET and WER are used in the projects in Section 4 and Section 5.

2.4.2. The Monte Carlo method

The use of Monte Carlo simulations in the field of medical physics has increased rapidly during the last 50 years [Rogers (2006)]. The power of Monte Carlo methods results from statistical approaches that solve, for example, radiation transport problems. Related to the application of proton transport computations, the Monte Carlo method uses probability distributions of microscopic interactions to describe protons in matter. Based on the interaction cross sections, the interaction length and mean free path length is modeled for each infinitesimal step for the proton path through matter. To do so, generated random numbers applied on probability density functions are utilized [Agostinelli et al. (2003); Wulff (2010); Geant4 (2020)]: This sequence of random steps with statistical events of the initial protons and generation of secondary particles proceeds until the energy of the particles is below a cut-off value. At that point, the particles stop in the material and deposit their remaining energy. Quantities such as the dose distribution, the LET or energy spectra can then be calculated via a numerical integration. A sufficiently large number of primary particles is needed to achieve a specific statistical uncertainty.
Monte Carlo methods are more accurate than analytical models, since the latter require more approximations. Therefore, a TPS in proton therapy nowadays also usually calculates the dose using Monte Carlo simulations.
In general, a Monte Carlo simulation tool involves a beam source model, the treatment head, and a phantom (patient) or detector. The proton source parameters implemented in the beam model are mostly determined by measurements. Any implemented range shifter or aperture is important for modeling the treatment head. A detector or phantom can be divided into arbitrary small steps, defining a scoring grid.
Briefly speaking, a computed tomography (CT) image of the patient is performed and imported into the TPS. The geometry of the patient is divided into voxels of an appropriate resolution. For each voxel, the CT number given in Hounsfield units (HU) is converted into a mass density via a calibration curve and also into a proton stopping power. The dose of charged particles is calculated using the Bethe-Bloch formula (Equation 2.6), whereby the proton transport through the patient geometry is based on the above discussed statistical Monte Carlo method.

3. Project *milli*: Optimization of collimated proton pencil beam positions

For the investigation of the lateral shape of proton fields, this project deals with observable scales in the *milli*meter range, the typical size for a lateral penumbra in proton pencil beam scanning as illustrated in Figure 2.2 [Safai et al. (2008); Bäumer et al. (2018)]. Thereby, the application of a static or dynamic collimator offers more options for the field shaping. This requires optimization of the collimator shape as well as the spots to be optimized with respect to a fluence modulation and its positioning relative to the aperture edge [Winterhalter et al. (2018)].

This thesis project deals with the optimization, i.e. the minimization, of the LP of proton fields in pencil beam scanning with an additional collimating aperture. For this purpose, the effect of the spot position with respect to the aperture edge in terms of dose fall-off is investigated in detail analytically, experimentally and *in silico*. First, from a theoretical side, two different analytical approaches are introduced in Section 3.2 to study the dose profile for various positions of one spot hitting the aperture edge in air. These analyses of the single spot in air are validated by measurements with radiochromic films on a clinical pencil beam scanning beam line. Further comparison with Monte Carlo simulations in the Geant4 TOol for PArticle Simulation (TOPAS) [Perl et al. (2012)] as well as in the TPS RayStation (RaySearch Laboratories, Stockholm, Sweden) is presented in Section 3.3.1. Further *in silico* investigations on the field shape of one collimated spot as a function if its position are performed in water, for different energies and using a clinical range shifter. In addition, two-dimensional spot pattern configurations with different spot positions to the aperture edge are simulated with respect to the LP (Section 3.3.2). The results of the experiments and simulations of a single spot in air (Section 3.4.1) confirm the theoretical analysis. A benefit from spot positioning beyond the aperture edge, here called overscanning, in terms of LP is found. Further simulations of the profiles in water are given (Section 3.4.2), as well as an analysis of two-dimensional fields in Section 3.4.3. These *in silico* investigations indicate a further potential of overscanning in combination

with fluence modulation. Overall, the spot overscanning method improves the lateral field shaping. Such sharper dose profiles spare potentially organs at risk.
The methods and results of this project are presented in an own publication on this topic, which is referred to once at this point to avoid frequent citations in the text below:

Behrends et al. (2023), *Optimization of proton pencil beam positioning in collimated fields, Medical Physics, accepted and online available, 2023.*

3.1. Introduction to collimated proton fields

High conformality of proton fields is particularly important to spare the surrounding tissue during radiotherapy. A disadvantage of the characteristic depth dose distribution of protons (Section 2.1.4.1) with the targeted dose deposition in the Bragg peak are range uncertainties, whereby the maximum dose could be inadvertently deposited distal to the tumor. This is coupled to an increased proton LET with depth and the consequent increased RBE distal to the Bragg peak (Section 2.2.2). Because of these difficulties, the optimization process in treatment planning seeks field designs that avoid proton stopping directly in front of an organ at risk or restricts these field arrangements appropriately. As a consequence, organs at risk are more often located laterally to the beam propagation direction, requiring a sharp lateral dose profile, i.e. a small LP.
In pencil beam scanning (Section 2.3.3.2), a field consists of overlapping spots, whose lateral dose profile is commonly approximated by a Gaussian function (Equation 2.9). The LP of a PBS field is generally determined by the initial spot size, the lateral scattering by MCS in the material or in the patient and by the influence of optional beam shaping devices in the nozzle, like a range shifter or an aperture. However, PBS offers further benefits for optimization, for example, the fluence modulation in IMPT compared to passive application techniques. Safai et al. (2008) found that the LP of passive techniques using a field shaping aperture is mostly superior to that of active techniques. These observations suggest the combination of PBS with a collimating aperture. It has proven to be beneficial for the LP when combining PBS with apertures or multi-leaf collimators [Bäumer et al. (2019, 2021); Bues et al. (2005); Dowdell et al. (2012); Wang et al. (2015); Tominaga et al. (2022)]. Related to this work, there are some approaches to improve the lateral dose fall-off of PBS with apertures in proton therapy. For example, Bäumer et al. (2018, 2019) have shown that some mechanical hardware modifications concerning the order of aperture and range shifter in the treatment head can be beneficial for the LP. Further, Winterhalter et al. (2018) pointed out that a fluence modulation, more precisely a higher weighting of the spot placed on the aperture edge (*edge enhancement*), is advantageous for the LP.

Overall, this highlights that the LP in PBS fields with aperture can be influenced by a variety of aspects, not all of which have been investigated or optimized so far. One of these aspects is the reduction of the LP by spot position optimization relative to the aperture edge, which is addressed in this project by theoretical considerations, experiments and simulations.

3.2. Analytical approaches of lateral penumbra optimization

The lateral one-dimensional dose profile of a PBS spot can be described by the Gaussian function (Equation 2.9). Based on Sabbas et al. (1987), the profile of a collimating aperture edge at its downstream end can be described by the Heaviside function

$$h(x) = \begin{cases} 1 & x \leq 0 \\ 0 & x > 0 \end{cases}. \tag{3.1}$$

The collimation effect on the spot is mathematically described by the multiplication of the spot profile $s(x)$ with the aperture profile $h(x)$ [Sabbas et al. (1987); Hong et al. (1996); Safai et al. (2008)]. To model the profile in a more downstream plane, it is convolved with the Gaussian-shaped lateral spread

$$a(x) = \frac{1}{\sqrt{2\pi}\sigma_\mathrm{a}} e^{-\frac{(x-x_\mathrm{mean})^2}{2\sigma_\mathrm{a}^2}}, \tag{3.2}$$

which includes, for example, the scatter due to the intrinsic angular confusion of the beam. The mean lateral position is denoted by x_mean and the standard deviation σ_a approaching typical beam optics in PBS. These definitions lead to the mathematical expression of a collimated lateral spot profile

$$p(x) = (s(x) \cdot h(x)) * a(x), \tag{3.3}$$

with the convolution expressed by the arithmetic symbol $*$. With respect to the optimization of spot positions in PBS with an aperture, this chapter provides two analytical approaches using Equation 3.3 regarding the resulting LP. Since the mathematical operation of convolution is inconvenient for an analytical consideration and $h(x)$ is a non-differentiable step function, both approaches make use of a simplification: While the non-differentiable function $h(x)$ in Approach A (Section 3.2.1) is estimated by an error

function with small standard deviation, Approach B (Section 3.2.2) describes the convolution over the width of the resulting profile as a quadratic addition of both widths. The latter assumption would only be completely correct for the convolution of two Gaussian functions.

3.2.1. Approach A: The analytical beam approach

The inversely proportional lateral gradient of a dose profile is used below as a measure to describe the LP. This is founded on the numerical definition of a gradient and the linear approximation of the profile in this range. For the gradient $p\prime(x)$ of the collimated spot profile $p(x)$ this gives

$$LP = \frac{(0.8-0.2)}{p\prime(x_\mathrm{c})}, \tag{3.4}$$

with the profile p reaching 50% at $x = x_c$, the most representative position within the LP, since the side facing the closed aperture:

$$p(x = x_\mathrm{c}) = 0.5. \tag{3.5}$$

It is worth mentioning that the position x_c depends on the spot position μ_s. Figure 3.1 (a) illustrates these defined quantities.
Considering the objective of this project, optimizing the spot position to minimize the LP, the mathematical optimization problem translates into maximizing the gradient of the dose profile $p(x)$ and is written as:

$$\underset{\text{over}\,\mu_\mathrm{s}}{\text{maximize}} \left\{ \mathrm{D}\left[(s(x,\mu_\mathrm{s}) \cdot h(x)) * a(x) \right] \right\}. \tag{3.6}$$

Here, the differential operator D acts on the resulting profile of Equation 3.3. The mathematical conversion $\mathrm{D}\left[(s(x,\mu_\mathrm{s}) \cdot h(x)) * a(x) \right] = \mathrm{D}\left[s(x,\mu_\mathrm{s}) \cdot h(x) \right] * a(x)$ reduces the optimization to maximizing the gradient $\mathrm{D}\left[s(x,\mu_\mathrm{s}) \cdot h(x) \right]$.
The non-differentiable function $h(x)$ is approximated by the error function with standard deviation σ_h, modeling the aperture profile in a plane further downstream (subscript 'ds') [Sabbas et al. (1987); Hong et al. (1996); Safai et al. (2008)]:

$$h_\mathrm{ds}(x) = \frac{1}{2}\left(1 - \mathrm{erf}\left(\frac{x}{\sqrt{2\sigma_\mathrm{h}^2}}\right)\right). \tag{3.7}$$

Therefore, the propagated spot profile in a plane further downstream is represented by $p_\mathrm{ds}(x) = s_\mathrm{ds}(x,\mu_\mathrm{s}) \cdot h_\mathrm{ds}(x)$. This describes any plane further downstream, according to the strength of aperture smearing and spot broadening, due to the propagation. The latter is

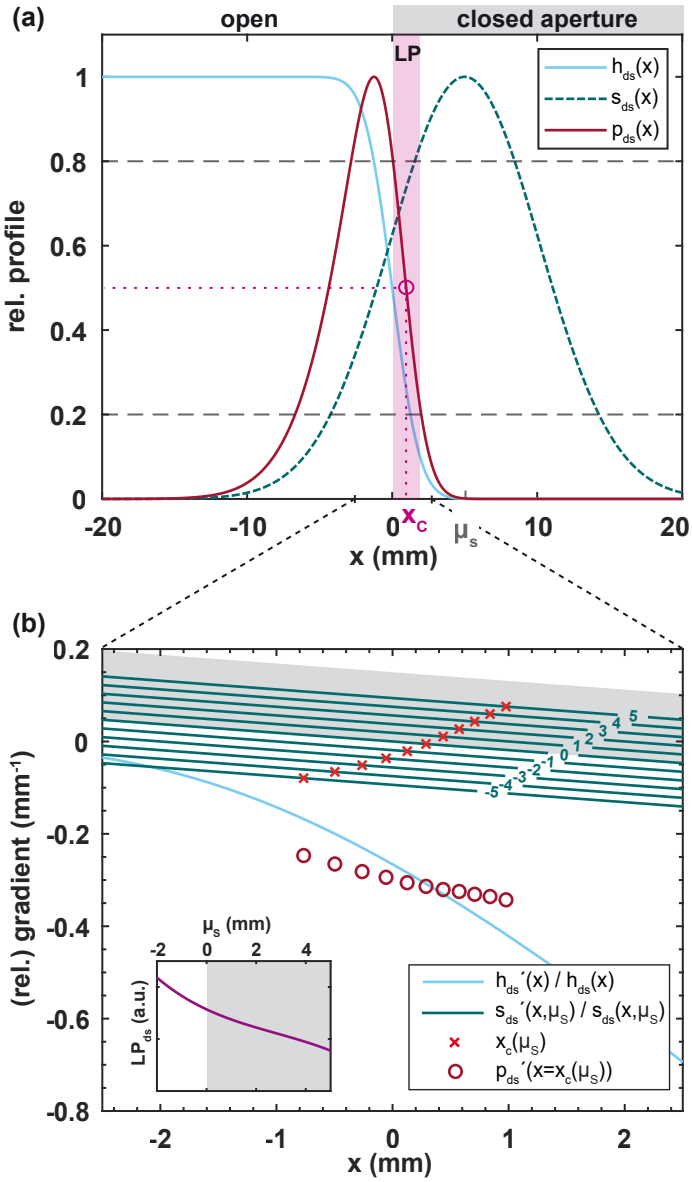

Figure 3.1.: Illustration of Approach A: In **(a)**, the one-dimensional profiles of the aperture edge as an error function $h_{\mathrm{ds}}(x)$ with $\sigma_{\mathrm{h}} = 1.5\,\mathrm{mm}$, the Gaussian-shaped spot profile $s_{\mathrm{ds}}(x)$ with $\sigma_{\mathrm{s}} = 5.2\,\mathrm{mm}$, and the profile $p_{\mathrm{ds}}(x)$ as a product of the former are given. The analysis of the gradient $p_{\mathrm{ds}}\prime(x)$ and the resulting lateral penumbra LP_{ds} as a function of different spot positions μ_{s} are visualized in **(b)**. To examine the influences of a varying spot position in detail, the contributions of the addends from Equation 3.10 are shown as separate relative gradients, as well as the total gradient $p_{\mathrm{ds}}\prime$. The effect of the spot comes from the first addend, which yields a straight line as a function of the spot position, illustrated as a series with varying μ_{s} values denoted in mm on the green lines. According to the μ_{s} values, the locations $x = x_{\mathrm{c}}$, where the gradient equals 50%, are marked by the red crosses. The gray shaded area indicates the closed aperture area. The second addend of Equation 3.10 is shown in light blue and represents the influence of the aperture on the gradient of the profile. The latter is marked by the dark red circles as a function of different x_{c} values for different spot positions μ_{s}. The inset provides the resulting values for the LP in dependence of the spot position, with the gray area again marking the closed aperture. Figure based on Behrends et al. (2023).

denoted by $s_{\mathrm{ds}}(x, \mu_s)$. However, here this is mentioned for consistency and any change in lateral spot position μ_s due to beam divergence in air is neglected for simplicity. It seems reasonable that these profiles defined downstream of the aperture comprise a small contribution from the lateral spread $a(x)$. This assumption is not necessarily true, since $h_{\mathrm{ds}}(x)$ is utilized only for differentiability with much smaller σ_h than σ_a and $a(x)$ is eliminated from the gradient expression.

This leads to the maximization problem of the gradient from Equation 3.6:

$$\underset{\text{over}\,\mu_\mathrm{s}}{\text{maximize}} \left\{ \mathrm{D}\left[s_{\mathrm{ds}}(x, \mu_\mathrm{s}) \cdot h_{\mathrm{ds}}(x) \right] \right\}. \tag{3.8}$$

Furthermore, following the condition in Equation 3.5, the profile becomes

$$p_{\mathrm{ds}}(x) = s_{\mathrm{ds}}(x, \mu_\mathrm{s}) \cdot h_{\mathrm{ds}}(x)\big|_{x=x_\mathrm{c}(\mu_\mathrm{s})} = 0.5. \tag{3.9}$$

The gradient, now written as $p_{\mathrm{ds}}{}'(x) = \mathrm{D}\left[s_{\mathrm{ds}}(x) \cdot h_{\mathrm{ds}}(x) \right]$, remains to be maximized for the optimization problem when varying the spot position μ_s, which results in

$$\begin{aligned} p_{\mathrm{ds}}{}'(x) &= 0.5 \left(\frac{s_{\mathrm{ds}}{}'(x, \mu_\mathrm{s})}{s_{\mathrm{ds}}(x, \mu_\mathrm{s})} + \frac{h_{\mathrm{ds}}{}'(x)}{h_{\mathrm{ds}}(x)} \right) \Bigg|_{x=x_c(\mu_s)} \\ &= 0.5 \left(-\frac{x - \mu_\mathrm{s}}{\sigma_\mathrm{s}^2} - \frac{\frac{1}{\sqrt{2\pi}\sigma_\mathrm{h}} e^{-\frac{x^2}{2\sigma_\mathrm{h}^2}}}{\frac{1}{2}\left(1 - \mathrm{erf}\left(\frac{x}{\sqrt{2\sigma_\mathrm{h}^2}}\right)\right)} \right) \Bigg|_{x=x_\mathrm{c}(\mu_\mathrm{s})} \end{aligned} \tag{3.10}$$

with the insertion of the spot and aperture profiles, $s_{\mathrm{ds}}(x, \mu_s)$ and $h_{\mathrm{ds}}(x)$, and their derivatives $s_{\mathrm{ds}}{}'(x, \mu_s)$ and $h_{\mathrm{ds}}{}'(x)$.

Figure 3.1 (b) provides a graphical representation of the relative gradient components and is explained step by step in the following.

The first addend of Equation 3.10, which is a straight line, is plotted as a series with varying μ_s values. The latter are indicated in mm on the corresponding line. It is intended to evaluate the gradient $p_{\mathrm{ds}}{}'(x)$ at the point $x = x_\mathrm{c}$, which is related to the spot position μ_s. Since the fraction $\frac{s_{\mathrm{ds}}{}'}{s_{\mathrm{ds}}}$ explicitly depends on μ_s, the values for x_c for each spot position μ_s are calculated first. For this, Equation 3.9 is solved for $x = x_\mathrm{c}$ via determination of the roots, $p_{\mathrm{ds}}(x) - 0.5 = 0$, for profiles with varying μ_s. In each case, the solution of the root for the profile's side pointing towards the aperture is taken. A third degree polynomial fit function relates x_c to μ_s: $x_\mathrm{c} \approx 0.0008\,\mu_\mathrm{s}^3 - 0.0073\,\mu_\mathrm{s}^2 + 0.1543\,\mu_\mathrm{s} + 0.2883$. With this result, the values of x_c for various spot positions are available analytically for the gradient analysis and are marked with the red crosses in Figure 3.1 (b).

One might expect a direct dependence of the fraction $\frac{h_{\mathrm{ds}}{}'}{h_{\mathrm{ds}}}$ on μ_s. This is not the case, since

the fraction only applies to the position x_c where the function value is determined. The plot of $\frac{h_{ds}\prime}{h_{ds}}$, which is the second addend of Equation 3.10, is displayed in light blue in Figure 3.1 (b) and shows a strong decay with x.
The resulting gradient $p_{ds}\prime(x)$ due to both addends for different values of $x = x_c$ is calculated and indicated by red circle markers in Figure 3.1 (b).
Equation 3.4 finally yields the LP from the gradient $p_{ds}\prime$ with varying spot positions μ_s, which is given as LP_{ds} in the inset of Figure 3.1 (b). From the definition of the aperture profile geometry in Equation 3.7, it follows that positive spot positions imply a spot overscanning. Overall, it can be seen that the gradient becomes larger for the absolute value with increasing x and thus a larger overscanning, and the LP consequently decreases.

3.2.2. Approach B: The approximated convolution approach

The contributing components and the resulting dose profile $p(x)$ as the convolution of the multiplication of spot $s(x)$ and aperture profile $h(x)$ with the lateral spread due to angular confusion $a(x)$ (Equation 3.2) are presented in Figure 3.2. This approach approximates the latter convolution by a convolution of two Gaussian functions. The width of the computed profile is evaluated as a measure of the LP, as explained in the following.
Starting from the multiplication of $s(x)$ and $h(x)$, the product is given by

$$m(x) = s(x) \cdot h(x) = \begin{cases} s(x) & x \leq 0 \\ 0 & x > 0 \end{cases} = \begin{cases} \frac{1}{\sqrt{2\pi}\sigma_s} e^{-\frac{(x-\mu_s)^2}{2\sigma_s^2}} & x \leq 0 \\ 0 & x > 0 \end{cases}. \tag{3.11}$$

These functions are shown in Figure 3.2. To describe the profile $p(x)$ propagated to a plane further downstream, $m(x)$ has to be convolved with the lateral spread $a(x)$, here approximated by the quadratic addition of their standard deviations σ_m and σ_a. The following calculation is based on the full width at half maximum (FWHM), for which the mathematical relation $\sigma = \frac{FWHM}{2\sqrt{2\ln 2}}$ holds. To find an expression for the FWHM of $m(x)$, $FWHM_m$, $m(x)$ is normalized to the maximum value, which is at μ_s for the case $\mu_s < 0$ and at $x = 0$ for $\mu_s \geq 0$. This relative profile of $m(x)$ is solved for the x values, returning $m(x) = 0.5$. The FWHM results from the absolute value of the existing solution, since here, $FWHM_m$ is the distance from $x = 0$ to the solution of $m(x) = 0.5$:

$$FWHM_m = \begin{cases} \left|\mu_s - \sqrt{2\ln(2)}\sigma_s\right| & \mu_s < 0 \\ \sqrt{2\ln(2)}\sigma_s & \mu_s = 0 \\ \left|\mu_s - \sqrt{\mu_s^2 + 2\ln(2)\sigma_s^2}\right| & \mu_s > 0 \end{cases}. \tag{3.12}$$

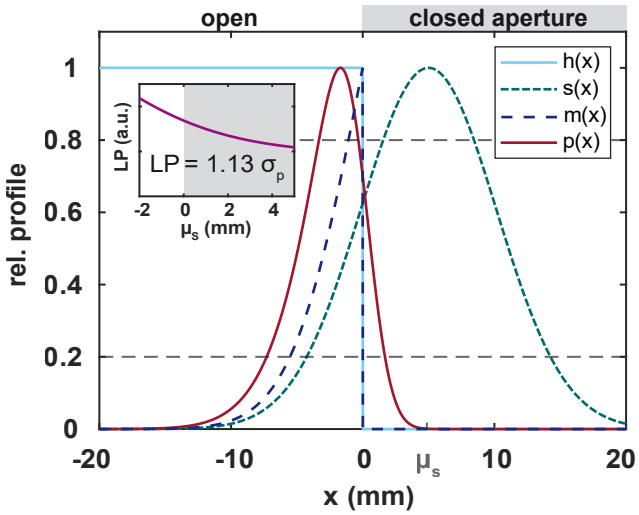

Figure 3.2.: Numerical presentation of Approach B: The aperture edge profile $h(x)$ as the Heaviside function, the spot profile $s(x)$ and their product $m(x)$ are given. A convolution of $m(x)$ with the lateral spread $a(x)$ (Equation 3.2) yields the resulting profile $p(x)$. The lateral penumbra of the latter for varying spot positions μ_s is shown in the inset, with the closed aperture marked by the gray shaded area. Figure from Behrends et al. (2023).

The solution for $\mu_s < 0$ is valid as long as $|\mu_s| \leq \sqrt{2\ln(2)}\sigma_s$. In the case of $\mu_s < 0$ and $|\mu_s| > \sqrt{2\ln(2)}\sigma_s$, two solutions not equal to zero would satisfy the condition of $m(x) = 0.5$ and the FWHM would correspond to their difference. However, the latter case is not considered in this approach.

This enables the calculation of the FWHM of $p(x)$ as

$$FWHM_p = \sqrt{FWHM_m^2 + FWHM_a^2}. \tag{3.13}$$

By calculating σ_p for $FWHM_p$, and using the relation between the standard deviation and the LP obtained in Bäumer and Farr (2011), the LP can be deduced as

$$LP \approx 1.13\sigma_p. \tag{3.14}$$

Applying this to several spot profiles for multiple spot position μ_s leads to the dependency on the LP shown in the inset of Figure 3.2. It indicates a smaller LP for a larger spot overscanning.

3.3. Methods of collimated spot position optimization

3.3.1. Verification of analytical approaches

This section outlines the experimental methods and simulations used to validate the theory developed in Section 3.2. As in the analytical approaches, the LP of a single spot profile with varying spot position relative to the aperture edge in air is investigated. The experiments are performed with film measurements and the simulations consist of computations in TOPAS and in the clinical TPS. The general setup of the measurements and simulations is sketched in Figure 3.3.

3.3.1.1. Measurements of single spot profiles in air

The fixed beam line at the WPE with an IBA universal nozzle, which can be equipped with an aperture (Section 2.3, Figure 2.4), is used for the experiments in the PBS delivery mode. A half-open 3.3 cm thick brass aperture is attached to the snout. To measure the effect of the spot position on the LP, the position of a single spot in the here-named *spot position plane* is varied from -2 mm to 5 mm relative to the aperture edge, as shown in Figure 3.3. Since the lateral spot positions in the scanning system are defined for the isocenter plane and the beam is divergent, the positions defined in the spot position plane have to be calculated for the isocenter plane. For this purpose, the known mean virtual source axis distance, which is the mean distance of the scanning magnets to the isocenter, is used (Figure 2.6). The protons have an energy of 150 MeV with a width in air at the isocenter of $\sigma_s = 5.4$ mm.

To measure high resolution profiles in air, Gafchromic EBT3 radiochromic films (Ashland LLC, Bridgewater, NJ, USA) are used, which have a negligible entrance window of 125 µm polyester and are suitable for dosimetry of PBS with apertures [Maes et al. (2019)]. These are attached to the surface of a stack of plastic blocks to ensure stable positioning of the films perpendicular to the central beam propagation direction. These plastic blocks can be seen partially in the photo of Figure 3.3. The optical density of the two-dimensional dose distribution of each collimated spot is detected at a distance of 5 cm and 13 cm in air (detection planes in Figure 3.3). The films are scanned 40 hours after exposure with the flatbed document scanner Epson Expression 10000XL (Epson, Suwa, Japan) with a resolution of 0.13 mm (200 dpi) and a color depth of 48 bit, i.e. 16 bit per color channel. Half an hour before the irradiated films are scanned, the scanner is turned on to warm up and 10 blank scans are performed. To eliminate further impacts of the scanner, a template is used, whereby the films are scanned at the same position in the

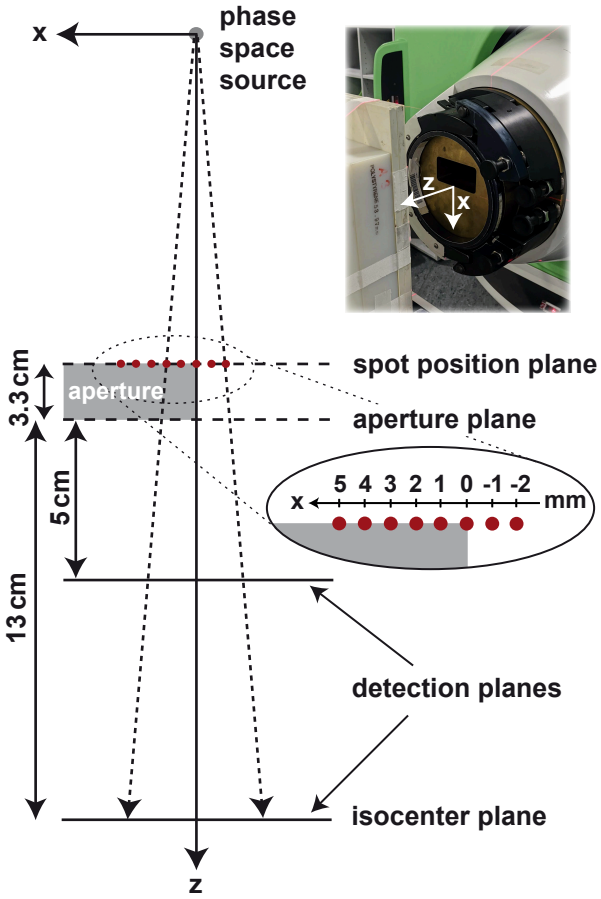

Figure 3.3.: Sketch of the setup for experiments and simulations. The phase space source and the propagation direction of the proton beam are indicated. The half-open aperture with the edge at $x = 0$ is shown as a gray shaded area. The multiple spot positions in the *spot position plane* are marked by the red dots. These range from -2 mm in-field to 5 mm overscanning, as can be seen in the magnification. The dose profile of each collimated spot is evaluated in 5 cm and 13 cm airgaps by film measurements or simulations. The photo shows the experiment with the half-open aperture mounted in the snout in the FBTR. Figure from Behrends et al. (2023).

center of the scanner and in the same orientation.
A calibration curve is used to map the optical density to the absorbed dose. This calibration is defined for the red color channel of the scanned films, which is the most sensitive color channel for low dose levels [Sorriaux et al. (2013)]. For further analysis, the relative dose profiles are processed in the myQA software (IBA Dosimetry, Schwarzenbruck, Germany, version 2.12). To compensate for uncertainties in the positioning of the films in each measurement, they are shifted relative to each other, so that the 50% dose levels align at the edge, with the measurement at $\mu_s = -2\,\text{mm}$ serving as the reference.
For the one-dimensional dose profiles perpendicular to the aperture edge, the row including the pixel value of maximum intensity is selected. To compensate for small inaccuracies, two rows before and two rows after the selected one are also included. The dose profile values for each lateral step are averaged over the five values and the standard error is given.

3.3.1.2. Monte Carlo simulations of single spot profiles in air

TOPAS Simulations of relative dose profiles of the collimated spots are computed in TOPAS (version 3.5). In the measurements and as illustrated in Figure 3.3, the profile of a single spot is recorded for multiple spot positions starting with $\mu_s = -2\,\text{mm}$ (in-field) up to $\mu_s = 5\,\text{mm}$ (overscanning) recorded downstream of the aperture edge. The simulations are based on a beam model in which the source is described by a phase space placed at the snout exit 53 cm upstream from the isocenter. From the phase space source, the protons emanate from a bivariate normal distribution, for which the Fermi-Eyges parameters, the mean energy corresponding to 150 MeV (σ_s at source plane is 5.2 mm) and the energy spread, are defined [Verbeek et al. (2020); Bortfeld (1997); Clasie et al. (2012); Grassberger et al. (2014)]. Unlike the measurements, the spot positions are specified here in the phase space source, which means that the defined positions in the spot position plane must be projected back onto the source plane of the simulations. Thereby, the deflection of the protons at the scanning magnets are considered in the beam model. The spot parameters are computed by the method of Kimstrand et al. (2007).
According to the setup in Figure 3.3, a half-open 3.3 cm thick brass block is positioned in the aperture plane with the edge centered to $x = 0$ in the simulation environment. Corresponding to the composition of the brass aperture used, the mean excitation energy of 333.2 eV is specified for brass. A one-dimensional air-filled detector volume scoring the mean dose with a voxel length of 5 mm parallel to the aperture edge, a voxel width perpendicular to the aperture edge of 0.05 mm and a voxel length of 0.05 mm in the beam propagation direction (in z-direction) is created. Thus, each dose profile is captured at 5 cm and 13 cm downstream of the aperture in air with a lateral resolution of 0.05 mm.

For computing the electronic stopping power in air, TOPAS refers to the International Commission on Radiation Units and Measurements (2014) Report 90. For the transport calculations, the production cut for all particles is set to 5 µm according to Wulff et al. (2018) and the default value for the maximum step size of 1 mm remained unchanged.
For each spot, 10^9 initial protons are simulated, resulting in a maximum mean statistical uncertainty of 1% of all values of the relative dose profile above 10%.
As recommended in Jarlskog and Paganetti (2008), the physics packages *g4em-standard opt4, g4hphy QGSP BIC HP, g4decay, g4ion-binarycascade, g4h-elastic HP* and *g4stopping* are included in the Monte Carlo computation. No variance reduction strategies are employed.

The RayStation treatment planning system The commercial TPS RayStation (version 12A Evaluation) is additionally used to verify the single spot profiles. As for the experiment and the TOPAS simulation, the setup shown in Figure 3.3 is used. A half-open 3.3 cm thick aperture made of brass, as described in Bäumer et al. (2021), with the edge centered is placed in the snout of the PBS universal nozzle. The varying spot position must be implemented in RayStation - as for the fields in the measurements - for the isocenter plane, which is why the conversion of the spot propagation from the spot position plane to the isocenter plane is applied. The proton energy is set to 150 MeV with a $\sigma_s = 5.4$ mm at the isocenter in air. A $1 \times 1 \times 1\,\text{mm}^3$ dose grid is used for dose computation in air evaluated at 5 cm and 13 cm distance downstream of the aperture. To set the dose grid symmetrically around the center, care is taken to ensure an aperture edge position centered within a voxel.
The implemented Monte Carlo dose engine, which calculates the dose up to a mean relative uncertainty of 0.5%, adjusts the internal lateral computational grid in the aperture block in accordance with the aperture opening size. For this reason, a smaller aperture opening than in the experiment is chosen, while the position of the edge is maintained. With a reduced aperture opening of $8\,\text{cm}^2$ in contrast to the half opened shape before, a lateral block resolution of 0.2 mm is achieved. However, no perturbing effects are expected from this smaller opening.

3.3.2. Investigation of clinically relevant setups *in silico*

Previously, the simplest setup of a spot in air is studied based on theoretical approaches. To investigate influences on the clinical outcome due to the potential impact of the spot position on the LP, simulations in RayStation of more clinically relevant setups are performed. First, a single spot is again evaluated but at this time in a water environment for different energies and in combination with a range shifter. In addition, field profiles

of mono-energetic two-dimensional spot patterns with different spot configurations are studied.

3.3.2.1. Single spot profiles in water

Comparable investigations in RayStation as in Section 3.3.1.2 (same setup as in Figure 3.3) are performed for single spots in water. A second proton energy of 100 MeV (in air σ_s at isocenter 8.1 mm) in addition to the 150 MeV ($\sigma_s = 5.4$ mm) is implemented. In addition, the influence of two clinical range shifters is examined: For 150 MeV the clinical range shifter of the WPE, so-called *RS74,* with a water-equivalent thickness of 74 mm is used, and for 100 MeV the *RS51*, with corresponding 51 mm WET, is used due to the different proton ranges.
Unlike before, here, the isocenter is placed in the Bragg peak plane, which is located in the target volume in a clinical situation. A clinically realistic airgap of 5 cm between snout and the water phantom is adjusted, except for the case of 100 MeV spots without range shifter. In this scenario, a minimal airgap of 6.1 cm is possible due to the maximum extended snout position under clinical conditions. Profiles with the spot positions from -2 mm to 5 mm in the spot position plane are examined at different water depths. For both energies, the depths at 3 cm, 5 cm and one in the Bragg peak vicinity, more specifically, proximal 1 cm to the peak, are evaluated. The latter approximates the modulation center of the SOBP for clinical extended fields with multiple energy layers (Section 2.1.4.1, Figure 2.1). For 150 MeV, an additional depth of 10 cm is chosen.
Further parameters remained unchanged compared to the previous studies of spots in air in RayStation.

3.3.2.2. Two-dimensional spot pattern

Various two-dimensional spot patterns are configured for a $4 \times 4\,\mathrm{cm}^2$ aperture, with half of each one-dimensional spot array sketched in Figure 3.4. The spots in RayStation are calculated for an energy of 150 MeV ($\sigma_s = 5.4$ mm) and are placed with a constant spot spacing of $\lambda = 4$ mm in respect to each other. The distance of the spots with the outermost position varies relative to the aperture edge, depending on the pattern arrangements: In the *in-field* configuration, all spots are placed within the opening of the aperture, with the outermost spots starting with a distance of $\frac{\lambda}{2} = 2$ mm to the aperture edge. In *edge*, the outermost spots are positioned directly on the aperture edge (top right). The *OS* (overscanning) configuration implies a possible configuration of overscanning with the outermost spots positioned with an overscanning of $\frac{\lambda}{2} = 2$ mm. The *OS enhancement* configuration implements the concept of fluence modulation of Winterhalter et al. (2018), where the overscanned spots have an extra weight of 50%.

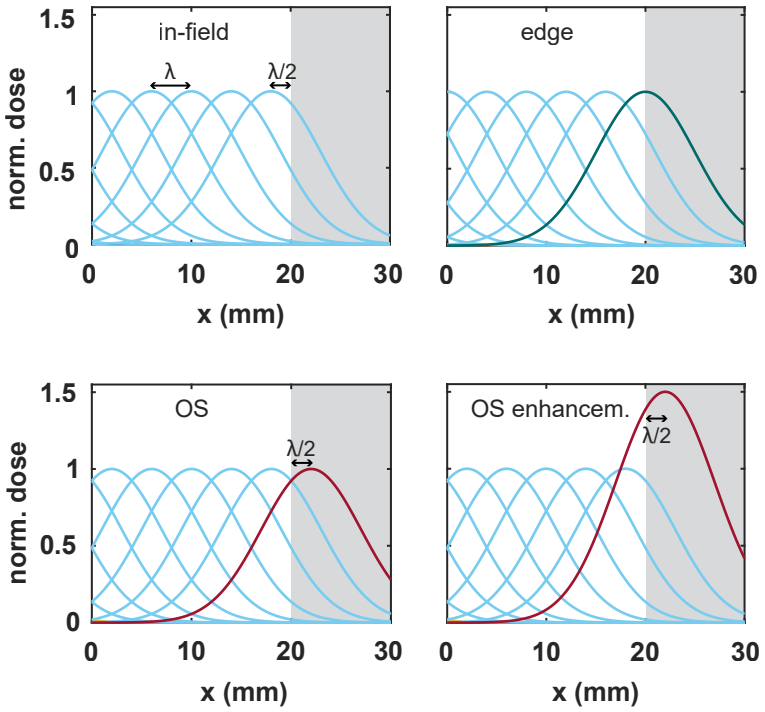

Figure 3.4.: Schematic sketch of the two-dimensional spot patterns studied in RayStation. For each configuration, half of a one-dimensional spot row of the two-dimensional pattern is sketched with Gaussian-shaped spots and a σ_s of 5 mm. The spot placement is adjusted relative to the aperture edge (at $\mu_s = 20\,\text{mm}$), while the spots are symmetrically arranged with a spot center spacing of $\lambda = 4\,\text{mm}$ for all configurations. In the sketch top left the *in-field* configuration is shown, where all spots are placed inside the aperture opening for a distance $\frac{\lambda}{2} = 2\,\text{mm}$ from the edge. In *edge*, the outermost spots, here one drawn in dark green, are positioned on the aperture edge (top right). In the *OS* configuration (bottom left) the outermost spots, of which one is shown in dark red, are $\frac{\lambda}{2} = 2\,\text{mm}$ overscanned and in *OS enhancement* configuration, they are weighted by additional 50% (bottom right). Figure based on Behrends et al. (2023).

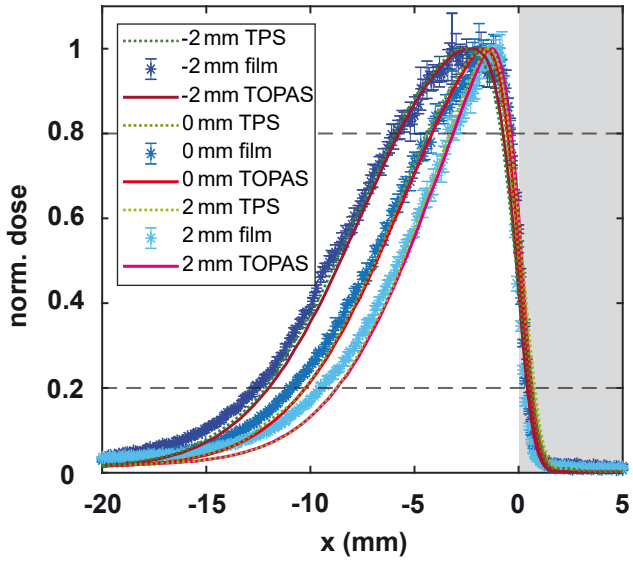

Figure 3.5.: Relative dose profiles of collimated spots at 150 MeV in 13 cm air for spot positions at $\mu_s = -2$ mm, 0 mm and 2 mm. The gray shaded area symbolizes the aperture. Shown are the experimental data in blue colors, denoted by 'film', the Monte Carlo simulations with TOPAS in red colors and the RayStation treatment planning system ('TPS') in green dotted lines. For the film measurements, the standard error of each sampling point is indicated by an error bar. The errors of the Monte Carlo simulations are not shown because of their smallness. Figure from Behrends et al. (2023).

As in previous computations in RayStation, the dose is calculated on a $1 \times 1 \times 1\,\text{mm}^3$ grid in water and the dose profiles are extracted at water depths of 3 cm, 5 cm and 10 cm. Since the internal resolution of the block for aperture openings below $10\,\text{cm}^2$ is 0.2 mm (as for the previous RayStation calculations) and otherwise scales with the aperture opening, an internal lateral computation grid of about 0.3 mm is assumed for the aperture opening that is here $16\,\text{cm}^2$. Further parameters and settings in RayStation, as well as the airgap of 5 cm, remain as in the previous calculations.

3.4. Results of collimated spot analysis

3.4.1. Single spot profiles in air

Figure 3.5 presents the relative dose profiles of spots at the aperture edge for the selected positions $\mu_s = -2$ mm, so 2 mm in-field, directly on the aperture edge ($\mu_s = 0$ mm), and with 2 mm overscanning, $\mu_s = 2$ mm. A comparison of the film measurements, as well as the simulations with TOPAS and RayStation, is given. The profiles of the 150 MeV spots are shown here exemplarily for the 13 cm airgap. The initial Gaussian-shaped spot profile is asymmetric due to collimation and clearly truncated on the side towards the

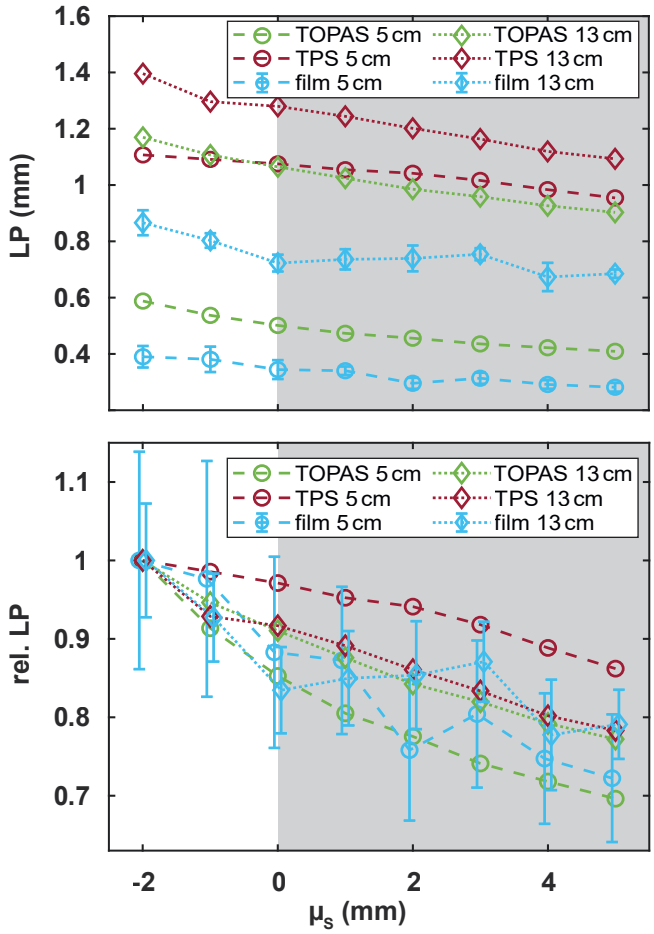

Figure 3.6.: Absolute (top) and relative (bottom) values of LP from collimated 150 MeV spots measured and simulated with varying spot position μ_s and 5 cm (dashed lines) and 13 cm (dotted lines) distance in air. The relative LP values are normalized to the value of LP at $\mu_s = -2$ mm. The aperture is indicated by the gray shaded area, and the labels 'film' and 'TPS' refer to the film measurements and simulations in the RayStation treatment planning system, respectively. The lines connect the data points only to guide the eye. Figure from Behrends et al. (2023).

closed aperture (gray shaded area), generating a sharp dose fall-off. The position of the normalized maximum is closer to the aperture edge when the spot is placed on the edge ($\mu_s = 0$ mm) compared to $\mu_s = -2$ mm, and even closer for 2 mm overscanning. This leads to a steeper dose fall-off from $\mu_s = -2$ mm to $\mu_s = 0$ mm to $\mu_s = 2$ mm.

Figure 3.6 provides an overview of the absolute and relative LP values from all investigated spot positions in 5 cm and 13 cm air for the film measurements and simulations in TOPAS and RayStation. Comparing the different airgaps for each evaluation method, the absolute LP (upper graph) is larger after the protons have penetrated 13 cm of air than after 5 cm of air. In addition, the film measurements reveal the smallest absolute values and RayStation the largest. While the film measurements show small variations in the

trend, the absolute LP generally decreases with larger spot position, which means from $\mu_s = -2\,\text{mm}$ to $\mu_s = 5\,\text{mm}$.
Basically, the relative values of the LP in the bottom graph of Figure 3.6, normalized to the value at $\mu_s = -2\,\text{mm}$, confirm the observed tendency of a decreasing LP from $\mu_s = -2\,\text{mm}$ to $\mu_s = 5\,\text{mm}$. Fluctuations in this trend for the film measurements, however, are more apparent due to normalization. While the relative values at 5 cm in RayStation exhibit a smaller effect than those at 13 cm, the relative ones in TOPAS at 5 cm airgap give the largest relative decrease in the LP for a larger spot position. A very good agreement is found between the RayStation and TOPAS results at the 13 cm airgap. Altogether, the methods result in an average 20% decrease in the LP in air with 5 mm overscanning compared to a spot position of 2 mm in-field.

3.4.2. Single spot profiles in water

Figure 3.7 shows the results of the absolute and relative LP for the simulations in RayStation at different water depths for a 150 MeV and a 100 MeV proton spot with varying position μ_s and for some cases in combination with a range shifter. The absolute LP at shallow water depths of 3 cm and 5 cm is larger for 100 MeV than for 150 MeV, as shown in Figure 3.7 (a). At greater water depths, 1 cm before the Bragg peak and in combination with a range shifter, the LP shows a smaller magnitude for the 100 MeV protons. The LP increases with increasing penetration depth for each energy, as also shown by the absolute LP values with increasing air distance in Figure 3.6. Likewise, a decreasing trend of the LP magnitude for overscanning can also be observed.
The relative values of LP, normalized to the value at $\mu_s = -2\,\text{mm}$, are provided in Figure 3.7 (b). In general, a stronger effect on the LP is evident at 150 MeV: The LP relative to that at the spot position for -2 mm in-field becomes smaller with increasing overscanning. The same order of magnitude as in the studies in air (Figure 3.6), meaning a 20% decrease in the LP with up to 5 mm spot overscanning, can be observed at small water depths of 3 cm and 5 cm. This effect decreases to about 15% at a water depth of 10 cm. At larger water depths close to the peak area or when applying a range shifter, the effect further decreases, but there still remains a 7% to 10% reduction in LP at up to 5 mm overscanning.
In contrast, at 100 MeV there is almost no difference between various water depths or in combination with a range shifter. Nevertheless, also a spot overscanning up to 5 mm results in a 10% decrease of the LP compared to the spot placed -2 mm in-field.

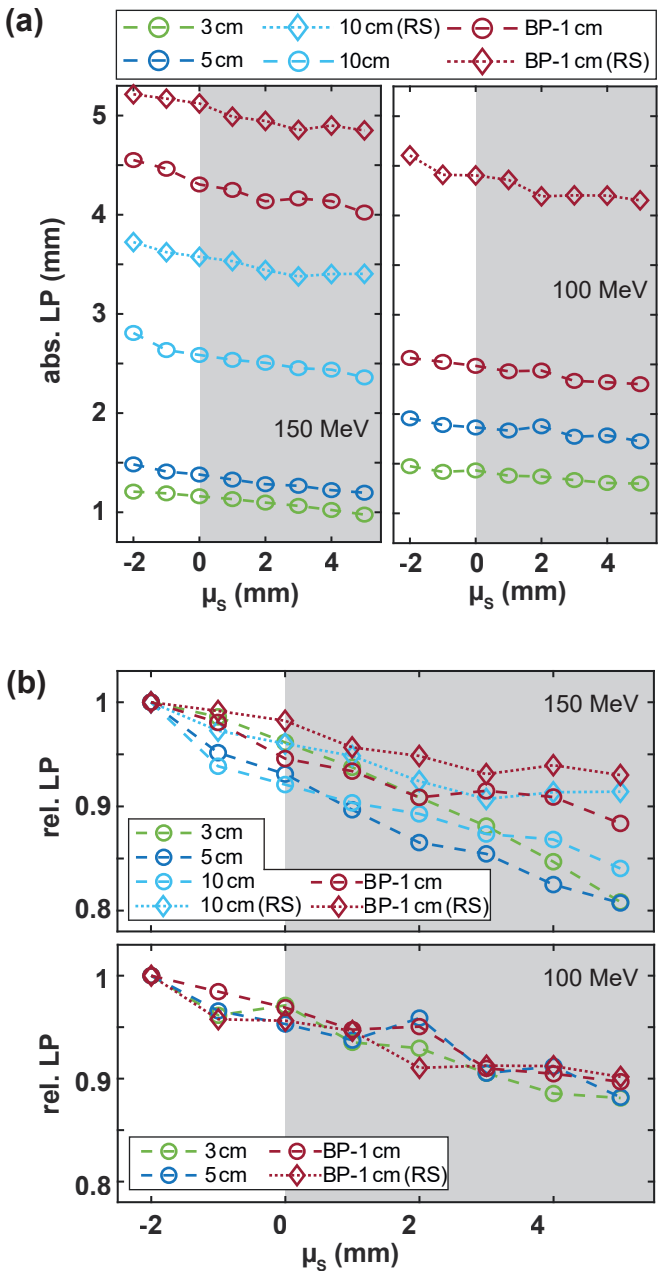

Figure 3.7.: Results of the absolute (in **(a)**) and relative (in **(b)**) lateral penumbra (LP) of the collimated spot profiles in water simulated in RayStation for several spot position μ_s and energies of 150 MeV (left in (a) and top in (b)) and 100 MeV (right in (a) and bottom in (b)). For each configuration, the values are normalized to the value at $\mu_s = -2$ mm. With an airgap of 5 cm (6.1 cm at 100 MeV and without range shifter) water depths of 3 cm, 5 cm and 10 cm, as well as 1 cm proximal to the Bragg peak are shown. The gray shaded area implies the closed aperture and 'RS' indicates that a range shifter is included in the study. The latter has a water-equivalent thickness of 74 mm for 150 MeV and 51 mm for 100 MeV. Figure from Behrends et al. (2023).

Table 3.1.: Values for aperture margin with iso-coverage of 95% of the various field configurations.

field configuration	aperture margin (mm)		
	3 cm WED	5 cm WED	10 cm WED
in-field	7.1	6.1	7.7
edge	4.8	5.2	6.3
OS	3.1	3.5	4.6
OS enhancem.	1.1	1.4	3.1

3.4.3. Profiles of two-dimensional spot patterns in water

The one-dimensional central relative dose profiles of the two-dimensional spot patterns of Figure 3.4 are presented in Figure 3.8 (a), showing half of the profile from the center of the field to the edge. The profiles consisting of 150 MeV spots at 3 cm water depth are presented on the left, at 5 cm water depth in the middle and at 10 cm water depth on the right. Comparing these water depths, it can be seen that the dose profiles are sharper (larger slope at the edge) at smaller water depths.

Figure 3.8 (b) provides the LP values of the profiles shown in (a). From the previous analyses it is known, that the LP increases with water depth for the same field configuration. When comparing the different spot pattern configurations, differences in the LP are further evident: For example, in 3 cm water depth, there is a 30% reduction in the LP of the *OS* configuration relative to the *edge* configuration, and almost 15% reduction of *OS enhancement* relative to *OS*. For 5 cm water depth, the LP of the *OS* arrangement relative to the *edge* configuration becomes smaller by 26% and of the *OS enhancement* arrangement relative to the *OS* configuration by 17%. The effect diminishes for the larger water depths of 10 cm: The values show an LP decrease of 10% of the *OS* arrangement relative to the *edge* configuration and a decrease of nearly 13% from *OS enhancement* relative to *OS*.

However, the spot arrangements yield differences in the shape of the field profiles, especially in the high dose region, which is indicated in Figure 3.8 by the 95% isodose. This leads to different field widths and uniformities within the 95% dose level. To compare the field widths with identical tumor coverage, the differences between the 50% isodose and 95% isodose corresponding to the aperture margin in treatment planning are given in Table 3.1. The values indicate that the aperture margin decreases from the *in-field* configuration through the *edge* configuration, the *OS* configuration up to the *OS enhancement* arrangement. Moreover, it increases with increasing water depth, except for *in-field* and 5 cm depth. In general, this trend reveals the proportionality of aperture margin and LP.

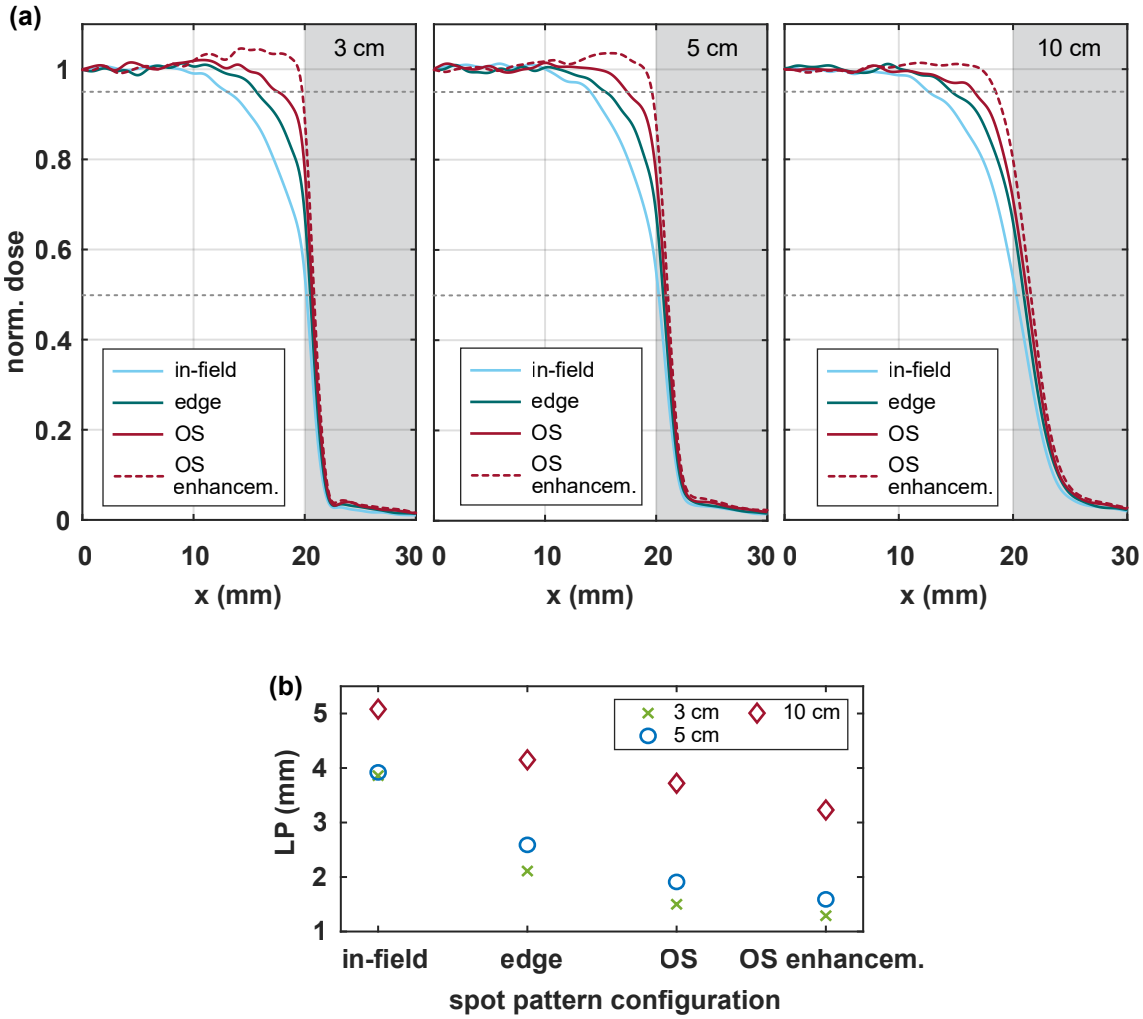

Figure 3.8.: Central one-dimensional dose profiles at 3 cm (left), 5 cm (middle) and 10 cm water depth (right) from the two-dimensional spot pattern configurations with 150 MeV spots simulated in RayStation, as outlined in Figure 3.4, are shown in **(a)**. The dose profiles are illustrated for the half-field from the center to the edge, with the gray shaded area indicating the closed aperture. For orientation, the 95% and 50% isodoses are marked by the gray dashed lines. **(b)** gives an overview of the LP values of the different spot pattern configurations for the three water depths. Parts from Behrends et al. (2023).

3.5. Discussion and conclusion of the collimated spot position optimization

The impact of spot positioning in PBS with apertures relative to the aperture edge on the LP is studied in detail for this project. It is demonstrated that spot overscanning, meaning the placement of the outermost spot on the closed side of the aperture, provides a benefit for the LP. A sharper LP potentially increases the sparing of normal tissue and organs at risk lateral to the fields in PBS with apertures. To conclude these findings, analytical proofs of a reduced LP with overscanning spot position are provided and verified with measurements and simulations in air. In addition, *in silico* studies in water in the TPS serve to evaluate the clinical impact based on different parameters, such as the combination with range shifters, and different energies or water depths.

Theoretical approaches of the spot penumbra optimization

By means of the two analytical approaches based on different assumptions, it could be argued that the LP is influenced by the spot position and decreases with spot overscanning. The first Approach A (Section 3.2.1) is based on the optimization problem in which the gradient of the resulting spot profile should be maximized, as a measure for the LP. Using Equation 3.10, this may suggest that for maximizing $p_{ds}{}'$ over μ_s, both addends should point the trend in the same direction and the outermost spot edge is in line with the aperture edge. However, as shown in Figure 3.1, the relative gradient of the aperture is considerably larger in absolute magnitude than the relative gradient caused by the spot. On the contrary, it is advantageous to place the outermost spots of a field in such a way that the large contribution of the relative gradient of the aperture is exploited. In other words, the position x_c should be favorably modified for this purpose, which can be achieved by overscanning. As this may be rather counterintuitive, Approach B (Section 3.2.2) presents the analytical results from another point of view.
Both approaches adopted approximations, such as the choice of σ_h for the description of the aperture profile downstream, or to simplify the mathematical operation of convolution. These simplifying assumptions in both approaches lead to the presentation of LP in arbitrary units. Therefore, only a similar trend can be recognized, while the results from the measurements and simulations (Figure 3.6) cannot be compared directly.

Validation of a collimating spot position theory

In general, the studies in Section 3.4.1 corroborate the theoretical approaches. The fact that the normalized profile in Figure 3.5 is sharpest at $\mu_s = 2\,\text{mm}$ confirms the trend of

a smaller LP with spot overscanning. The larger absolute LP values for a larger airgap (Figure 3.6) are consistent with observations in other studies [Bäumer et al. (2019); Maes et al. (2019); Ciocca et al. (2019)] and can be explained by an increased angular variance of the initial spot with increasing airgap. With the longer trajectory of protons through material, also the MCS increases (Section 2.1.2). Both Monte Carlo simulation methods reveal the same trend of decreasing an LP with overscanning. However, the absolute values in RayStation are larger, which is due to the larger computation grid of 1 mm, causing a volume averaging effect. Due to the smaller resolution of 0.05 mm, the TOPAS simulations resulted in smaller values for the LP. However, although the film measurements have a larger resolution of 0.13 mm, the measured LP is still smaller than those of TOPAS. This may be caused by inaccuracies in the TOPAS simulation, e.g. due to the implemented beam model. Various influences on the film dosimetry, such as uncertainties in the calibration curve or LET effects, can also be responsible. In addition, inconsistencies in the spot positioning of the system during the experiment can play a role. The latter are validated during the monthly quality assurance and the position accuracy is expected to be less than 1 mm depending on the deflection distance. Nevertheless, these differences in the absolute LP occur on extremely small scales. While the relative results of the film measurements show variations in the trend, they also exhibit large error bars because of the error propagation. Considering the standard errors, a decreasing LP with spot overscanning is evident and the film measurements verify experimentally the trend of the Monte Carlo simulations and analytical proofs.
An alternative dosimetry method to measure steep dose gradients would be a pixel detector [Schilling et al. (2022b)] or based on radioluminescence [Metzner et al. (2022)].

Investigations on the collimated spot positioning in water

Investigations of individual spot profiles in water show an LP increase with depth (Figure 3.7). There are two influences contributing to the smearing of the profile, i.e. the increase of the LP, with water depth: On the one hand, there is the contribution of the increasing angular confusion of the spot's initial angular variance with depth, as in air. On the other hand, the increasing MCS with water depth contributes to the increase in LP. The results show that for the same water depths, 3 cm and 5 cm, the LP is smaller for a higher energy due to its smaller initial σ_s and smaller initial angular variance. The results in water are consistent with those of other studies [Bäumer et al. (2019); Maes et al. (2019); Ciocca et al. (2019)]. The spot profiles in water with varying position for 150 MeV at depths of 3 cm and 5 cm demonstrate a decrease in the relative LP of about 20% with 5 mm spot overscanning (Figure 3.7), similar to investigations of a spot in air (Figure 3.6). Further setups at larger depths, for 100 MeV or in combination with a range

shifter produce also an effect on the LP with overscanning, mostly in the range of 7% to 10%. But overall, the results suggest a clinical relevance of this spot overscanning method.
The smaller effect on the LP decrease for spot overscanning at larger depths can be attributed to the increasing lateral scattering due to MCS with depth, as in air (Section 2.1.2). MCS in PMMA is also responsible for a smaller effect on LP reduction in the modality of collimated PBS with a range shifter for superficial tumors, which has been considered in many publications so far [Bäumer et al. (2018, 2019, 2021); Bues et al. (2005); Dowdell et al. (2012); Winterhalter et al. (2018); Maes et al. (2019)]. The decrease in the overscanning effect on the LP for a lower energy reflects that this effect depends on the initial spot width σ_s, like the LP itself. The relative benefit on the LP from overscanning is therefore smaller with larger σ_s. Beyond these simple setups, these results encourage further analyses of a spot position dependence on the LP in clinical scenarios. Of potential interest would be treatment plans with multiple fields, fields with multiple energies, configurations of different range shifter thicknesses or materials, and modifying the order of aperture and range shifter in the snout, as analyzed in Bäumer et al. (2018, 2019).

The results discussed so far consider only a single spot. Based on this, small fields consisting of only a few overscanned spots are conceivable for stereotactical fields or radiobiological applications, where the previously observed effect on the LP with single spots is expected. For a more clinically representative setup, the effect is studied in two-dimensional spot patterns (Figure 3.4), with the extension to fields consisting of many spots proving to be straightforward (Figure 3.8). Using the simple field configurations, the trend of the single spot analyzed before can be confirmed by the fact that the arrangement with the outermost spots at 2 mm overscanning results in a smaller LP than with a positioning in-field or on the edge. Likewise, the LP increases with a longer proton pathway due to MCS for the same field configuration. In addition, further benefits are motivated by the fluence modulation. Even for non-collimated fields with contour-driven spot positioning, a sharper LP is found when higher weights are applied to the outermost spots [Meier et al. (2017)]. In Winterhalter et al. (2018) the technique 'collimated edge enhancement' based on fluence modulation by spot weight optimization at the aperture edge in collimated PBS yielded also advantages with respect to the LP. The results in Figure 3.8 highlight the potential of combining overscanning and fluence modulation for spot optimization in the collimated PBS techniques. A consideration of other parameters, such as variable spot weighting or spot spacing for field optimization, should be addressed in follow-up research. Further, the overscanning method is associated with a

high fluence loss demanding a higher accelerator output, which is an important aspect to be considered.

Due to the fact that the two-dimensional spot patterns in Figure 3.4 are created manually and thus represent academic cases, the results of their profiles in Figure 3.8 should be interpreted carefully. The configurations are established to apply the results of a single spot to a multi-spot field arrangement and therefore probably do not constitute a realistic optimization problem in the treatment planning. A typical constraint for the plan optimization would be to cover the tumor with the 95% isodose, which, when applying a uniform dose in one field, meaning the SFUD concept (Section 2.3.3.2), is expected to yield different and rather irregular spot arrangements per energy layer. These studies nevertheless suggest that in any field layout, an improvement in lateral dose fall-off can be achieved by spot overscanning. Additionally, the studies of these theoretical field configurations emphasize the use of overscanning for the treatment planning due to the required smaller aperture margin. The fact that the aperture margin in Table 3.1 in 5 cm depth is smaller than in 3 cm depth for the *in-field* configuration, may be an effect of the RayStation computation grid. In addition, a more sensitive effect of proton edge-scattering at the aperture for the 95% isodose compared to the 50% isodose at shallower depths would be conceivable (see the dose horns below). At greater depths, this effect is expected to be compensated. Furthermore, the results in Table 3.1 show, that for all investigated water depths, the aperture margin could be reduced by 1.7 mm if the spot is overscanned by 2 mm than if it is positioned on the aperture edge for a 95% tumor coverage, for example. This would lead to an increased sparing of normal tissue.

Further outlook on the spot optimization in PBS

While in clinical practice many different energy layers forming the spread-out Bragg peak are applied to conformally cover the tumor in depth, this study examined one energy layer at a static aperture with regard to the spot position optimization. Therefore, the question remains to what extent an advantage in the LP can be expected from spot overscanning in fields with many proton energies. Based on this study and the fact that the opening of a static aperture is optimized to conform to the projected tumor extension, no different effect is expected for spot overscanning with multi-layer fields. After all, the static aperture directly affects only a few layers or one energy layer.

The combination of PBS with a dynamic collimation systems is thought to be a promising tool for improving the LP through spot optimization, based on previous investigations of Hyer et al. (2014) and Moignier et al. (2016). Based on the superposition principle, dynamic collimation forms a collimator setup for each energy layer. This enables the possibilities of a continuous spot position and fluence optimization for each collimator

setting and energy layer for the entire field formation. Such dynamic collimation systems can be found in compact proton therapy systems with adaptive apertures, which are dynamic multileaf collimators for PBS [Vilches-Freixas et al. (2020); Grewal et al. (2021)]. Smith et al. (2016) have shown that a dynamic aperture generally has advantages over a static aperture. However, if the application of the overscanning method achieves an improvement in the LP for both methods, the relative output between them is expected to remain unchanged. Furthermore, an aperture with a focusing opening would be conceivable, which would follow the shape of the beam divergence. Oblique incident protons at the aperture edge have to pass the same material thickness, which would likely reduce the secondary effects at the aperture (see below) and lead to a sharper profile. This is a theoretically interesting aspect, however, this hardware modification is difficult to realize in clinical practice.
Comparing proton spot scanning techniques with conventional photon techniques, Wang et al. (2014) found an initial proton spot size limit beneath which the proton techniques provide some advantages in stereotactical applications. The application of apertures in the PBS for field shaping makes these initial spot size constraints obsolete. Beyond that, this project demonstrates that spot overscanning at the aperture edge can achieve an LP in air of less than 1 mm with an initial in-air spot width of 5.4 mm at the isocenter. In addition, the results of this project extend the studies of Wang et al. (2015) on the determination of the aperture margin in spot scanning proton therapy, since no overscanned spot positions were considered in their study. Regarding the optimization process for the irradiation planning, based on this work, it is recommended to insert an aperture before spot optimization.

Moreover, secondary effects occurring in the interaction of the aperture material with the protons should be taken into account with regard to the out-of-field dose. These include, for example, the so-called dose *horns* formed by edge-scattered protons at the aperture, affecting the dose especially in shallow regions as observed in Titt et al. (2007) and van Luijk et al. (2001). At small depths, low-dose contamination of the generated secondary charged particles can also be problematic. Additionally, overscanning can lead to an increased neutron generation during the proton interaction with brass, since the increased target area of brass causes a higher neutron production rate.
An increased LET of protons scattered at the aperture edge due to their higher energy deposition is further expected. In the studies of Ueno et al. (2019), the observed enhancement in the dose-averaged LET is negligible compared to the entire LET distribution. Nevertheless, effects on the LET should be considered, in general when using overscanning and especially when applying the method to small fields. Overall, these secondary

effects influence the absorbed dose downstream of the aperture and should therefore be investigated in more detail in the future.

Conclusions

This project presents a method for improving the lateral penumbra by a spot positioning optimization relative to the aperture edge in collimated pencil beam scanning fields. Two mathematical independent analytical approaches extensively examine the LP as a function of the spot position. The theoretical considerations reveal that the further the spot is positioned beyond the aperture edge at the closed side, so-called spot overscanning, the smaller the LP and thus the sharper the dose profile. Film measurements at the clinical proton therapy facility WPE as well as Monte Carlo simulations in the TOPAS simulation tool and in the commercial TPS RayStation serve to validate the analytical proofs. Measurements as well as simulations confirm the result of the analytical approaches by finding up to 20% decrease of the relative LP in air with 5 mm overscanning. Moreover, *in silico* investigations demonstrate an effect of 20% LP reduction for 150 MeV at 3 cm or 5 cm WED with 5 mm overscanning. This shows, that overscanning affects the lateral penumbra of collimated spots in water especially at higher energy, lower depths, and also in two-dimensional field configurations. Combining such a spot position optimization with the fluence modulation is identified as a promising tool for field shaping in PBS with apertures.

Further research in collimated scanned proton beam therapy should elucidate secondary effects such as the influence on the out-of-field dose as well as the LET in spot positioning at the aperture edge.

Overall, these findings provide new possibilities for improving the lateral penumbra in scanned collimated proton fields to spare nearby organs at risk, especially in the entrance plateau. Particular potential is expected in combining this method with other techniques such as dynamic collimator systems. In addition, the application with respect to small fields, for example for small animal irradiations, offers particular benefit due to the relatively higher effect of LP reduction.

4. Project *micro*: Providing low-energetic proton beams for radiobiological experiments

When providing very low-energetic proton fields at clinical facilities for radiobiological experiments, the observed residual proton ranges are on the *micro*meter scale. They are of special interest for cell experiments due to their high LET, but also for comparison with alpha particles [Goodhead et al. (1992); Schneider et al. (2019)], carbon ions [Weber and Kraft (2009)] or laser accelerated protons (LAPs) [Beyreuther et al. (2017); Hanton et al. (2019); Raschke et al. (2016)].

First of all, a general overview of protons with energies down to the few-MeV level and therefore correspondingly high LET is given. It is common to reduce the protons' energy by means of absorbing materials (*absorbers*) in the beam path. However, at the first glance, this method seems to be a trivial approach: the more material, the lower the proton energy. In fact, it entails a special challenge due to physical aspects of increasing range straggling (Section 2.1.4.2) and decreasing fluence as a function of WED. The energy range of 2.5 MeV to 3.3 MeV for LAPs, implies residual ranges of about 110 µm to 180 µm in water [Berger et al. (2010a)]. Components for a suitable setup to provide such low-energetic protons as well as a possible technique for dosimetric characterization under these extreme conditions at a clinical beam line are developed and optimized. Monte Carlo simulations are conducted to analyze the energy spectra downstream of various absorber thicknesses. An optimized setup is presented for the implementation of these fairly low proton energies at a clinical facility. In other words, for each target energy there is an absorber thickness at which the maximum possible fluence can be achieved. Depth dose measurements are compared to depth dose simulations and the LET distribution is calculated.

The entire chapter is based on an own publication, which reference is given here once to

avoid frequent citations in the following:

Behrends et al. (2021), *Technical note: Providing proton fields down to the few-MeV level at clinical pencil beam scanning facilities for radiobiological experiments, Med Phys,* ***49****:666-674, 2021.*

4.1. Application of low-energetic proton fields

Radiobiological studies for a high-LET proton radiation are of particular interest. The LET increases sharply in the Bragg peak, so that the assumption of a constant RBE of 1.1 is an oversimplification (Section 2.2.2). With the help of cell experiments for this LET range, the radiation effect due to a higher RBE could be investigated with regard to normal tissue complications. In addition, more *in vitro* data can be provided to develop or validate RBE models, for example based on different ion types [Tian et al. (2022)]. This leads to the opportunity to improve concepts of treatment planning with respect to distally located organs at risk. The radiobiological effect of high-LET protons is also discussed in other studies [Chaudhary et al. (2014); Guan et al. (2015); Dahle et al. (2017)].
Since most clinical facilities can provide proton energies between $60-230\,\mathrm{MeV}$, the most challenging aspect of this kind of experiments is to generate the low proton energies. Regarding previous projects for low-energetic protons, the proton beam in the work of Dahle et al. (2017) is generated at a research institute and therefore not within clinical parameters, and an eye treatment beam line was used in Chaudhary et al. (2014). Therefore, the generation of a suitable low-energetic proton beam in the high-LET range at a clinical PBS facility is still outstanding. The biological effectiveness was already addressed by the work of Guan et al. (2015) and Patel et al. (2017) in which absorbing materials of different thicknesses was placed in the beam path to degrade the energy of the protons for different LET values. An *in silico* implementation using a small animal irradiation platform at a clinical proton therapy facility with energies between 20 and 50 MeV is presented in Gerlach et al. (2020).

Example: Comparison with laser accelerated protons Laser-plasma acceleration is an alternative proton acceleration technique in addition to the acceleration with a cyclotron (Section 2.3.1) or a synchrotron. The acceleration process is based on the method of *target normal sheath acceleration* [Roth and Schollmeier (2016); Wilks et al. (2001)]. A major advantage for clinical application would be the much simpler laser beam guidance by lenses and mirrors, not requiring elaborate shielding [Schippers (2015)]. In addition, LAPs induce ultra-high dose pulses (in the order of 10^8 or $10^{10}\,\frac{\mathrm{Gy}}{\mathrm{s}}$) due to a high acceleration by ultra-short and high-intensity laser pulses [Karsch et al. (2019);

Ehlert et al. (2021)]. Therefore, LAPs are of particular interest in radiobiology with respect to the novel so-called FLASH radiotherapy modality. This technique is based on ultra-high dose rates eliciting different radiation responses between normal tissue and tumor cells [Favaudon et al. (2014)]. The FLASH radiotherapy characterized by dose rates above $30\,\frac{\mathrm{Gy}}{\mathrm{s}}$ has shown normal tissue sparing while offering an unaltered tumor response [Montay-Gruel et al. (2019); Al-Hallaq et al. (2019); Kroll et al. (2022)]. Up to now, the underlying mechanisms of the FLASH effect have not been clarified. There are different hypotheses concerning dose rate effects and the influence of oxygen content on radiosensitivity. An overview is provided in Favaudon et al. (2021). Adrian et al. (2020) pointed out that the high dose rate causes oxygen depletion in normal tissue, leading to hypoxic and thus more radiation-resistant cells. On the contrary, the results of Labarbe et al. (2020) indicated a radical-radical recombination as the major mechanism of FLASH. The recombination leads to shorter lifetimes of the damaging radicals, which correlates with a reduced probability of normal tissue complications.

The extent to which LAPs can also induce a FLASH effect is still unknown. However, a recent work of Pawelke et al. (2021) shows, that electrons with a dose rate $\geq 10^9\,\frac{\mathrm{Gy}}{\mathrm{s}}$ produce a FLASH effect in zebrafish embryos [Kroll et al. (2022)]. Moreover, Raschke et al. (2016) have already proved that LAPs induce a similar DNA damage, but less immediate nitroxidative stress in comparison to conventional protons. They have supposed that this is due to the particularly high dose rate of LAPs. This implies a need for interdisciplinary research of FLASH radiotherapy and LAPs to investigate and compare the underlying radiobiological or chemical processes. In addition, comparing cellular radiation damages of conventionally accelerated protons at a clinical beam line and LAPs would be of particular interest for future developments.

The proton fields from a clinical proton therapy machine used in this project are intended to correspond to the typical energy range of the LAPs $(2.5 - 3.3\,\mathrm{MeV})$ generated with the Arcturus laser system at the Institute of Laser and Plasma Physics at the Heinrich-Heine-University Düsseldorf [Cerchez et al. (2019)]. There, a setup for the application of the generated LAP radiation is available: A vacuum chamber with two pinholes is used to spatially confine the protons to a narrow pencil beam. The latter is deflected by two magnet yokes, whereby the protons possess a defined direction and an energy dispersion. These kind of proton fields has already been used to verify an increased double-strand break induction with a higher LAP dose [Ehlert et al. (2021)].

For simplicity, the acronym LAP refers in the following to the particular energy range of $2.5 - 3.3\,\mathrm{MeV}$.

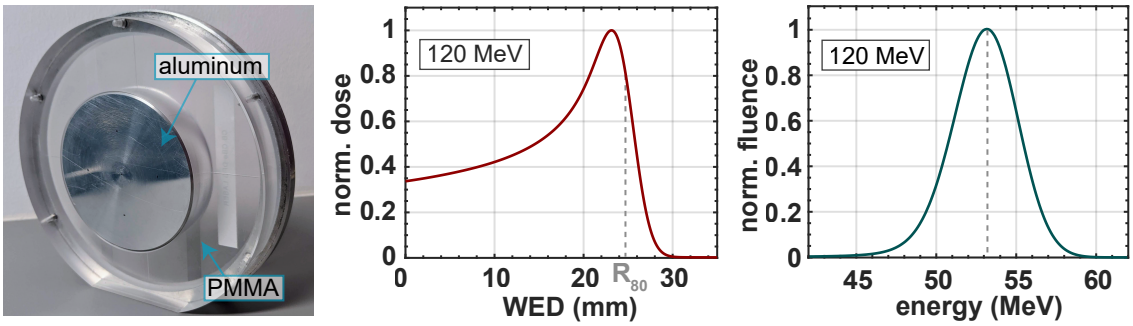

Figure 4.1.: Characterization of the aluminum range shifter: A photo is shown on the left, the simulated depth dose curve of initial 120 MeV protons downstream of the aluminum range shifter (middle part), and the resulting energy spectrum downstream (right).

4.2. Experimental methods and computer simulations

A setup is designed to be attached to the IBA universal nozzle for the fixed beam line at WPE (Section 2.3, Figure 2.4). The preparations and optimizations of the experimental setup with considerations about the absorber, the field design and detection for the low-energetic protons are presented in the following. In addition, the details on the Monte Carlo simulations of the energy spectra downstream of the various absorbers, as well as of the depth dose and LET of the degraded protons, are described.

4.2.1. Characterization of absorber materials

A range shifter block is designed for the snout of the WPE system. The material of the block has to fulfill the following properties: Since both, range straggling (Equation 2.8) and MCS, scale with the atomic number Z, a material with the lowest possible Z should be chosen. In addition, it should have a small temperature coefficient of expansion and in general it should be practical to fabricate in the in-house workshop. Based on these criteria, an aluminum alloy consisting of aluminum (94.8%), magnesium (4.5%) and manganese (0.7%) is used. The cylindrically shaped aluminum block is fabricated and laterally enclosed in PMMA to match the dimensions of a clinical range shifter for the snout holder. For details on thickness and WER, see below.

Figure 4.1 shows a photo of the aluminum range shifter (left). The DDC in water for protons with an initial energy of 120 MeV (range in water: 106.6 mm) is simulated downstream of the range shifter and scored for a simple model in TOPAS (more details in Section 4.2.3). The outcome is shown in the middle of Figure 4.1. The protons passed

through the aluminum range shifter still have a residual range of about 2.4 cm. This implies, that 120 MeV is well suited as an initial energy, since the entire Bragg peak can be observed downstream the aluminum range shifter, allowing normalization during post-processing. This energy provides enough flexibility to vary the total absorber thickness with additional material to study the resulting effect. The resulting energy spectrum downstream of the aluminum range shifter of the simple Monte Carlo simulation is shown on the right. On average, the remaining protons have an energy of 53.5 MeV.
In order to further reduce the energy and thus the range of the protons, solid water phantoms, hereafter called RW3-plates (SP34, type RW3, IBA Dosimetry, composition: 98% polystryrene + 2% TiO_2), are used. These are also included in clinical quality assurance routines and are available in nominal thicknesses from 1 mm to 10 mm. To facilitate smaller step sizes for the DDC measurements, 50 µm Mylar foils are utilized. The extrapolation ionization chamber (IC) also used for the measurements (Section 4.2.2) has an entrance window made of 25 µm Kapton. Figure 4.2 presents a schematic sketch of the variable absorber combinations (left part). For visualization, the varying shapes of energy spectra described in Section 2.1.4.2 are shown. In order to provide a very specific energy range, here that of the LAPs, an energy selection system would be necessary. The implementation at the institute in Düsseldorf (Section 4.1), in which a vacuum chamber with two slits and two dipole magnets is used, is sketched here as an example (Figure 4.2, dashed box, right). Even though the energy selection system will not be considered further on, it is shown for the sake of completeness. More details on this topic can be found in Raschke et al. (2016).
The Kapton layer represents the entrance window of the vacuum chamber. Since the extrapolation chamber also has a Kapton window (Section 4.2.2), it is included in the simulations (Section 4.2.3).

The physical thickness and the water-equivalent thickness of the absorber layers has to be determined with appropriate accuracy. The physical thicknesses of the Mylar films and the Kapton layer is specified by the manufacturer. The physical thicknesses of the aluminum range shifter and the RW3-plates is verified with the TESA-Hite magna 400 IP40 (Tesa Technology, Renens, Switzerland) measuring device with an accuracy of 1 µm. The thickness of the aluminum range shifter in the center region, where the beam incidences the block, yields 38.993(6) mm on average over its cross section with a radius of 45 mm. For the RW3-plates, in addition to the measured thickness, its homogeneity is checked in order to use plates with minimal roughness for the experiment. The details of the plates used are shown in Table A.1. The effort to select the plates is worthwhile, since considerable differences in the important µm-range are found.

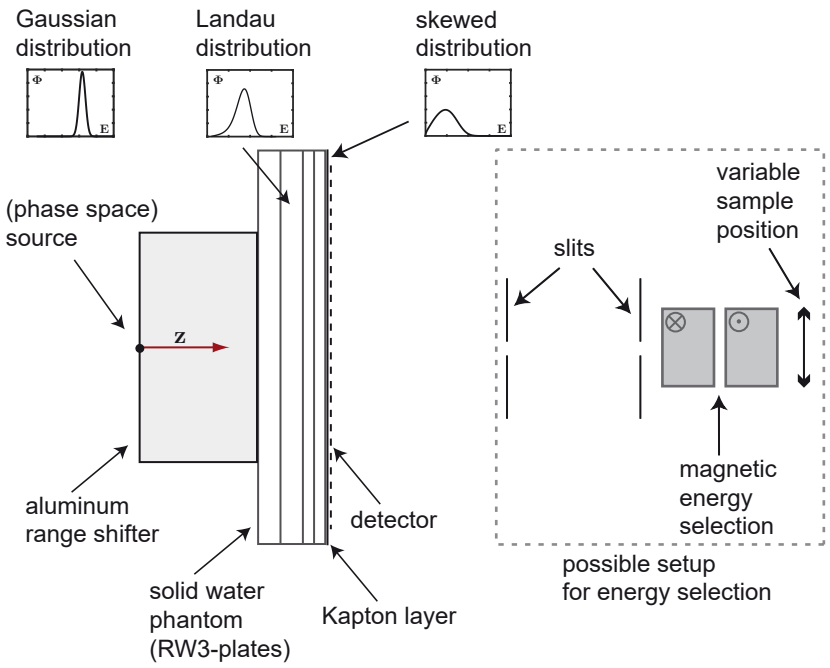

Figure 4.2.: Scheme of combined absorbers used for the experimental setup and modeled for the simulations (black part). The aluminum range shifter is combined with RW3-plates of different thicknesses. As an option, additional 50 µm Mylar foils are used, which are not shown here. The Kapton layer represents the detection entrance window of the extrapolation chamber, see Section 4.2.2, and is also implemented in the Monte Carlo simulations (Section 4.2.3). The development of the energy spectra with increasing absorber thickness is outlined in the three top insets. The part in the dashed box on the right sketches a possibility for energy selection from the resulting energy spectrum by means of slits and magnets as described in Raschke et al. (2016). Figure based on Behrends et al. (2021).

Table 4.1.: WER values of the different absorber materials used in the measurements for the water equivalent thickness from Behrends et al. (2021).

material	WER
aluminum alloy	2.093
RW3-plates	1.028
Kapton	1.309
Mylar	1.329

Methods for WER determination

- The WER (Section 2.4.1) of the aluminum range shifter is measured using a **multi-layer ionization chamber (MLIC)**, the Giraffe detector[1] (IBA Dosimetry, Schwarzenbruck, Germany). It consists of 180 air-filled ionization chambers, which have a diameter of 12 cm and are stacked at a distance of 2 mm in beam direction. This distance is reduced by measurements with an additional cover attached with its WET of 1.2 mm [Bäumer et al. (2015); Behrends et al. (2022)]. This detector is well suited for measuring the WET of materials, achieving high collection efficiency with its large cross-section when the MLIC is captured with single coaxial pencil beam spots [Bäumer et al. (2015)]. The sampled charge as a function of WED of the spot with 120 MeV protons is given as a measure of the dose, allowing the WET to be determined based on the ranges with and without the aluminum range shifter (Equation 2.14).

- **Stopping power calculations** based on the National Institute of Standards and Technology (NIST) database [Berger et al. (2010a)] are used to estimate the WER for the RW3-plates, the Kapton layer and the Mylar films. Based on the thin-target approximation (Equation 2.13) [Zhang and Newhauser (2009)], the WET is calculated representative for 1 cm of each material, which subsequently corresponds to the WER. This computation is not made for aluminum, since the aluminum alloy used has a different material composition than that available in the database.

- In addition, the above range analysis with the Giraffe detector is evaluated in **TOPAS simulations**. The range of the simulated DDC in water with and without absorbers is also evaluated with a Bortfeld fit [Bortfeld (1997)] and Equation 2.14 yields the WET for all materials.

[1] A photo of this detector can be found in Project *nano*, Section 5, Figure 5.2 (a).

In summary, the WER of the aluminum range shifter is determined from the average of the measurement with the Giraffe and the simulation in TOPAS at 120 MeV. For the RW3-plates, according to the energy dependence of the WER, the simulation is performed with an aluminum range shifter upstream and the energy 53.5 MeV is used in the computation. The WER for Kapton and Mylar is also averaged over the calculation with the NIST values and the simulation result from TOPAS. The averages of the determined WER values are listed in Table 4.1. Note that this value for aluminum nearly agrees with the WER of 2.069 calculated in Zhang and Newhauser (2009) for a comparable proton energy of 50 MeV.

4.2.2. Relative depth dose measurements

An experimentally challenging method of dose verification is needed. The conventional detectors in clinical quality assurance have a too thick entrance window for these µm-range protons and even Gafchromic EBT3 radiochromic films (Ashland LLC, Bridgewater, NJ, USA) still have an entrance window of about 125 µm with an active layer of 28 µm downstream (physical thicknesses). Therefore, only the cylindrical-shaped air-filled PTW extrapolation IC type 23391 (PTW, Freiburg, Germany) as a remaining detector is suitable for the dose measurements (Figure 4.3) [Physikalisch Technische Werkstätten (PTW) (1977)]. This chamber has an exchangeable entrance window (diameter = 60 mm) made of stretched Kapton, with the thinnest window of 25 µm is used for all measurements. This entrance window is located on one side of the cylindrical chamber and is coated with a graphite layer on the inside to serve as a conductive electrode. A second movable collecting electrode made of brass is positioned inside the chamber. It has a diameter of 30 mm and is surrounded by a guard ring at the same potential to ensure a homogeneous electric field. The distance, i.e. the air volume, between the entrance electrode and the collecting electrode can be adjusted with an uncertainty of 1 µm using a micrometer screw mounted on the rear side of the cylindrical chamber. For the following measurements, a distance of 2 mm is used between the electrodes and a voltage of 300 V is applied based on previous studies [Kern et al. (2020)]. The individual components are shown in Figure 4.3. The ionization events are detected due to the deposited charge in the air volume and read out by an electrometer (TANDEM, PTW, Freiburg, Germany) controlled by the software Mephysto Navigator (PTW, Freiburg, Germany, version 3.4). With this, the relative dose downstream of the absorber materials could be measured. The results are given in Section 4.4. In order to record the dose at different depths, the thickness of the absorber materials, i.e. the thickness of the entire buildup, is varied accordingly and a measurement is performed for every setup. In total, the measurements for the DDC are repeated six times over a time period of one month to check the reproducibility, i.e. fluctuations of

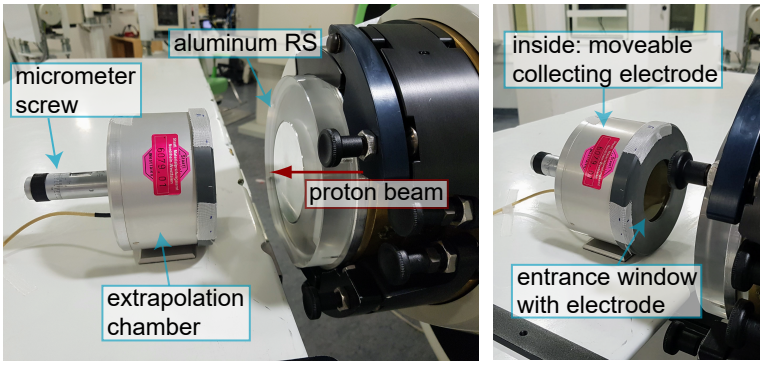

Figure 4.3.: The air-filled extrapolation ionization chamber type 23391 (PTW, Freiburg, Germany) at the fixed beam line with the aluminum range shifter for dosimetric measurements. Note, for a better view, no RW3-plates and Mylar foils are placed in the beam path.

the energy and range of the clinical proton beam. The chamber is aligned with the clinical x-ray system with an accuracy of 0.5 mm to the isocenter of the radiation system. In order to have sufficient space available for varying of the absorber materials and simultaneously to maintain a reasonably small air gap, the snout is positioned at 12 cm (i.e. at a distance of 12 cm from the upstream end of the range shifter to the isocenter). The measurement details with the various absorber combinations used for the depth dose measurements are listed in Table A.2. The overall setup, which is also simulated, is described in detail in the next section.

The protons experience different path lengths through the absorber due to their initial deflection angle. To improve the beam transmission and to ensure that all emerging protons have approximately the same energy, a specially tailored and scanned $2 \times 2\,\mathrm{cm}^2$ proton field is used for the measurements: For this purpose, the field is divided into "rings", whereby the central proton spots have an energy of 120 MeV and spots on the outer rings get a higher initial energy corresponding to the energy loss of the increasing path length. The latter is due to the beam divergence from the scanning system. In this case, however, an incorrect value for the divergence distance is used in the calculation leading to the fact, that the energies of the outer protons are somewhat too high (a maximum variation of 0.7 MeV). Anyhow, this does not affect the results below, since the same field with the same energies is used accordingly for the depth dose simulations.

4.2.3. Monte Carlo simulations in TOPAS

Monte Carlo simulations of the energy spectra as well as the depth dose and the LET are performed in TOPAS (version 3.5) as also used in Section 3.3.1.2. The design of the experimental setup presented in Figure 4.2 is implemented in TOPAS.

A phase space source with corresponding Fermi-Eyges parameters, as well as the mean energy and energy spread, is calculated for both simulation setups using the WPE beam line model for the FBTR [Verbeek et al. (2020); Bortfeld (1997); Clasie et al. (2012); Grassberger et al. (2014)]. The WPE beam model is based on measurement in air in the isocenter, from which the parameters for a position more upstream can be traced back. Since the data already includes the air scattering, the simulations are planned in vacuum to ensure the same conditions as for the measurements (in air). 10^9 primary protons are included in all simulations.

Based on the material compositions for the various absorber materials (see above), new material compositions matching the conditions are specified in TOPAS: For the aluminum alloy, the density of 2.66 $\frac{\mathrm{g}}{\mathrm{cm}^3}$ is obtained and for the RW3-plates of 1.045 $\frac{\mathrm{g}}{\mathrm{cm}^3}$. The electronic stopping power computations in TOPAS are based on the data of the International Commission on Radiation Units and Measurements (1993) Report 49 and for water on the International Commission on Radiation Units and Measurements (2014) Report 90. For that, the mean excitation energies as specified in International Commission on Radiation Units and Measurements (2014) are set: 166.0 eV for aluminum and 78 eV for water. Concerning the transport calculations, the production cut for all particles is defined according to a proton range in water ($2.458 \cdot 10^{-3}$ cm) with an energy of 1 MeV [Berger et al. (2010a)]. As default, a maximum step size of 1 mm is used. The physics lists *g4em-standard opt4, g4hphy QGSP BIC HP, g4decay, g4ion-binarycascade, g4h-elastic HP* and *g4stopping* are chosen based on the work of Jarlskog and Paganetti (2008).

Simulation of energy spectra As shown in Figure 4.2, the phase space source is calculated for the position of the upstream surface of the aluminum range shifter and one central spot is sampled. To simulate the energy spectra downstream for multiple absorber thicknesses, the aluminum range shifter, RW3-plates and the Kapton foil are used (details in Table A.2). The variation of absorber thickness is implemented by varying the RW3-plates' thicknesses. A cylindrical scorer volume placed directly downstream of the Kapton layer tallied the proton fluence with standard deviation and the number of histories. The detection volume of vacuum has a short extension in the beam direction (0.1 µm) but a large radius of 10 cm in lateral direction with a radial binning of 0.5 cm. The total number of scored protons is determined by numerical integration in polar coordinates over the whole cross sectional area of 20 bins. In addition, the scorer geometry is binned by energy up to 120 MeV in 1200 bins, i.e. energy bins of 0.1 MeV. The spectra are given in a relative efficiency, which is defined as the number of scored protons from the fluence relative to the initial proton number per energy given in the unit $\frac{\%}{\mathrm{MeV}}$. The values for total

efficiency, i.e. the integrals of the spectra, give the total relative efficiency with respect to the initial number of particles for a specific absorber thickness.

Simulation of the depth dose and the LET A phase space source, located at the upstream surface of the aluminum range shifter, which is here 12 cm upstream of the isocenter, is built with the same spot pattern of the $2 \times 2\,\mathrm{cm}^2$ field as designed for the measurements. A cylindrical scoring volume of water is placed with its upstream end in the isocenter plane. Only the aluminum range shifter is used as an absorber material, so the water volume serves as additional absorber material as well as for scoring purpose. The scoring volume diameter of 3 cm at the front surface corresponds to the electrode in the extrapolation chamber. Its length of 4 cm is divided into 800 bins. This allows a dose and LET scoring, as well as a calculation of their standard deviations, in beam direction (0.05 mm step size).

The LET (Equation 2.2) is most often computed by Monte Carlo simulations, since it is not an easy measurable quantity. TOPAS computes the proton LET as the deposited energy of all protons and secondary electrons per step length, i.e. considering all produced secondary electrons ($\Delta \to \infty$ in Equation 2.2). Besides a few test simulations for comparison, the choice of the influencing scoring parameters is mainly based on previous studies [Cortés-Giraldo and Carabe (2015); Granville and Sawakuchi (2015)]. Calculations are usually based on dose-averaged LET or fluence-averaged LET to get the local average LET of all protons in one voxel. In the following, the dose-averaged LET (LETd) is used since it is more meaningful in terms of RBE, considering the dose and therefore the energy deposition:

$$LETd = \frac{\Sigma_i^N E_{\mathrm{dep},i} \cdot LET_i}{\Sigma_i^N E_{\mathrm{dep},i}}. \tag{4.1}$$

This means, LET_i is multiplied with the deposited energy $E_{\mathrm{dep},i}$ for each step i. The sum of the LET values weighted by the energy deposition is taken and divided by the total energy deposition in the considered voxel [Granville and Sawakuchi (2015)].

Based on Granville and Sawakuchi (2015) and Cortés-Giraldo and Carabe (2015) the 'stopping power $\mathrm{d}E/\mathrm{d}x$ pre-step lookup' calculation method is used, which is implemented in TOPAS. Here, the LETd calculation is based on the stopping power of the proton energy of the pre-step. This avoids unrealistic LET values due to a potential restricted proton step length of a voxel boundary crossing. The parameter of maximum scored LET is kept by the default $100\,\frac{\mathrm{MeV}}{\mathrm{mm}} / \frac{\mathrm{g}}{\mathrm{cm}^3}$. In addition, as recommended in Granville and Sawakuchi (2015), the secondary electron production threshold is increased to 1 mm.

4.2.4. Uncertainty analysis

For the consideration of uncertainties in the measurements and simulations, a distinction is made between type A and type B ones [Joint Committee for Guides in Metrology (2008)]. All statistical uncertainties being treated as type A. For all other type B uncertainties, with its uniform probability distribution is assumed and the standard deviation is stated with the coverage factor $\frac{1}{\sqrt{3}}$.
Table A.2 shows the total experimental uncertainties. For the measured charge, there is a maximum statistical uncertainty of 0.9% for the six repeated measurements of each data point. To estimate the uncertainty for the WED, different quantities have to be considered: On the one hand, there is the long-term output fluctuation in the energy of 0.05 MeV at the facility. This affects an uncertainty in the range of 0.08 mm for 120 MeV protons in water [Berger et al. (2010a)]. On the other hand, the determination of the exact physical thicknesses of the RW3-plates and the aluminum range shifter have also some uncertainties that contribute to WED. Scaling these maximal uncertainties in physical thickness with the WER factor (Table 4.1) leads to an uncertainty equal or less than 0.1 mm in WET for all combinations of RW3-plates used and 0.027 mm for the aluminum range shifter. The quadratic addition of the uncertainties regarding range, WET and material combinations yields a maximal uncertainty of 0.1 mm in the total WED (compare Table A.2).
In the Monte Carlo simulations of the energy spectra, the uncertainty on the efficiency of the protons is given above the 10% level because the uncertainties become very large at very low numbers of protons. Above this 10% limit of each energy spectrum, the maximum relative uncertainty is found to be 1.1% in terms of efficiency. The simulations of the DDC show a maximum uncertainty of 0.1% in terms of dose.
The uncertainties in the WED result from the bin sizes in the simulations: this is 0.002 mm in the simulations of the energy spectra, which results from the energy binning of 0.1 MeV. For the simulation of the DDC and the LETd, the bin size of 0.05 mm is used for the uncertainty calculation. For a clear visualization of the results, only the experimental uncertainties are shown in the following.

4.3. Comparison of simulated energy spectra

Figure 4.4 presents the results of the Monte Carlo simulations of the energy spectra (Section 4.2.3). The relative efficiency is shown as a function of the residual proton energy with the absorber thicknesses as a parameter, i.e. different total WED. The change of the shape of the energy spectra of initial 120 MeV protons with varying absorber thicknesses consisting of different material layers changes as described in Section 2.1.4.2: For thinner absorber thicknesses, the scored energy spectra follow the Landau distribution with

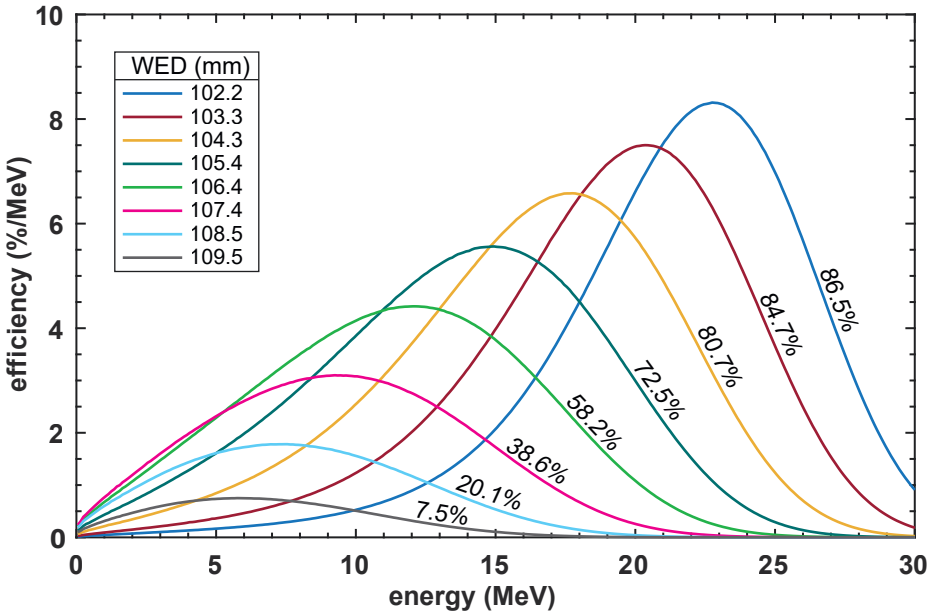

Figure 4.4.: Simulated proton energy spectra with an initial energy of 120 MeV downstream of different absorber thicknesses. In the setup, the water equivalent thickness of the absorber is varied. The aluminum range shifter with a thickness of 38.993 mm is combined with different thicknesses of RW3-plates and a Kapton layer (Figure 4.2). The relative efficiency, as a measure of fluence, is plotted as a function of the proton energy. The total efficiency with respect to the initial beam is written at each spectrum in percent. Figure based on Behrends et al. (2021).

the tail in the low-energy range. With increasing WED, more precisely from a WED of 106.4 mm, the energy spectrum becomes broader and skewed, since it is almost straight on the low-energy side and no Landau tail is visible. As expected, the skewness increases for even thicker absorbers. However, along the way, the overall efficiency decreases with increasing absorber thickness: For the thinnest absorber thickness (a WED of 102.2 mm), the overall efficiency is still 86.5%, while it has dropped to 58.2% in the case with a WED of 106.4 mm, and to 7.5% for the thickest absorber with a WED of 109.5 mm. The WED of 106.4 mm is emphasized, because it is close to the nominal range $R_{80} = 106.6$ mm of 120 MeV protons with an efficiency of about 50%. Accordingly, the skewed shape of the spectrum is observed as soon as about half of the protons in the absorber have stopped and no longer contribute to the spectrum.

The low-energetic spectra are analyzed in detail: For that, the spectra normalized to their respective maximum with large WED are given in Figure 4.5. This representation is helpful to investigate the physical processes in the low-energetic parts in more detail. There are more low-energetic protons at larger WED relative to the respective maximum efficiency. The slope of the efficiency for the low energies becomes steeper (almost linear)

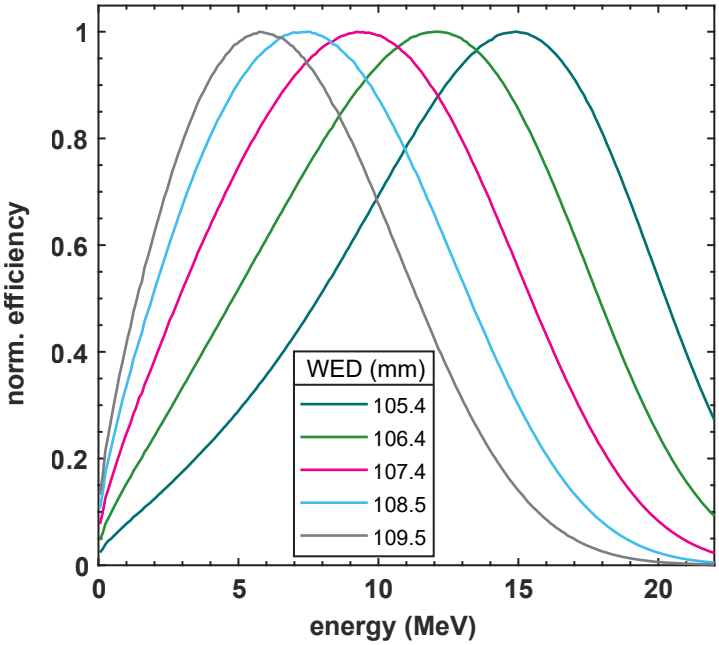

Figure 4.5.: Normalized energy spectra for the larger WED from Figure 4.4.

and the efficiency maximum is reached at a lower energy. As a result, the entire energy spectrum also becomes narrower at larger WED in the energy domain close to 0 MeV.

4.3.1. An optimal setup for the few-MeV level

Here, the spectra are analyzed in terms of an optimal setup, i.e. a setup in which the proton fluence is maximized in the energy range of interest. The special application of LAPs requires a setup for providing proton energies in the range of $2.5 - 3.3$ MeV, as discussed before. Based on this application, the optimal absorber thickness to be used will be determined based on the energy spectra. Figure 4.6 (a) shows the detailed overview of the energy spectra with respect to the energy range up to $4\,\frac{\mathrm{MeV}}{\mathrm{u}}$. This is a zoom-in of Figure 4.4 for the low energies. Since further applications are specified, the energy is now given per nucleon (N) in $\frac{\mathrm{MeV}}{\mathrm{u}}$: The energy of alpha particles from an americium (^{214}Am) source per nucleon is given, which is in a similar energy range as that of LAPs. Also shown is the natural energy limit (0.9 MeV) for irradiation of a mono-layer of cells, which typically have a diameter of 20 µm. As also outlined in Section 4.1, this represents the multiple applications of this particular low-energy region for radiobiological research. Figure 4.6 (b) illustrates the existence of an optimal setup, by presenting the efficiency as a function of WED. For each energy there is an optimum for maximum efficiency, with the optimum WED decreasing as the energy increases. For providing protons with 7.5 MeV or 10 MeV, a WED of 106.4 mm is optimal. At 5 MeV, both WED of 106.4 and 107.4 mm provide the same efficiency, but at lower energies 107.4 mm is preferable. Thus, for the

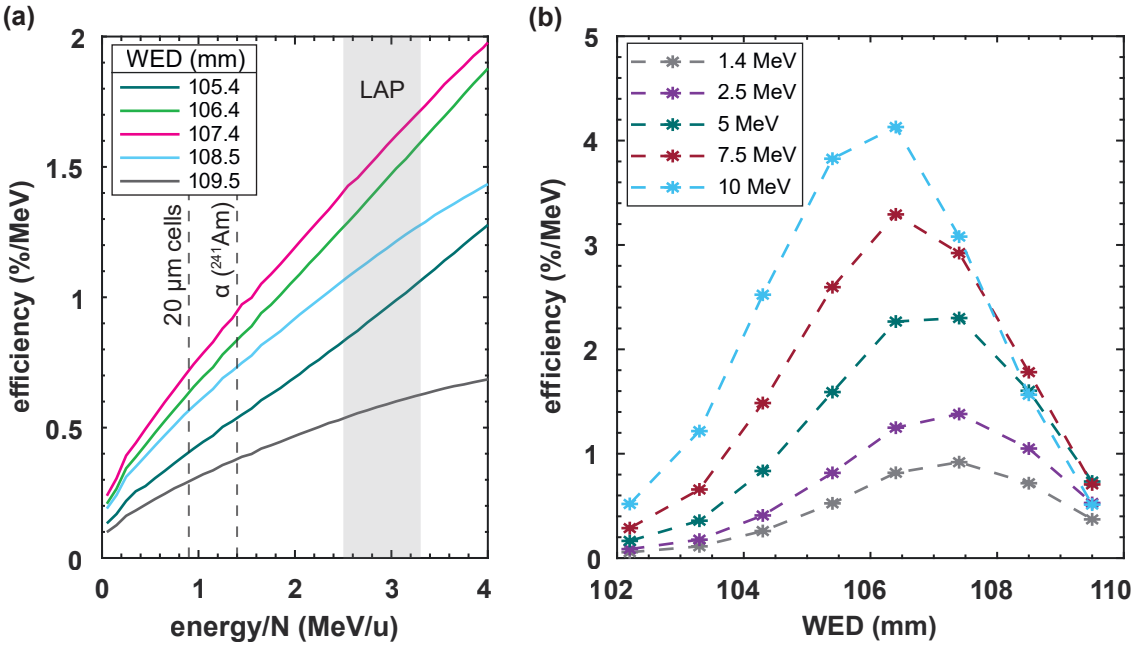

Figure 4.6.: Figure **(a)** shows the part of the energy spectra from Figure 4.4 up to 4 $\frac{\text{MeV}}{\text{u}}$ to better show the efficiencies in the low-energy region. Here the energy per nucleon (N) is given, since also the energy of the alpha particles per nucleon from an americium (^{214}Am) source (1.4 $\frac{\text{MeV}}{\text{u}}$) [Goodman et al. (1994)] is plotted as a possible application. The natural energy limit of 0.9 MeV for proton irradiation of 20 µm thick cells is marked as a dashed line. The gray shaded area indicates the energy range of the LAPs. For these applications, the maximum efficiency is found for an absorber with a WED of 107.4 mm. The relative efficiency as a function of WED is presented for different proton energies in Figure **(b)**. For each energy to be provided, there is an optimal absorber WED with maximum relative efficiency. The dashed lines are given to guide the eye. Figure based on Behrends et al. (2021).

specific energy range of the LAPs, as well as alpha particles or for irradiation of 20 µm cells, a WED of 107.4 mm can produce an optimal efficiency, with the produced energy spectrum having a total efficiency of 38.6% with respect to the initial beam.

4.4. Depth dose and LET on a small scale

In Figure 4.7, the DDC and the LET Monte Carlo simulations (Section 4.2.3) as well as the relative dose measurements for different WED using the extrapolation chamber (Section 4.2.2) are presented. The shown interval of the DDC with corresponding LET is limited to the region around the Bragg peak and R_{80} of the field, since this region is of special interest for providing the low energies, as previously discussed for the energy spectra. The measured values are given with error bars related to the WED as well as to the normalized dose. The normalized measurement values agree very well with the Monte

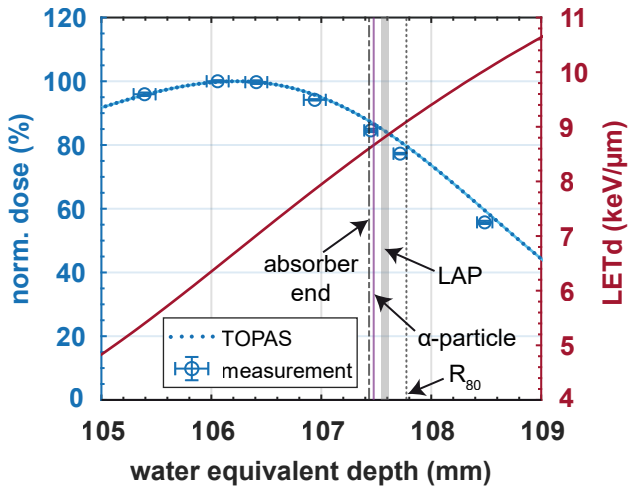

Figure 4.7.: Monte Carlo simulations of the DDC (left axis) and dose-averaged LET (LETd, right axis), as well as the measurements of the relative depth dose of the designed $2 \times 2\,\mathrm{cm}^2$ proton field for 120 MeV (Section 4.2.2). As shown by the color code, the left blue ordinate shows the relative dose, as do the blue graphs, and the right ordinate shows the LETd, as does the corresponding red graph. For the simulation of the DDC, the exact sampling points are denoted in dark blue and the linear interpolation in between in light blue. The measured values of the relative dose are shown at discrete depths with their standard errors. The LETd is calculated based on the electronic stopping power values of the pre-step proton energy, as explained in Section 4.2.3. Further information regarding possible applications is included: The dashed vertical line shows the downstream end of the absorber for an optimal WED (107.4 mm) based on the energy spectra and efficiency analyses. The residual range of protons at 1.4 MeV, the energy of the alpha particles per nucleon, is indicated by the purple line. The range of $2.5 - 3.3$ MeV protons for LAP application is also marked by the gray shaded area. Figure based on Behrends et al. (2021).

Carlo simulations of the depth dose in the Bragg peak region. They deviate only by about 0.1 mm in depth and by a maximum of 4% in the normalized dose at the distal end. The LETd shows the expected trend of a strong increase with increasing depth at the distal end of the depth dose curve. In the region of R_{80} the LETd reaches almost $9\,\frac{\mathrm{keV}}{\mu\mathrm{m}}$ and at the distal fall-off, where the dose has dropped to 50%, even almost $11\,\frac{\mathrm{keV}}{\mu\mathrm{m}}$.

The distal end of the optimal absorber thickness for the application of proton energies ≤ 5 MeV and thus in particular also for the LAP comparison is plotted by the dashed vertical line at 107.4 mm water equivalent depth, as determined in the energy spectrum and maximum efficiency analyses above. The violet line indicates the residual range of protons in water after leaving the absorber, at an energy of 1.4 MeV according to the comparison with alpha particles. The special application of providing the proton energies in the range of LAP energies is shown by the gray shaded area: This region corresponds to the residual ranges of the protons with $2.5 - 3.3$ MeV. As already observed in the

efficiency analyses, the depth region of the low-energetic protons is just upstream of the R_{80} of the initial proton beam. Moreover, these studies in Figure 4.7 show that the LETd for this low-energy region is about 9 $\frac{\text{keV}}{\mu\text{m}}$.

4.5. Discussion and conclusion of providing low-energetic proton beams

A method is presented to optimize the proton efficiency for radiobiological experiments using clinical protons degraded to energies in the few-MeV level.
Compared to other works that have provided proton fields with high LET, such as Guan et al. (2015) and Patel et al. (2017), this study particularly focuses on the underlying physical aspects and experimental challenges posed by very thick absorbers and strong degrading of the initial proton energy.

Energy spectra

The evolution of the shape of the energy spectra in the Monte Carlo simulation due to increasing absorber thickness is described by the theory of Tschalär and Maccabee (1970) and Bichsel and Hiraoka (1989), as given in Section 2.1.4.2. The underlying physical aspects with increasing absorber thickness can be found in the energy spectra of Figure 4.4. The increasing range straggling with WED, described by Equation 2.8, is evident from the increasing width of the spectra. In addition, the decrease in fluence with increasing WED appears in the decreasing efficiency, i.e. in the smaller integrals of the spectra. As stated in Section 2.1.3, the number of protons decreases with depth due to non-elastic nuclear interactions. However, this initially causes the fluence to drop only slightly over the path length. Since the optimal WED for protons with residual ranges of several micrometers is close to the protons' total range of the initial beam, the fluence is about 50% and decreases very sharply. This leads to the counteracting processes of a strong fluence decrease and an increasing range straggling for providing protons in the low-energy range. It explains the asymmetric shape of the energy spectra and the resulting optimum efficiency (Figure 4.6). However, the increasing range straggling is only evident in the spectra to a limited extent: The width of the spectra in Figure 4.4 increases with larger WED, due to the increased range straggling. But for very thick absorbers, the energy spectra's width decreases again, since the spectra approach 0 MeV (Figure 4.5).
In addition, some considerations are made concerning the formation of the skewed energy spectra shape: The steeper low-energy (almost linear) slope of the normalized energy spectra at larger WED could be generated by the increased number of ionizations at low

proton energies (Section 2.2.2). This increased LETd in larger depth corresponds to a lower proton energy (Figure 4.7). An increased ionization density leads to more low-energetic protons, which could explain the relatively increased number of protons at these energies (Figure 4.5 and Figure 4.6 (a)). Since the effective cross section of non-elastic nuclear interactions at proton energies $\leq 8\,\mathrm{MeV}$ is negligible (Section 2.1.3), these interactions would not make a relevant contribution to the number of low-energetic protons.
In the experimental setting, it is advantageous to optimize the beam transmission for low-energetic protons as much as possible, since many protons stop in the absorbers. One option is the correct choice of the absorber material. Since both, range straggling (Equation 2.8) and MCS increase with Z, the absorber material should be of low Z. As explained in Section 4.2.1, aluminum is chosen because it has a relatively low Z, has a small temperature coefficient of expansion, and is easy to use in the WPE facility. Aluminum thus represents a good choice with regard to the requirements. Theoretically, however, other materials would be even more suitable: Beryllium and graphite provide good conditions with atomic numbers of $Z = 4$ and $Z = 6$, respectively. Beryllium and carbon were compared as a degrader material in van Goethem et al. (2009) and they found even a 40% higher beam transmission for beryllium. Therefore, better results can be expected with such a thick absorber made of beryllium or carbon. Since beryllium is biologically harmful and carbon is usually brittle, an outer coating of aluminum would be advantageous.
The method presented here is intended to serve as a recipe for the production of low proton energies at clinical facilities. When transferring it to other facilities, variations in energy parameters due to other accelerator types are expected. While the lowest possible initial energy should be used, different cyclotron models vary concerning the minimum energy and energy spread. Compared to a synchrotron, the initial energy spread is larger for a cyclotron because a synchrotron varies the energy internally, i.e. it has no degrader. As an example, the beam parameters of the synchrotron from the Heidelberg Ion Beam Therapy Center are given: At low energies, the beam has a momentum spread of 0.3% [Parodi et al. (2012)], which is about a factor of three smaller compared to the WPE cyclotron. Due to the smaller energy spread, narrower energy spectra than those in Figure 4.4 are therefore expected for a synchrotron accelerator. Thus, the method would also likely be more effective at a synchrotron, since a higher number of protons could be achieved. However, the existence of an optimal setup is still expected, making the method presented here interesting for applications at other facilities with different accelerator parameters.

Depth dose and LET

This study provides a good validation method of the underlying computations of the physical interaction processes in the Geant4 TOPAS Monte Carlo Code. Since the simulations

and measurements with extreme proton scattering and stopping agree very well, the implemented physics in TOPAS models the energy loss and range straggling accurately.

It is obvious that a low initial proton energy should be chosen for this method in terms of efficiency per energy. An advantage of low energies is also evident in the LETd: The simulation result in Figure 4.7 indicates that in this study an LETd of about $9\,\frac{\mathrm{keV}}{\mu\mathrm{m}}$ can be achieved at an initial clinical energy of 120 MeV for the generation of proton energies ≤ 5 MeV. Compared to other works on radiobiological studies, this is not particularly high. In the simulations by Dahle et al. (2017) with initial energies of 80 MeV and 15.5 MeV, the achieved LETd values in the range of R_{80} are $15\,\frac{\mathrm{keV}}{\mu\mathrm{m}}$ and $30\,\frac{\mathrm{keV}}{\mu\mathrm{m}}$, respectively. While 15.5 MeV initial proton energy is far from an energy in clinical applications, the investigated 80 MeV is more representative of a clinical accelerator. Thus, the $9\,\frac{\mathrm{keV}}{\mu\mathrm{m}}$ achieved in this work represents a feasible value with respect to an initial 120 MeV.

When comparing the low-energetic protons with alpha particles, a distinction must be made between the energy of an alpha particle and the energy per nucleon (Equation 2.6). An alpha particle consisting of four nucleons has about the same range at four times the energy compared to a proton. In other words, alpha particles and protons have the same range at the same energy per nucleon. However, the total stopping power for alpha particles with four times the energy or the same energy per nucleon is about four times the stopping power for a proton in water [Berger et al. (2010a)]. And since the LET is a measure of stopping power (Equation 2.2), the LETd would therefore also be four times higher.

As a specified energy value is always a mean value of an energy spectrum, a given LETd is also a mean of an LET spectrum. In principle, the LET spectrum is broadened with increasing initial energy and WED. However, the LET spectra of different widths and shapes can of course reach the same mean LET value. Accordingly, the same LETd values can cause a different radiobiological effect due to a differently shaped LET spectrum. This aspect should be considered in radiobiological experiments and especially when comparing LETd values. Such studies on LET spectra including more details on this topic are presented in Dahle et al. (2017).

Another challenge, besides providing low proton energies, is their dosimetric detection at the µm-ranges. Here, the extrapolation IC (Section 4.2.2) is chosen for the relative dosimetry because all other available clinical detectors are not suitable. Generally, clinical detectors have an entrance window that is too thick, i.e. it is thicker than the protons' residual range. Alternatively, radiochromic films with suitable entrance window could be used [Sanchez-Parcerisa et al. (2021)]. In addition, calibrated photo stimulated image plates or solid state detectors CR39 are an alternative [Mančić et al. (2008)], as also used in Ehlert et al. (2021).

To compensate for small fluctuations from the accelerator, these measurements are repeated over a period of one month and the results are averaged. However, the small fluctuations show a good reproducibility of the ranges in µm-scales. Nevertheless, possible energy and range fluctuations should be taken into account for applications of this approach.

Applications of this approach and future efforts

With the provided low-energetic protons, cell experiments under the energetically same conditions as LAPs can be performed in order to compare the radiation effects [Ehlert et al. (2021)]. As already mentioned, with this method an energy spectrum is generated and an energy selection system would be required for a well defined proton energy. Such a system is of higher complexity than the simplified setup used in this work. It is indicated in the dashed box in Figure 4.2 and presented in the works of Raschke et al. (2016) and Ehlert et al. (2021). To address the increased scattering and fluence loss due to the additional slits in the vacuum chamber, further simulations of the energy spectra are performed. With a slit aperture attached to the absorbers (a WED of 107.4 mm), the fluence is scored as described in Section 4.2.3. A second slit is attached at the upstream end of the detector, i.e. 30 cm further downstream in vacuum. The distance of 30 cm is roughly estimated by the vacuum chamber's dimensions. The energy spectrum shows a comparable shape, indicating that the scattering at the slit is negligible. But, as expected, significantly less protons hit the detector: Behind the second slit aperture only 0.01% of the protons compared to the number directly behind the absorber material are detected. From the results presented in Figure 4.4 it is known that for a WED of 107.4 mm an efficiency of 38.6% with respect to the initial efficiency can be achieved. Thus, the total efficiency related to the initial number of particles behind the second slit aperture is only about 0.004%. This very low efficiency resulting from the combination of the simple setup with an energy selection system underlines the relevance of achieving a maximum efficiency and thus of the method presented here.
Furthermore, this method can be used for dosimetric studies, such as the response functions of detectors at low energies and close to the end of the depth dose curve.

Although the presented method optimizes the setup and presents a possible dosimetry procedure for studies with low-energetic protons from clinical proton therapy machines, a few practical challenges remain to be addressed in the future: Due to the strong degradation of protons and possible use of slit apertures, the fluence loss is high, so that the dose rate should be checked for cell experiments. In addition, a way to measure the energy spectra or selected energy should be implemented. Furthermore, Trinkl et al. (2017)

showed a larger secondary neutron production while using a range shifter. This motivates to consider and investigate the neutron contamination on the cells especially downstream of such thick absorbers as used for this method.

Conclusions

For this project, protons with *micro*meter residual ranges could be provided at a clinical PBS line. A setup is developed that degrades the energy of clinical protons as efficiently as possible. In principle, it is expected that additional material in the beam path, would lower the energy of the outcoming protons. This is true with respect to the resulting average energy spectra, but at one point it is not practical with respect to efficiency on the low-energy scale. This project shows, based on energy spectra simulations, that there is an optimal absorber thickness for delivering protons with energies $\leq 5\,\mathrm{MeV}$ and maximum efficiency starting with initial 120 MeV protons. The WED of the optimal absorber thickness is found here to be close to R_{80} of the initial proton beam, i.e. on the distal fall-off of the Bragg peak, where simultaneously the proton fluence strongly decreases and the range straggling increases. These physical processes with an opposite trend produce an efficiency maximum in the energy spectra.
The relative depth dose of the demonstrated measurement procedure agrees with the depth dose simulations within 0.1 mm in water-equivalent depth and within 4% in relative dose. In addition, the provided low-energetic protons reach a dose-averaged LET of $9\,\frac{\mathrm{keV}}{\mu\mathrm{m}}$.
Overall, this project presents an optimal setup for providing low-energetic proton fields at a clinical PBS facility with regard to radiobiological experiments. It allows experiments with proton energies of a few-MeV up to 230 MeV to be performed under comparable environmental conditions and one setup.
This method finds particular application in radiobiological studies, not least because of the associated high LET of the protons. While the setup for such radiobiological experiments with clinical protons is principally available, further investigations may address the remaining aspects, for example in terms of secondary effects.

5. Project *nano*: Investigations on the radiosensitizing effect of platinum nanoparticles in proton therapy

Studying the effect of metal nanoparticles (NPs) require an even smaller scale in proton therapy, which is at the *nano*meter level. Such NPs are of great interest for tumor control in radiotherapy due to their radiosensitizing effect [Schuemann et al. (2020)]. The general mechanism and the underlying radiobiological, physical or chemical processes have not been elucidated up to now. With regard to proton therapy, this project aims to contribute to this hot topic.

First, an overview of the application of metal nanoparticles in radiotherapy and especially in combination with protons (Section 5.1) is provided. Most studies are based on gold nanoparticles (AuNPs), which is why some considerations are presented for comparison with the platinum nanoparticles (PtNPs) used here. Then, the methods and experiments analyzing the energy deposition of PtNPs under proton irradiation are given in Section 5.2. Biocompatible surfactant-free PtNPs of $40(10)\,\mathrm{nm}$ diameter, with the capacity to induce a radiosensitizing effect via damaging reactive oxygen species (ROS), are used[1]. Tissue-like samples in terms of water content without and with a $300\,\frac{\mu g}{ml}$ PtNP concentration are employed for the following investigations (Section 5.2.1). For a simplified nomenclature, the samples with PtNPs will be referred to as *PtNP sample* in the following and those without PtNPs will be referred to as *nonPtNP sample*. CT imaging is used to characterize the tissue-like samples (Section 5.2.2), as well as to study the impact of the PtNPs on the treatment planning (Section 5.2.3). The proton energy deposition downstream of the samples is measured under different experimental methods described in Section 5.2.4. The WER as a measure of proton stopping, as well as the deposited energy downstream of the samples are compared. The results of the imaging and the treatment planning

[1] The manufacturing process of the PtNPs and the samples was performed by the Center for Nanointegration (CENIDE), University Duisburg-Essen.

analyses are presented in Section 5.3.
These experiments are published in an own publication, which is referred to once here to avoid frequent citations to it hereafter:

Behrends et al. (2022), *The radiosensitizing effect of platinum nanoparticles in proton irradiations is not caused by an enhanced proton energy deposition at the macroscopic scale, Phys. Med. Biol.,* ***67*** *155023, 2022.*

5.1. The power of metal nanoparticles in radiotherapy

By the definition according to ISO/TS:27687 [Organization for Standardization Technical Specification (2008)], nanoparticles are nanoobjects in which three external dimensions are on the nanoscale, which extends from about 1 nm to 100 nm. Thus, in general, NPs are characterized by a relatively large surface-area-to-volume ratio. Metal NPs in particular are specified by a high atomic number Z, ranging from titanium with $Z = 22$ to bismuth, $Z = 83$, resulting in a large interaction cross-section for photons, which makes the concept of enriching tumors with NPs fundamentally interesting for radiation therapy [Schuemann et al. (2020)]. For proton radiation interactions, the electron density of the material affects the energy deposition (Equation 2.6).
The combination of non-toxic metal NPs in radiotherapy presents a wide field with multiple applications and promising results. The versatile applications include diagnostics, in which the NPs can act as contrast agents, or in therapy, in which the NPs induce a dose enhancement effect through their radiosensitivity. Other applications are, for example, in immunotherapy or dosimetry. In terms of imaging, the use of non-toxic AuNPs as contrast agents for a CT has already been demonstrated [Hainfeld et al. (2013); Silvestri et al. (2016); Han et al. (2019)]. Schuemann et al. (2020) provides a road map with various potential roles of metal NPs in radiotherapy. Until now, most of the evidence is from pre-clinical studies. In Scher et al. (2020), the current status of a clinical application of the NPs in radiotherapy was reviewed. The most commonly used NPs in clinical studies are hafnium oxide and gadolinium, showing promising results such as increased radiotherapeutic efficiency by a dose enhancement but no toxicity. Hereafter, the focus is mostly on pre-clinical investigations in diagnostics and therapy of PtNPs ($Z = 78$).
In their pioneering work, Hainfeld et al. (2004) presented the radiosensitizing effect of AuNPs when mouse models are irradiated with x-rays: The long-term survival of the mice after one year was 86% for the combination of AuNPs ($270\,\frac{\mathrm{mg}}{\mathrm{ml}}$) with x-ray irradiation compared to 20% for irradiation only. The work demonstrated the preferential absorption of x-rays by high-Z NPs, leading to secondary electrons that ionize the surrounding

material and produce free radicals. This leads to a local dose enhancement [Schuemann et al. (2020)]. This motivates the potential of the AuNP enrichment in a tumor tissue for an induced local therapeutic dose enhancement effect. Due to the calculations of the ratio of absorption coefficients of a soft tissue and gold, a low x-ray energy in the keV range is more effective for the photoelectric yield and the dose deposited in the tumor [Hainfeld et al. (2008); Butterworth et al. (2012)]. These promising first results led to further experiments and simulations on AuNPs demonstrating the radiosensitizing effect with ionizing radiation, as presented in Mesbahi (2010) and Butterworth et al. (2012).
Beyond the application in photon therapy, the radiosensitizing effect of metal NPs or metallic complexes exposed to particle radiation is also being investigated [Lacombe et al. (2017)]: Usami et al. (2005) presented an enhanced DNA damage with platinum-containing molecules after irradiation with helium ions. On the cellular scale, the group demonstrated the enhancement effect of the platinum complexes *in vitro* with carbon ions [Usami et al. (2008)]. These studies in hadron therapy suggested a potential enhancement effect also for proton therapy. Using mouse tumors, Kim et al. (2010) demonstrated the proton radiation enhancement effect for AuNPs and iron NPs for the first time. An increased biological effectiveness of protons combined with AuNPs was *in vitro* confirmed by Polf et al. (2011), with prostate tumor cells enriched with AuNPs showing a $15-20\%$ increased killing efficiency. Moreover, an LET-dependent radiosensitizing effect of AuNPs in proton fields was observed by Li et al. (2016), showing a larger effect for a higher LET.

5.1.1. Considerations in radiotherapy with metal NPs

Although there are already a lot of important results in radiobiological research with metal NPs, the underlying physical, chemical and biological effects of enhancement mechanisms are inconclusive [Schuemann et al. (2020)]. Considerations for this are presented in this section, as well as further physical aspects that are related to this project.

5.1.1.1. A physical explanation on the radiosensitizing effect?

Various approaches explaining the radiosensitizing effect of metal NPs are discussed in the literature.
On the one hand, particle-induced x-ray emission (PIXE), in which protons kick out innershell electrons from the atoms and the vacancy is filled by an outer electron under characteristic x-ray emission, is an explanation of the proton therapy enhancement effect stated by Kim et al. (2010) and Polf et al. (2011). But Dollinger (2011) and Le Sech et al. (2012) disagree with this PIXE-based interpretations. According to the stopping power

computations of Dollinger (2011), the transferred proton energy to the NPs is too small to induce such a PIXE effect.
On the other hand, based on the argumentation of Le Sech et al. (2012), the effect can be explained by a secondary electron induced Auger effect: The secondary electrons generated by proton interactions on their primary path induce an inneratomic Auger cascade in the NPs leading to an Auger electron emission. In other words, the generated hole by the removal of an innershell electron is occupied by an outershell electron, transferring its energy to another atomic electron, which is released as an Auger electron. This secondary electron energy conversion into Auger de-excitation induces an additional radiolysis of water producing more free radicals. Based on this described conversion of secondary electron energy, Le Sech et al. (2012) concluded that the enhancement effect cannot be explained by an increased proton energy deposition. Monte Carlo studies, as presented in Wälzlein et al. (2014) and Cho et al. (2016), corroborated a microscopic local enhanced dose effect in the immediate vicinity of the NPs due to Auger electrons [Lacombe et al. (2017)].
The two different approaches discussed in the literature are competing processes. De-excitation of high-Z materials can occur via the PIXE or Auger process, whose probability depends on Z. It is known, that the fluorescence yield, i.e. the probability that an x-ray photon is emitted, increases strongly with Z after excitation of an innershell electron [Bambynek et al. (1972)]. Accordingly, an innershell Auger de-excitation would be rather unlikely for AuNPs and PtNPs, which contradicts the argument of an innershell electron de-excitation via the Auger effect as described in Le Sech et al. (2012). Wälzlein et al. (2014) considered that the probability of an Auger effect depends on the origin of the ionized electron. They argued that, based on ionization cross sections, outershell electrons are more likely to be removed, which increases the probability of the Auger effect, due to a lower fluorescence yield of outer shells.

In addition to the previous interpretations, the radiosensitizing effect of metal NPs is explained from the chemical side. Sicard-Roselli et al. (2014) argued with a much more efficient radiolysis of water in the vicinity of AuNPs - in this case for photon radiation. In their work, different pathways of photon-NP interactions were investigated, finding a too low efficiency of photon and electron emission to generate the observed amount of radicals. In contrast, they justified the effect by catalytic-like reactions at the interface between water molecules and the NPs: A structured alignment of the water layer around the NP weakens the H-OH bonds, which favors radiolysis of the water and thus radical production [Sicard-Roselli et al. (2014)]. Gerken et al. (2022) supported the hypothesis of a catalytic effect, stating that the increased ROS formation at the surface is dependent

on the NP material composition.
Although there is a dispute in the NP community regarding the interpretation of the radiosensitizing effect and thus the observed dose enhancement, the fundamental role of the damaging ROS through radiolysis of water is frequently mentioned [Usami et al. (2005, 2008); Kim et al. (2012); Sicard-Roselli et al. (2014); Li et al. (2016); Schlathölter et al. (2016); Smith et al. (2017)].
A surface effect for the AuNPs sensitizing effect with proton radiation was observed in chemistry by Johny et al. (2022a), where a larger ROS generation for a larger total particle surface area could be observed, meaning that small particles are more effective. Similar results were observed by Zwiehoff et al. (2021), who showed, based on AuNPs and PtNPs, that the enhancement of a proton therapy efficacy is a surface-driven and not a mass-dependent effect. It is concluded that not the NP size is crucial for the ROS generation, but rather the number and type of surface atoms (for the latter see Section 5.1.1.2). These findings pave the way towards a deeper understanding of the metal NPs radiosensitizing effect from a chemical point of view.

5.1.1.2. Are platinum NPs "better" than gold NPs?

As presented, many important results have been achieved with AuNPs in the radiotherapeutic research, however platinum is also a promising candidate [Porcel et al. (2010)]. The simulations in Wälzlein et al. (2014) have determined an Auger electron yield for Pt that is almost twice as high as for Au. Zwiehoff et al. (2021) also investigated the characteristics of the surface atoms choosing Au, Pt and a combination, $Au_{90}Pt_{10}$ (subscripts: mixing ratio), as materials for the NPs with a similar diameter ($\approx 3\,\mathrm{nm}$) and therefore same surface area. Thereby, PtNPs revealed a significantly higher ROS yield compared to AuNPs and $Au_{90}Pt_{10}$ NPs.
A comparison of the Pt and Au properties potentially affecting the proton energy deposition shows no major differences: Both atoms have a similar atomic number Z (Au $= 79$ and Pt $= 78$) and similar relative atomic masses A (Au $= 197\,\mathrm{u}$ and Pt $= 195\,\mathrm{u}$) giving the almost same effective ratio of $\frac{Z}{A}$. Although the first ionization energy of Pt ($9.0\,\mathrm{eV}$) is slightly lower than that of Au ($9.2\,\mathrm{eV}$), the mean excitation energy driving the energy deposition according to the Bethe-Bloch formula (Equation 2.6) is $790\,\mathrm{eV}$ for both cases. The definition of the mass stopping power (Equation 2.1) implies an increase in the stopping power with density. The density of platinum is $21.45\,\frac{\mathrm{g}}{\mathrm{cm}^3}$ and the density of Au is $19.32\,\frac{\mathrm{g}}{\mathrm{cm}^3}$. The values also lead to a comparable electron density of Au and Pt. Therefore, these considerations of physical energy deposition do not explain the observed enhancement effect, but make an effect at the chemical stage more likely. However, they highlight

again the need for the experimental studies on this issue and motivate the following experiments. In Zwiehoff et al. (2021), different chemical reactivities of the AuNPs and PtNPs surfaces were suspected.
Given the material-dependent ROS-based enhancement effect of proton therapy according to Zwiehoff et al. (2021), the PtNPs are selected for the following studies of this project.

5.2. Experimental methods of the radiosensitizing effect of PtNPs

5.2.1. Manufacturing and characterization of the samples

The production of the tissue-like samples with and without PtNPs is carried out in cooperation with the Center for Nanointegration (CENIDE) of the University Duisburg-Essen, which is why only the most important specifications of the samples are presented here. All details can be found also in Behrends et al. (2022).
Briefly, the sample production process includes the steps of laser ablation in liquids [Waag et al. (2021)], centrifugation for PtNP extraction, transmission electron microscopy for the NPs' size determination, and gelation, which is illustrated in Figure A.1. The PtNPs used have a mean particle diameter of $d_{\text{mean}} = 40(10)\,\text{nm}$. To produce tissue-like samples, that are variable in thickness and manageable in the experiment, gelatin cuboids with and without PtNPs are used. The PtNP sample has a concentration of $300\,\frac{\mu g}{ml}$, which corresponds to a percent weight of $0.03\,\text{wt}\%$ platinum in the gelatin solution. The cuboids have a base area of $30 \times 30\,\text{mm}^2$ and a height of about 20 mm, which corresponds to the path length of the proton beam through the sample in the experiment. Therefore, it is extremely important for accurate results to consider the exact height of the samples. Due to the softness of the gelatin, it is difficult to determine the physical height of the samples, which is why in the following the quantifiable ratio of the heights of the samples to each other and their WET (Section 2.4.1) will be used (Section 5.2.2).
Furthermore, since the increased efficiency of a proton therapy is quantified by the increased number of damaging ROS, it is ensured that the produced PtNPs generate ROS upon proton irradiation. For that, PtNPs of different concentrations in water phantoms combined with an ROS dye were irradiated with 100 MeV protons. In general, the experiment is performed like the measurements in Zwiehoff et al. (2021). Figure A.2 shows, the higher the concentration of PtNPs in the colloid, the higher the ROS production. Thus, the generation of damaging ROS of the used PtNPs under proton irradiation is validated. To achieve the greatest enhancement effect, the concentration of $300\,\frac{\mu g}{ml}$ is used for the PtNP gelatin samples.

5.2.2. CT imaging with PtNPs

CT images are taken of two sample cuboids with and without PtNPs to investigate the properties of the PtNP samples in terms of homogeneity or geometric dimensions. Further, the imaging contrast due to the PtNPs for a clinical application as contrast agents and their influence in treatment planning is studied. For this purpose, the clinical scanner Brilliance Big Bore scanner (Philips, Hamburg, Germany) with a tube voltage of 80 kV, a tube current of 250 mA and a high resolution protocol with a reconstructed pixel width of 0.65 mm is used. To avoid artifacts, for example during reconstruction at sharp edges, the samples are placed diagonally to the CT axis. Thus, they do not interfere with each other. Nevertheless, at this point it would have been better to place the samples in an additional phantom to account for the beam hardening. However, this is not easily doable due to the soft properties of gelatin and the dimensions of the sample, so edge artifacts in the samples are taken into account in the analysis.

The RayStation clinical TPS is used to subsequently create the outer contour of the sample cuboids by means of gray level, meaning according to a line of equal HU values. To exclude the marginal parts, regions of interest (ROIs) contracted by 5 mm are established to evaluate the mean HU values of the sample. The mean HU value, $\overline{CT_{\text{num}}}$, as well as its standard deviation, of all voxels included in the contracted ROI are calculated.

Since this is only done for a control sample of HU values, i.e. a limited number of voxels in the contracted ROIs and a limited number of scanned samples, the standard error of the determined mean HU value, $\sigma_{\overline{CT_{\text{num}}}}$, is an appropriate measure of the deviation of the true population mean. In order to estimate the number of independent samples, the initial CT resolution is experimentally estimated to 1.52 mm by determining the FWHM of the intensity distribution of a scanned thin wire. With that, the standard error of the mean HU value, $\sigma_{\overline{CT_{\text{num}}}}$, is calculated.

The enhanced CT contrast induced by the PtNPs is defined as the difference of the mean HU value for the PtNP sample, $\overline{CT_{\text{num}}}(\text{PtNP})$, and the mean HU value for the nonPtNP sample, $\overline{CT_{\text{num}}}(\text{nonPtNP})$:

$$\Delta\overline{CT_{\text{num}}} = \overline{CT_{\text{num}}}(\text{PtNP}) - \overline{CT_{\text{num}}}(\text{nonPtNP}). \tag{5.1}$$

Sample thickness analysis As already outlined in Section 5.2.1, the physical thickness of the samples is needed to evaluate the experiments, which is difficult to measure. In order to determine the samples' thicknesses as accurately as possible, the CT contrast (Equation 5.1) is used. The extension of the samples is defined at their 50% density level, i.e. at 50% of their gray level profile. Since $\Delta\overline{CT_{\text{num}}}$ is related to the contracted ROI and thus to the 100% density level and the HU values are approximately linear to the density,

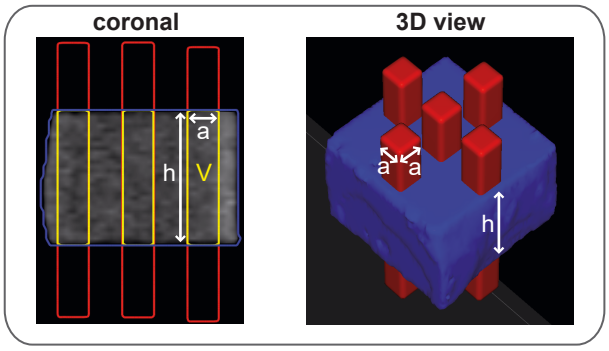

Figure 5.1.: Method for the sample thickness estimation in CT images in a coronal view (left) and a 3D view (right). Well-defined matchstick-shaped volumes (shown in red) with a cross-sectional area of a^2 and their intersection volumes V (yellow) with the outer contours of the samples (blue) are used for the determination of the sample thickness h. Details are described in the text. Figure based on Behrends et al. (2022).

the 50% density level corresponds to half of the CT contrast. Applying this knowledge, the outer contours of the samples are re-contoured, for two different clinical HU windowings, the lung window and the brain window, for comparison. This method allows the outer contours of the samples to be created under the same contrast conditions, which are illustrated in Figure 5.1 in blue.

Matchstick-shaped volumes (red in Figure 5.1) with well-defined lateral dimensions are finally used to determine the thicknesses of the sample. These are arranged in a way, that their long side lengths correspond to the sample thickness to be determined, i.e. are parallel to the beam direction, and the small cross section is perpendicular to the beam. Using the volume V of the intersection of the matchstick-shaped volumes and the outer contour (intersections shown in yellow in Figure 5.1), the long edge h corresponding to the thickness of the sample can be determined by considering the known dimensions a^2 of the small cross-sectional area: $h = \frac{V}{a^2}$. Calculations are made for five matchstick-shaped volumes at different lateral positions (Figure 5.1) to identify variations in the sample thickness. Since the thickness of the samples determined in the CT depends on the selected HU window, i.e. the gray level scale, the ratio H of the thicknesses

$$H = \frac{h_{\mathrm{PtNP}}}{h_{\mathrm{nonPtNP}}}, \tag{5.2}$$

which is independent of the CT scale, is extracted. Here, h_{PtNP} and h_{nonPtNP} are the averaged sample thicknesses at the same gray level windowing. For the final calculation of H, both clinical HU window presets for lung and brain images are used and eventually averaged.

5.2.3. Dose calculation with PtNPs

The influence of PtNP-enriched tumors on the treatment planning, more specifically on the dose calculation, is investigated using the above determined CT contrast. The idea is to make use of the HU to density proportionality. The original CT is copied and the mean density in the planning target volume (PTV) for the simulation with PtNPs is increased by $\Delta\rho$ according to the mean CT contrast $\Delta\overline{CT_{\text{num}}}$ (Equation 5.1). Then, the originally highly conformal dose distribution is subsequently recalculated on the CT with the overwritten PTV's density. The dose coverage of 95% and 98% of the PTV's volume ('original') is compared to the PTV with overwritten density ('overwritten'), respectively. For both dose volume statistics, the difference in dose coverage is calculated as

$$\Delta D_V = \frac{D_V(\text{original})}{D_V(\text{overwritten})} - 1 \tag{5.3}$$

with $V = \{95\%;98\%\}$ giving $D_{95\%}$ and $D_{98\%}$ the dose in the PTV's volume with original or overwritten density, respectively.
For this brief analysis, three pediatric study patients with brain tumors of slightly different locations are evaluated, two with ependymoma and one with medulloblastoma. These locations are likely to benefit from an radiotherapy with higher efficacy.

5.2.4. Setups for the measurements of the depth dose curves

In these measurements, the energy downstream of the PtNPs and nonPtNPs will be evaluated in comparison to detect differences in proton energy deposition due to the presence of PtNPs. For these experiments, both a gantry room with the PBS technique (Section 2.3.3.2) and the eyeline with the single scattering technique (Section 2.3.3.1) are used at WPE. In order to measure the energy deposition downstream of the samples as versatile as possible, three different setups are used, all described in Behrends et al. (2022), of which only two evaluating the depth dose distributions are presented in this section. The third measurement setup determines the deposited charge in terms of energy deposition downstream of the samples with a pixelated semiconductor counting-mode detector for high energy physics tracking experiments. It is applied in the context of a cooperation with the TU Dortmund University and is therefore not primarily part of this thesis. For the sake of completeness, it is given in Section A. More details to the application in proton therapy measurements of this specific detector can be found in Schilling et al. (2022a,b).

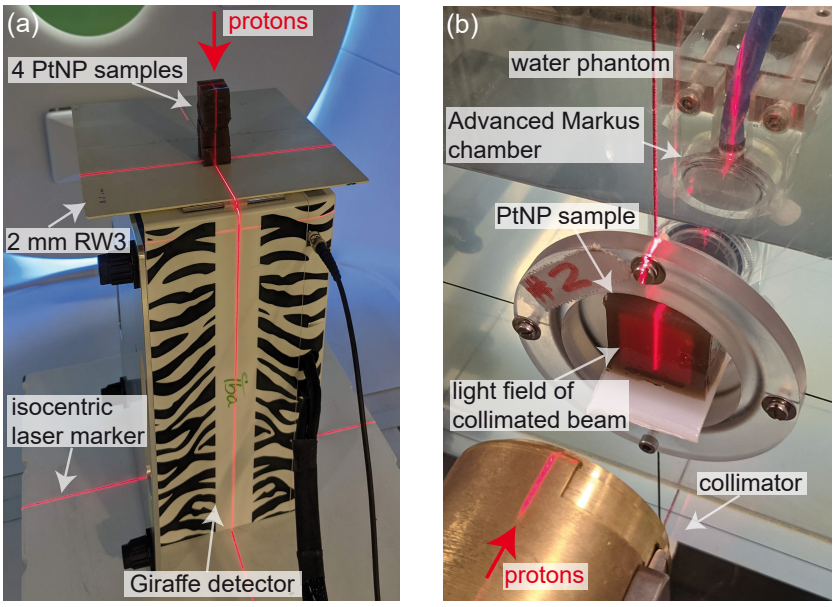

Figure 5.2.: Setup of the depth dose curve measurements for two methods: **(a)** illustrates the setup with the vertically aligned Giraffe detector and four stacked cuboid PtNP samples. The monitoring of the depth dose curves downstream of one PtNP sample cuboid at the eyeline using the motorized water phantom and the Advanced Markus chamber is shown in **(b)**. Figure from Behrends et al. (2022).

5.2.4.1. Multi layer ionization chamber - Giraffe detector

Depth dose distributions of mono-energetic pencil beams downstream of the sample with and without PtNPs are evaluated at a PBS beam line equipped with an IBA PBS dedicated nozzle (Figure 2.4 (b)). For this purpose, the MLIC Giraffe detector is selected (details in Section 4.2.1). In order to place, align and stack the gelatin samples optimally to the beam, the detector is tilted so that the beam is irradiated at a gantry angle of 0°. A photo of this setup is given in Figure 5.2 (a). To optimize the stability of the positioned samples, an additional 2 mm thick RW3-plate (with a WET of $\sim$ 2.06 mm) is placed on top of the detector. In addition, the detector in upright position and the centered sample are aligned in the isocenter with the help of the clinical positioning laser system. A single co-axial proton spot is employed, to ensure that, ideally, no protons are scattered laterally out of the small samples. Further, as mentioned before (Section 4.2.1), such single spots are well suited for measurements with ICs of large cross sections.

The energy deposition is measured in terms of DDCs downstream of the PtNP and nonPtNP samples, and without any sample via the charge counts in the stacked ICs of the Giraffe detector. As described in Section 4.2.1, an additional WET cover serves to reduce the sampling distance from 2 mm to about 1 mm. Each sample is made thicker by stacking several gelatin cuboids to be most sensitive to possible range reduction due to

increased energy deposition in the PtNP sample. The Bragg peaks downstream of the various samples are measured one after the other. In order to additionally investigate the influence of the proton energy, measurements are performed at 100 MeV, 140 MeV, 170 MeV and 200 MeV, respectively, with initial spot sizes of $\sigma_s = 5.4$ mm, 4.1 mm, 3.7 mm and 3.1 mm. In all measurements, two cuboids are stacked per sample type and an additional stack of four cuboids each is set up for the measurements at 200 MeV. The latter can be seen in Figure 5.2 (a) for the PtNP sample.
The data are recorded using the software OmniPro Incline (IBA Dosimetry, Schwarzenbruck, Germany, version 1.1.2.0).

Additional measurements for reproducibility and reproduction of the WET
In order to estimate experimentally the uncertainties of the WET, additional measurements for reproducibility and its resolution are performed with the Giraffe detector. For the reproducibility estimation, the range is measured with reduced sampling steps through the WET cover in seven repetitive measurements for 100 MeV and six measurements for 200 MeV. The dispersion of the R_{80} for both energies is given by the standard deviation of all values for the R_{80} determined by the Bortfeld fit [Bortfeld (1997)].
To estimate the WET resolution experimentally, the R_{80} is measured at an average energy of 150 MeV with and without a 1 mm RW3-plate in the beam path to find its WET. The difference of the measured and known WET of this RW3-plate (Table 4.1) is calculated. As a measure for the resolution, the standard deviation from this difference as an interval is estimated with the coverage factor of $\frac{1}{\sqrt{12}}$.

5.2.4.2. Plane parallel ionization chamber - Advanced Markus chamber

The eyeline with the single scattering technique and the dedicated nozzle (Figure 2.4 (a) and Section 2.3.3.1) is used for the depth dose measurements for energy modulated fields. Due to the small residual proton range of at most 35 mm, only one sample cuboid is placed in the beam path for these measurements. A square aperture is mounted to the nozzle, which limits the field to $20 \times 20\,\text{mm}^2$. This is visible in the light field in Figure 5.2 (b). Passively scattered fields with a residual range of 35 mm and a modulation width of 35 mm (R35M35), and a residual range of 27 mm and a modulation width of 28 mm (R27M28) are applied. The initial proton energies upstream of the samples vary between 56 and 64 MeV [Berger et al. (2010a)].
To record the relative DDCs with the PtNP and nonPtNP sample in the beam path, and also without a sample, the combination of an IC and a water phantom is used, varying the position of the chamber in the water depth (Figure 5.2 (b)). The PTW34045 Advanced

Markus chamber (PTW, Freiburg, Germany), a plane-parallel IC, is used, which is implemented in the clinical quality assurance at the eyeline and because it has a small volume and a small entrance window. The latter, more precisely, is composed of an entrance foil made of 0.03 mm polyethylene and a protection cap for the use of the chamber in water of 0.87 mm PMMA. To detect and then compensate for the dose rate variations in the beam while measuring different positions, an additional reference chamber positioned upstream in the beam path is used, the Semiflex 31010 (PTW). A modified MP3 XS water phantom (PTW) is motorized enabling the movement of the IC, in this case the Advanced Markus chamber, along three axes. Using a crossline and inline profile measurement, i.e. the two axes perpendicular to the beam, the Advanced Markus chamber is positioned in the field center. The water phantom has an extra thin entrance window in the area used for the measurements, in which the sample is placed with the help of an additional pad, see Figure 5.2. During the commissioning of the eyeline, a value of 2.42 mm was determined for the WET of the Advanced Markus chamber together with the wall of the water phantom [Koska and Wulff (2021)]. With this setup, the Advanced Markus chamber is scanned in depth for 0.1 mm steps and so the DDC is measured.
Charge counts are measured with the TANDEM electrometer as used in Section 4.2.2. Similarly, the Mephysto software is utilized to record the measurement data for both chambers and to correct the data of the Advanced Markus chamber with those of the reference chamber.

5.2.5. Data analysis and interpretation

The charge counts collected from the stacked ICs of the Giraffe detector are analyzed by Matlab (MathWorks Inc., Natick, MA, USA, R2019a): The measurements with and without the additional WET cover are combined to achieve the reduced sampling, and then normalized to their maximum charge value. Since no R_{80} values are intended to be determined, only the difference of the range with and without sample is considered here. Also, the WET of the Giraffe detector and the 2 mm RW3-plate are not included in the WED at this point for the sake of simplicity. The range R_{80} is determined by a Bortfeld fit to the data, describing the shape of a Bragg peak [Bortfeld (1997)].
An analysis of the DDC data from the eyeline measurements is also performed in Matlab, correcting the data for the known WET of the phantom wall and the chamber. Subsequently, a function for the analysis of a SOBP from the quality assurance routine is applied. Here, the maximum in the SOBP plateau is determined using an iterative process until convergence to normalize the data, where the plateau is generally defined by 95% proximal to 90% distal. Afterwards, the R_{80} is determined for every SOBP.
For further calculations in both analyses, the range values are not corrected for a potential

difference in thickness of the samples, since samples of equal thickness are initially assumed for this experiment. Only for the visualization in the plot of the DDCs, the WED is corrected based on the difference in physical thicknesses to be comparable in the graphical representation. However, for the following calculations, the thickness differences are accounted for in the uncertainty analysis. Thus, for all depth dose measurements with PtNP sample, with nonPtNP sample or without any sample, and for both setups, the R_{80} is determined.

To compare the energy deposition in the PtNP and nonPtNP samples, the WET (Section 2.4.1, Equation 2.14) is determined with the range measurements for each initial proton energy E_0. It is worth mentioning that the material in this case corresponds to the particular sample. Then, the WER is calculated based on Equation 2.15.

Quantification of differences in the energy deposition in the PtNP and nonPtNP sample is determined by the ratio of the characteristic WER of the samples:

$$WER_{\text{ratio}}(E_0) = \frac{WER_{\text{nonPtNP}}(E_0)}{WER_{\text{PtNP}}(E_0)} = H \cdot \frac{WET_{\text{nonPtNP}}(E_0)}{WET_{\text{PtNP}}(E_0)} \tag{5.4}$$

with the subscripts 'nonPtNP' and 'PtNP' for the used samples. This definition eliminates the not exactly known physical thicknesses of the samples, and requires only the well-defined ratio H (Equation 5.2). Hence, a WER_{ratio} less than 1 indicates an increased stopping power of the PtNP sample, so in the presence of PtNPs.

An additional analysis of the absolute count values of the measurements with the Giraffe detector is performed to determine some potential effects of nuclear interaction between protons and the PtNPs. By normalizing to the maximum of each measurement, absolute differences in terms of charge reading as a measure of the local dose variations would be eliminated. For this, each absolute count value of the measurement downstream of the nonPtNP sample, cnt_{nonPtNP}, is compared with each count value downstream of the PtNP sample, cnt_{PtNP}, by calculating the deviation of the absolute DDCs as follows:

$$DDC_{\text{dev}} = \frac{cnt_{\text{nonPtNP}}}{cnt_{\text{PtNP}}} - 1. \tag{5.5}$$

In this definition, negative DDC_{dev} values suggest a local physical dose increase and positive values a local dose decrease by the PtNP sample. Here, small range differences due to measurement uncertainties or differences in the physical thickness of the samples in the Bragg peak region and also a steep dose decay would result in extremely large absolute values of DDC_{dev}. To avoid these effects and resulting misinterpretations, the analysis is performed only in the plateau region up to the proximal R_{50}, i.e. the WED at which

the count values proximal to the Bragg peak reach 50% of their maximum value. Furthermore, this analysis of absolute DDCs could not be implemented for the eyeline measurements because absolute values are not available, due to normalization to the reference chamber. Basically, the analysis of the Giraffe measurements is sufficient to quantify the influence of possible nuclear interactions.

5.2.6. Uncertainty estimation

The experimental uncertainties for WER_{ratio} (Equation 5.4) are determined with respect to the individual contributions of the thickness ratio H and the WET of the samples. As in Section 4.2.4, they are divided into type A and type B uncertainties.

Sample thickness determination In the CT analysis, the sample thicknesses are determined by five help volumes of varying lateral position, using two PtNP samples and two nonPtNP samples and two contrast windows each. Accordingly, a statistical uncertainty is obtained per contrast window for each sample type based on ten values of its physical thickness and correspondingly for the final thickness ratio from both windowings. For this purpose, the relative deviations are calculated for all thickness values, resulting in an overall relative standard error of $\sigma_{\text{H}} = 0.021$, so 2.1%, for the determination of H.

WET reproducibility and resolution with the Giraffe detector The additional measurements with the Giraffe detector for the WET reproducibility result in a precision of 0.004 mm given by their standard deviation averaged over both energies, 100 MeV and 200 MeV. Experimentally obtained uncertainties on reproducibility are appropriate for reporting uncertainties on the WET, since they also account for fluctuations in the beam energy from the cyclotron. Furthermore, a type B uncertainty of 0.02 mm on the WET resolution was determined.
The quadratic addition of both uncertainties yields 0.02 mm as the uncertainty of the WET measured with the Giraffe detector.

Range reproducibility with the setup at the eyeline For the measurements at the eyeline, no additional measurements are performed to estimate the uncertainties, since measurements of the range are available over a period of several months as part of the commissioning of the eyeline. The reproducibility of the range and thus the uncertainty of the water phantom (e.g. the step sizes due to the motor) as well as of the beam is straightforward. Although these values actually refer to the R_{90} (the range of protons at which the dose dropped to distal 90%), it is assumed that the uncertainty of R_{90} and R_{80} is comparable. A deviation of 0.11 mm is determined by 32 measurements performed

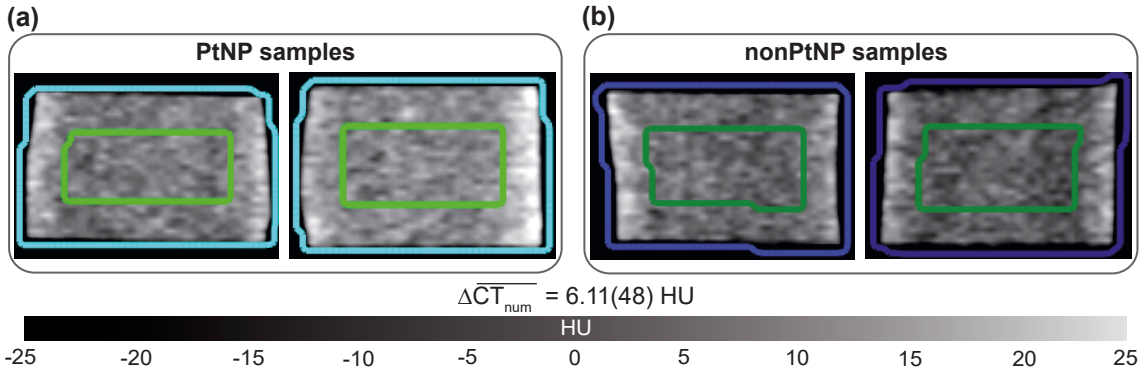

Figure 5.3.: Transversal CT slices of the samples: **(a)** presents the imaging of the PtNP samples and **(b)** the imaging of the nonPtNP samples. Outer contours are marked in light and dark blue and the contours contracted by 5 mm taken for the $\overline{CT_{\text{num}}}$ calculation of the samples are drawn in light and dark green. The HU values of the voxels are expressed in gray scale. The mean CT contrast $\Delta\overline{CT_{\text{num}}}$ of PtNP to nonPtNP samples is provided in concise notation with the standard deviation of the mean. Figure from Behrends et al. (2022).

over several weeks. Like for the WET uncertainties, an experimental determination of the uncertainties regarding the reproducibility of the R_{80} is a reasonable measure, since beam fluctuations are included.

Total WER ratio uncertainty Equation 2.15 and Equation 5.4 yield a total WER_{ratio} standard uncertainty of $\sigma_{WER_{\text{ratio}}} = 0.022$ for the Giraffe setup as well as for the eyeline.

5.3. Results of the PtNP studies

5.3.1. Impact on the treatment planning

Figure 5.3 shows a transversal CT slice of the two PtNP samples and two nonPtNP samples. It is apparent that the PtNP samples appear slightly brighter than the nonPtNP samples. Based on the contracted ROIs, in the mean of both analyzed sample cuboids of each sample type, a mean value $\overline{CT_{\text{num}}}(\text{PtNP}) = 7.46\,\text{HU}$ and its standard uncertainty $\sigma_{\overline{CT_{\text{num}}}}(\text{PtNP}) = 0.35\,\text{HU}$ is obtained for the PtNP sample and $\overline{CT_{\text{num}}}(\text{nonPtNP}) = 1.35\,\text{HU}$ and $\sigma_{\overline{CT_{\text{num}}}}(\text{nonPtNP}) = 0.33\,\text{HU}$ for the nonPtNP sample. On average, an increased contrast $\Delta\overline{CT_{\text{num}}} = 6.11\,\text{HU}$ with its total standard uncertainty of 0.48 HU is found for PtNPs. Based on Equation 5.1, this indicates a larger $\overline{CT_{\text{num}}}$ for the PtNP sample than for the nonPtNP sample, leading to higher HU values with PtNPs. Artifacts are clearly visible at the edges of the samples as very bright voxels outside the contracted ROIs.
The contrast of approximately 6 HU, according to the thickness analysis presented in Section 5.2.2 with the definition of the sample thicknesses at the 50% density level, results

Table 5.1.: Values of the difference in dose coverage ΔD_V of the planning target volume according to Equation 5.3.

patient	$\Delta\rho$ (g/cm³)	$\Delta D_{95\%}$ (%)	$\Delta D_{98\%}$(%)
1	0.005	0.02	0.04
2	0.005	−0.10	0.16
3	0.006	0.0	−0.13

in a difference in CT contrast for the new contouring of approximately 3 HU. So for the new contouring, the sample's outer contour with PtNPs is defined with additional 3 HU in both windowings to ensure the same physical thickness conditions in comparison to the nonPtNP samples. The values of physical thicknesses of both samples and for both CT windowings are provided in Table A.4. On average, the analysis results in a mean value of $H = 0.997(21)$ for the physical thickness ratio.

Any impacts on the dose calculation during treatment planning are assessed using a simple study with three pediatric patients considering the CT contrast. For the simulation of a tumor enriched with PtNPs, the density in the target volume is overwritten corresponding to $\Delta\overline{CT_{\text{num}}}$. The resulting increases in density, as well as the differences in the dose coverage $\Delta D_{95\%}$ and $\Delta D_{98\%}$ (Equation 5.3) of the PTV with overwritten density compared to the original are summarized in Table 5.1. The contrast enhancement leads on average to a density increase assumed by the TPS of $\Delta\rho_{\text{mean}} = 0.005\,\frac{\text{g}}{\text{cm}^3}$. The values for $\Delta D_{95\%}$ and $\Delta D_{98\%}$ take negative and positive values, indicating no clear change for the calculated dose in the presence of the PtNPs in the tumor.

5.3.2. Depth dose analysis and WER comparison

The results of the mono-energetic depth dose measurements with the Giraffe detector at the PBS beam line are presented in the upper part of Figure 5.4. Bragg peaks for different initial proton energies and downstream of the PtNP and nonPtNP samples are shown. The DDCs downstream of two sample cuboids show no noticeable differences between the PtNP and nonPtNP samples with the correction of the sample thickness ratio H. Only the Bragg peaks downstream of four stacked sample cuboids yield a small range shift: Compared to the DDC of the nonPtNP sample, the DDC of the PtNP sample is shifted in proximal direction by about 0.9 mm (see magnification in Figure 5.4). The analysis of the count differences DDC_{dev} (Equation 5.5) for each sampling point is illustrated in the lower part of Figure 5.4. Positive values for DDC_{dev} result for all measurements with two stacked sample cuboids, which may indicate a local dose decrease under the presence of PtNPs. Only the measurements with four stacked cuboids DDC_{dev} result in negative

Table 5.2.: Values of the determined WER_{ratio} given for the measurements at the Giraffe detector for the various mono-energetic energies and the number of stacked samples [Behrends et al. (2022)].

energy (MeV)	100	140	170	200	
number of cuboids	2	2	2	2	4
WER_{ratio}	1.008(22)	1.008(22)	1.008(22)	1.008(22)	0.986(22)

Table 5.3.: Values of the determined WER_{ratio} presented for the measurements at the eyeline for the energy modulated fields [Behrends et al. (2022)].

field configuration	R27M28	R35M35
number of cuboids	1	1
WER_{ratio}	0.999(22)	0.998(22)

values, indicating a local PtNP-induced dose enhancement. However, the deviations of each sampling step up to the proximal R_{50} are in total still within 2%.

The DDCs measured at the eyeline for one PtNP and nonPtNP cuboid are shown in Figure 5.5. Just like almost all Bragg peaks, the energy modulated SOBP distributions show no difference downstream of the PtNP sample compared to the nonPtNP sample.

The resulting WER_{ratio} values (Equation 5.4) for the various field configurations are summarized in Table 5.2 and Table 5.3. In addition, the number of sample cuboids used for the measurements is given, referring to one sample type, i.e. PtNP or nonPtNP, respectively. Regardless of the field configuration with different energies or the number of sample cuboids, all values for WER_{ratio} are consistent to 1 within the uncertainties. Also, the measurements with four stacked cuboids at 200 MeV, which have a shift of 0.9 mm in the range in the DDCs, show a WER_{ratio} consistent to 1 for PtNP and nonPtNP.

5.4. Discussions and conclusion of PtNP-application in proton therapy

In this project, the underlying mechanisms of the radiosensitizing effect of PtNPs under proton irradiation are investigated in the energy domain. For this, tissue-like samples with and without ROS-producing PtNPs with a mean diameter of 40(10) nm and a concentration of 300 $\frac{\mu g}{ml}$ are used. The proton energy deposition is studied and compared downstream of the PtNP and nonPtNP samples.

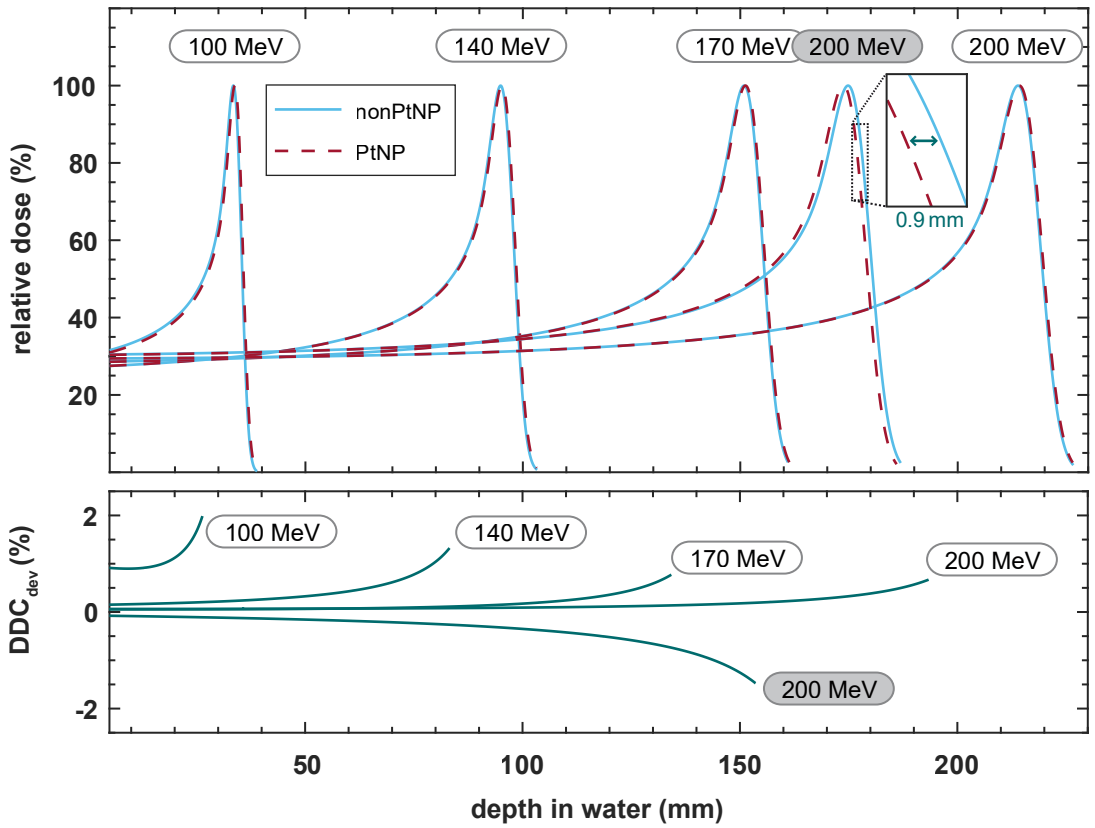

Figure 5.4.: Relative depth dose curves (DDCs) in water for protons with various initial energies downstream of the samples with platinum nanoparticles (PtNP, dashed red) and without PtNP (nonPtNP, light blue) are presented in the top graph. The data is measured with the Giraffe detector for single monoenergetic proton spots. A stack of two cuboid samples is used, except for the gray marked 200 MeV measurement. For that, four cuboids are stacked for each measurement with PtNP samples or nonPtNP samples, respectively. The latter setup is exemplary given in Figure 5.2 (a). These DDCs show a small shift of 0.9 mm downstream of the PtNP samples in comparison to the nonPtNP samples, indicated by the dark green double arrow in the magnified illustration. The deviation of the detector counts DDC_{dev} (Equation 5.5) for each sampling point and each proton energy is given in the bottom graph. Figure adapted from Behrends et al. (2022).

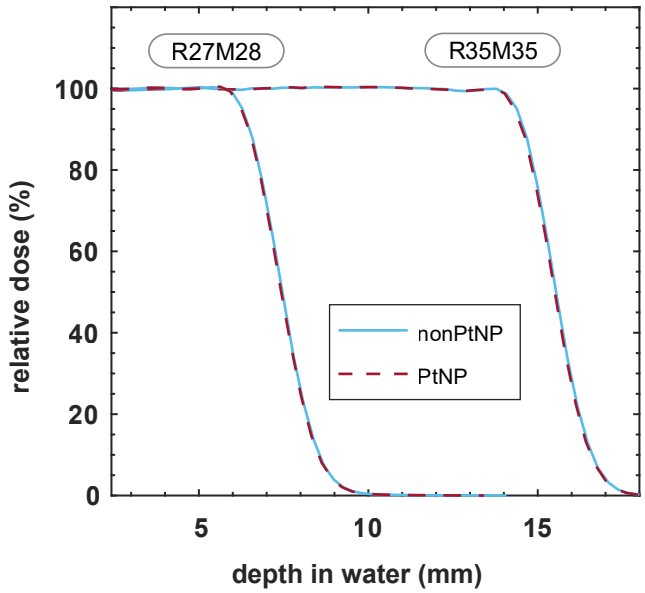

Figure 5.5.: Relative depth dose curves at the eyeline measured in the water phantom with the Advanced Markus chamber for collimated passively scattered proton beams. Curves downstream a PtNP cuboid sample are illustrated in dashed red lines and curves downstream the nonPtNP sample in light blue lines. Figure from Behrends et al. (2022).

Impact on the treatment planning

The investigation of the sample parameters by CT imaging is performed based on two randomly selected PtNP and two nonPtNP sample cuboids. Thus, both the determined CT contrast and the thickness ratio refer to random samples, but are assumed to be valid for all sample cuboids. For the CT contrast determination and the resulting influence on the treatment planning, this means that deviations can occur if the sample cuboids differ from each other. Since the standard errors determined in Section 5.3.1 are relatively small and thus the samples are quite homogeneous, the influence is thus assumed to be unlikely. Clinical imaging with x-rays can be affected by high absorption coefficients, such as those of gold or platinum. Here, CT analysis demonstrates an increased CT contrast $\Delta\overline{CT_{\mathrm{num}}}$ of $6.11(48)$ HU on average in the presence of PtNPs, which therefore makes these PtNPs interesting for clinical imaging. In the previous studies of Hainfeld et al. (2013), Silvestri et al. (2016) and Han et al. (2019) presenting AuNPs as non-toxic contrast agents in CT imaging, higher concentrations than the one used here were chosen. At the same concentration, a CT attenuation of 8 HU, which is comparable to the CT contrast of the PtNPs found here, was observed with gadolinium [Kim et al. (2018)].

The fact that an enhanced CT contrast is obtained with these PtNPs may indicate a relevant clinical effect on the treatment planning. A recalculation of the previously highly conformal dose coverage in the target volume of three pediatric brain tumor patients based on

the CT contrast of 6 HU, which corresponds to just a mean density increase of 0.005 $\frac{g}{cm^3}$, does not show any influence on the calculated dose. The fact that the dose statistics for $D_{95\%}$ and $D_{98\%}$ deviate in positive and negative directions can be explained by variations due to the voxel grid.

However, the conversion from HU to density is made using the clinical CT calibration curve. This correlation is based on clinically relevant materials, such as tissue, water, fat, calcium, and will therefore not be valid for metals like platinum. It is reasonable to assume that a calibration curve for platinum would result in a stronger increasing HU value with increasing density due to the higher photoelectric effect and thus higher attenuation coefficients. This would lead to a smaller increase in density $\Delta\rho$ for the same CT contrast $\Delta\overline{CT_{\text{num}}}$. Therefore, the effect of PtNPs tends to be overestimated in this study, which further indicates a negligible clinical effect in the treatment planning. Moreover, it points out that PtNPs do not necessarily need to be delivered already for a planning CT. It would be sufficient to inject them for the proton irradiation.

In this study, a CT tube voltage of 80 kV is used. Although smaller photon energies generally have a higher absorption coefficient, Galper et al. (2012) have shown that an optimal contrast of AuNP in water is achieved with 120 kV, due to a higher number of photons near the K-edge at 80.7 keV. However, this is also related to beam hardening, i.e. the increase in x-ray energy when the photons penetrate several centimeters of water until reaching the contrast agents, which favors attenuation with AuNPs in water from 80 kV to 120 kV. Platinum has similar absorption coefficients and a K-edge at 78.4 keV compared to gold [Berger et al. (2010b)], which is why the contrast's behavior of Pt used here is assumed to be similar to Au. The samples with PtNPs embedded in gelatin are scanned in air instead of a water phantom. In addition, Galper et al. (2012) have presented that a tube voltage of 80 kV reveals the best contrast for AuNP samples in air.

All these observations demonstrate that the choice of the CT voltage for metal nanoparticle scans is not straightforward. The extent to which the CT voltage of 80 kV used here is optimal for the PtNP and nonPtNP samples in air remains unclear. Nevertheless, a CT scan of the PtNP and nonPtNP samples in a water phantom at 120 kV would have been preferable in terms of comparable physiological conditions for the investigations in clinical patients.

Depth dose distributions and energy deposition

The results of the WER_{ratio} values (Table 5.2 and 5.3) show no difference in the WER of the individual samples (Equation 2.15), indicating no difference in the stopping power of the samples. This reveals no increased energy deposition, and thus absorbed dose, at

the macroscopic scale, when PtNPs are present. Even with the small difference in the detected DDCs at 200 MeV (Figure 5.4) and four stacked samples, the measurements yield an unchanged WER of the samples within the uncertainties. This does not indicate a different energy deposition, although one might suspect this when considering Figure 5.4.
Only the measurements with 200 MeV and four stacked samples show negative values for the deviation of their absolute detector counts DDC_{dev}, which by definition could indicate a local dose increase (lower part of Figure 5.4). However, this deviation is still within a 2% interval until a depth of the proximal 50% of the Bragg peak. The peak region is not evaluated because the absolute count deviations would be unrealistically large due to small range differences (see upper part of Figure 5.4) and may lead to a misleading interpretation. To investigate an effect of local energy deposition based on point-wise deviations in the depth dose curve, matching could have been performed on the R_{80} of the DDC of the nonPtNP and PtNP sample. This method is not applied here because it would falsify the original purpose of the study. Since all other measurements result in positive deviations of the absolute count values DDC_{dev} and there are no deviations larger than 2% in the region proximal 50% of the Bragg peak, these results show a comparable total energy deposition of the protons downstream of the PtNP and nonPtNP samples. This means that the nuclear interactions do not contribute relevantly to the energy deposition in the presence of PtNPs, which otherwise could have been a possible explanation for the radiosensitizing effect.
Gold nanofilms with higher concentrations such as 5.5 $\frac{\text{mg}}{\text{ml}}$ and 6.1 $\frac{\text{mg}}{\text{ml}}$ were studied in Ahmad et al. (2016) and revealed macroscopic effects in the shape and longitudinal shifts of the Bragg peak in the simulations and experiments. These results remain unconfirmed in this work. Such differences may indicate that nanofilms cause different effects than NPs and thus are not comparable.
Dose enhancement due to the radiosensitizing effect of metal NPs has been demonstrated in other works very localized in the immediate vicinity of the NPs [Sicard-Roselli et al. (2014); Wälzlein et al. (2014); Cho et al. (2016)]. In the present work, the energy deposition is measured and investigated macroscopically downstream of the samples, which is why a potential local microscopic dose increase cannot be detected here.
While the measurements of the DDCs with the Giraffe detector are performed with the samples placed in the beam's entrance plateau, during the measurements at the eyeline the samples are positioned in the spread-out Bragg peak. Thus, the samples are located in different Bragg peak regions for the two setups. The fact that the depth dose distributions and the results on the WER_{ratio} in both setups show no difference between PtNP and nonPtNP samples excludes effects on the macroscopic scale. Effects on the microscopic scale due to the variable proton LET with increasing proton penetration depth, as

observed in Li et al. (2016) for AuNPs, should be investigated in further studies.
The fact that the thickness ratio is determined on the basis of random sampling and assumed to be valid for all sample cuboids on average could also lead to discrepancies in the samples' WER, especially when more than two samples are used for the measurements.
Furthermore, the similar ranges and energy depositions between the PtNP and nonPtNP samples, as observed in the WER, confirm a negligible dosimetric impact by PtNPs in the treatment planning study.

Further considerations on the radiosensitizing effect of PtNPs

This work demonstrates studies of the radiosensitizing effect from a physical perspective, which is why a large amount of material leading to a high electron density (Equation 2.6) is of interest. For this purpose, colloidal NPs with a mass concentration of 300 $\frac{\mu g}{ml}$ and an average PtNP diameter of $40(10)$ nm are chosen and placed in the beam path. Compared to Zwiehoff et al. (2021), these PtNPs have a relatively high concentration and large diameter. In this way, an increase by the factor 2 in the amount of damaging radicals is obtained when interacting with protons compared to samples without PtNPs (Figure A.2). This study does not consider biological issues such as cellular uptake, toxicity or sterilization, as investigated in Johny et al. (2022b), of the metal NPs. At this point, it is important to achieve a potentially high enhancement effect in proton therapy and not to initially implement a clinical application of the PtNPs.
The chemotherapy uses the anti-cancer drug cisplatin to inhibit cell growth, which contains a large amount of platinum. The work of Zeng et al. (2020) suggests an *in vivo* PtNP generation by cisplatin, as PtNPs were found in the blood of treated patients. Based on the results of the present project, the question arises, whether a potential radiosensitizing effect of *in vivo* generated PtNPs may be exploited indirectly. Determined *in vivo* generated PtNP concentrations in the blood of maximally about 0.09 $\frac{\mu g}{ml}$ contradict this, since the concentrations are about a factor 100 smaller than the one used in Zwiehoff et al. (2021) and even a factor 3000 smaller than the one used here. Therefore, it is assumed that the amount of *in vivo* generated PtNPs is too small for a potential radiosensitizing effect. Furthermore, a biologically induced protein corona forms around the *in vivo* generated PtNPs, which could additionally mitigate the ROS generation [Zeng et al. (2020)].
These experiments demonstrate that the radiosensitizing effect of PtNPs in proton therapy is not due to an increased macroscopic energy deposition of the protons. Behrends et al. (2022) present further measurements with a pixelated semiconductor detector that also reveal equivalent energy deposition in the silicon sensor downstream of the nonPtNP and PtNP sample by measuring the absolute deposited charge. Furthermore, the spot sizes in the two-dimensional pixel sensor match within their uncertainties downstream of the

nonPtNP and PtNP samples, indicating no effect due to potential increased MCS of protons by the PtNPs present.
The fact that an increased energy deposition of protons is not responsible for the enhanced proton therapy efficiency confirms the arguments of Dollinger (2011). Therein, it was discussed that only a small fraction of the proton energy can be transferred to the PtNPs themselves. Overall, the basic mechanisms of the radiosensitizing effect of PtNPs in proton therapy cannot be explained in this work and remain an unsolved issue. However, this topic does not confirm a mass-dependent effect, as this would presumably induce an increased energy deposition due to the increased electron density of the PtNP sample. These results rather suggest a confirmation of the reported surface effect and thus also indicate a catalytic effect of the PtNPs as previously observed in Zwiehoff et al. (2021).

Conclusions

This project serves as experimental proof that an enhanced stopping power or energy deposition in the presence of ROS-producing PtNPs is not the determining factor for the radiosensitizing effect of the PtNPs in proton irradiation at the macroscopic scale. Studies of the proton stopping power in the presence of $40(10)\,\mathrm{nm}$ sized PtNPs with a concentration of $300\,\frac{\mu g}{ml}$ are conducted. Comparable WERs of the samples with and without PtNPs are detected within the experimental uncertainties of 2% on a macroscopic scale. Analyses of the impact on clinical treatment planning in imaging and dose calculation reveal the potential use of the PtNPs as contrast agents, but no effect on the dose calculation. The latter confirms the result of the unchanged energy deposition with PtNPs. The results further indicate that the PtNPs are not required for the planning CT and it is sufficient to inject the NPs for treatment. Moreover, radiation planning would be straightforward with no additional dose correction for a tumor enriched with these ROS-generating PtNPs.
In summary, the experiments in this project confirm theories of the underlying mechanisms of the radiosensitizing effect of PtNPs in proton therapy previously suspected in the literature. The results serve as further evidence for chemical aspects, such as the catalytic effect of PtNPs. Nevertheless, no microscopic studies are performed and the experiments cannot provide a complete clarification of the underlying aspects of the enhancement effect. However, this project provides a contribution to an exciting, highly interesting but not yet fully understood research field of radiation chemistry and biology.

6. Summary and conclusion

In this work, various physical aspects for optimizing radiobiological research in proton therapy are extensively investigated. Three independent approaches to extend the therapeutic window by either increased sparing of normal tissue or a more effective application of proton radiation are presented. Owing to the extremely small scales involved in these research projects, high accuracy is required, making them particularly challenging.

The pencil beam scanning technique offers many optimization aspects for the treatment planning in proton therapy. A combination with static or dynamic apertures provides new field shaping options. The Project *milli* in Chapter 3 examines the fundamental relationship between a spot and the aperture edge in terms of a lateral field penumbra reduction. Detailed analytical evidence based on one-dimensional considerations for shaping the intensity profile of a single spot that is cut at an aperture edge is presented. These analytical approaches demonstrate that the placement of the spot beyond the aperture edge is advantageous in terms of a sharper dose gradient. This presented method of overscanning exploits the stronger influence of the relative gradient of the aperture. Profile measurements and simulations of the spot in air on a clinical brass aperture for multiple spot positions relative to the edge on a pencil beam scanning beam line confirm this effect. A reduction of up to 20% in the LP at a spot overscanning of 5 mm can be achieved. In absolute terms, a lateral penumbra of the order of one *milli*meter is reached. Investigations under more clinical conditions with a range shifter or in extended fields in water demonstrate that the effect is also pronounced at lower depths and higher energies. The combination of a spot optimization and fluence modulation is proved to be an effective option for field shaping in collimated scanned proton fields. Furthermore, the very interesting results provoke further investigations in terms of clinical relevance. With regard to clinically realistic field configurations, the influence of spot spacing or variable spot weighting is of particular interest. Dynamic collimator systems open up attractive opportunities especially for depth modulated fields due to their continuous optimization possibilities.

Overall, this project presents new possibilities for a spot position optimization in collimated scanned proton fields, achieving a reduced lateral penumbra. With this method,

normal tissue and organs at risk lateral to the beam direction can be better protected.

In order to further investigate the effects of ionizing radiation on radiobiology, adequate experimental conditions for cell experiments are needed. Since the LET of protons increases sharply at the distal end of the Bragg peak and thus may induce adverse side effects, it is of particular interest for the research in proton therapy. A comparison between protons and carbon ions or laser accelerated protons, which are interesting due to their high dose rate and a potential FLASH effect, could also provide further insight into the radiation effects. Radiobiological research at this level requires low-energy protons, with high LET. For this reason, an experimental setup for providing radiobiologically relevant energies, especially down to the few-MeV level, is developed and optimized in the Project *micro*. In this context, the delivery of low-energetic protons is particularly challenging due to their short range, which means according to the studies with laser accelerated protons in the *micro*meter range. To reduce the energy of clinical protons for this purpose, absorbing materials are used. It is shown that the limiting physical factors such as increasing range straggling and reduction of the fluence with increasing material thickness lead to an optimal setup for a maximal efficiency. With such an optimized setup, especially for the provision of proton energies in the few-MeV range, radiobiological experiments can be performed with a maximal efficiency for all relevant energies as well as under uniform environmental conditions. However, this project does not investigate all aspects related to this method. Secondary effects affecting the dose like the higher neutron production by the absorbing material in the beam path should be considered.
In general, there are various potential applications for radiobiological research in a clinical facility where this optimized setup can be useful. Research under these extreme conditions could provide further insights into radiation effects.

In addition to the reduction of the normal tissue complications, the therapeutic window can also be extended via an optimized tumor control. Due to their radiosensitizing effect, metal nanoparticles can locally enhance radiation efficacy. Such a therapy enhancement effect in a nanoparticle-enriched tumor can thus increase the tumor control. While there are many promising results regarding the potential application of metal nanoparticles in proton therapy, the underlying mechanism of enhanced therapy efficacy is not conclusive [Schuemann et al. (2020)]. The Project *nano* in Chapter 5 studies in detail the potential for an increased proton energy deposition in the presence of platinum *nano*particles. For this purpose, the water equivalent ratio downstream of a tissue-like sample with and without PtNPs is experimentally determined and compared. Here, the PtNPs have a diameter of $40(10)\,\mathrm{nm}$ and a concentration of $300\,\frac{\mu g}{ml}$. On the macroscopic scale, the WER is found

to be the same within the uncertainties of 2%, suggesting unchanged energy deposition and stopping power in the presence of PtNPs. This indicates that the radiosensitizing effect of PtNPs is not due to an increased energy deposition, but rather to a catalytic effect due to radical reactions. Since the underlying effect remains unexplained, further studies should investigate in detail potential mechanisms of the radiosensitizing effect on a chemical basis, in addition to previous promising ROS studies.
Furthermore, the project addresses the treatment planning process with PtNPs. Investigations in a CT reveal that a contrast of about 6 HU can be achieved. This supports the potential use of metal nanoparticles as contrast agents in imaging. However, the contrast enhancement and associated density change does not affect treatment planning, as the dose calculation is straightforward. More studies with a varying CT voltage and PtNP concentrations could provide further insight into the contrast potential of PtNPs.
Overall, this project provides a contribution to previously unsolved and highly debated radiobiological research topics. Furthermore, a clinical treatment planning with these PtNPs is found to remain unaffected.

All together, this work presents three independent research approaches, each with its own contribution to improving the therapeutic effect of proton therapy.

List of abbreviations

AuNP	Gold nanoparticle
CT	Computer tomography
DDC	Depth dose curve
DNA	Deoxyribonucleic acid
FBTR	Fixed beam treatment room
FWHM	Full width at half maximum
HU	Hounsfield unit
IC	Ionization chamber
IMPT	Intensity modulated proton therapy
LAP	Laser accelerated proton
LET	Linear energy transfer
LETd	Dose-averaged linear energy transfer
LP	Lateral penumbra
MCS	Multiple Coulomb scattering
MLIC	Multi-layer ionization chamber
NIST	National Institute of Standards and Technology
NP	Nanoparticle
NTCP	Normal tissue complication probability
OS	Overscanning
PBS	Pencil beam scanning

PET	Positron emission tomography
PIXE	Particle-induced x-ray emission
PMMA	Polymethyl methacrylate
PtNP	Platinum nanoparticle
PTV	Planning target volume
RBE	Relative biological effectiveness
rf	Radio frequency
ROI	Region of interest
ROS	Reactive oxygen species
RS	Range shifter
SFUD	Single field uniform dose
SOBP	Spread-out Bragg peak
TCP	Tumor controll probability
TOPAS	Tool for particle simulation
TPS	Treatment planning system
WED	Water-equivalent depth
WER	Water-equivalent ratio
WET	Water-equivalent thickness
WPE	West German Proton Therapy Centre Essen

A. Appendix

Project *micro*

This section provides additional material to the measurements of the DDCs and the simulations of the energy spectra.

Details of DDC measurements

Table A.1.: Thickness details and measurements of the uniformity of the used RW3-plates.

label of plate	nominal thickness (mm)	meas. thickness (mm)	max. deviation (mm)
101	10	10.052	0.016
102	10	10.011	0.038
51	5	5.059	0.054
21	2	2.051	0.132
22	2	1.995	0.011
11	1	1.007	0.015

Table A.2.: Details of the DDC measurements with the extrapolation chamber: The absorber combinations with their resulting WED and the measured charge values. The total WED includes the WET of the aluminum range shifter (RS).

measure-ment	absorber (+ aluminum RS and Kapton layer)			mean charge (nC)	std. dev. of charge (nC)	total WED (mm)	std. dev. of total WED (mm)
	RW3-plates		Mylar foils (µm)				
	nominal thickness (mm)	labels of used plates					
1	23	*101 + 102 + 21 + 11*	-	12.70	0.072	105.393	0.10
2	23	*101 + 102 + 21 + 11*	500	13.23	0.045	106.057	0.10
3	24	*101 + 102 + 21 + 22*	-	13.20	0.075	106.409	0.10
4	24	*101 + 102 + 21 + 22*	400	12.46	0.028	106.941	0.10
5	25	*101 + 102 + 51*	-	11.19	0.069	107.451	0.06
6	25	*101 + 102 + 51*	200	10.23	0.033	107.717	0.06
7	26	*101 + 102 + 51 + 11*	-	7.373	0.067	108.486	0.07

Details of the energy spectra simulations

Table A.3.: Total water equivalent depth due to the absorber made of an aluminum range shifter, a Kapton layer and the listed RW3-plates.

simulation	RW3-plates in absorber combination		total WED (mm)
	nominal thickness (mm)	labels of used plates	
1	20	*101 + 102*	102.232
2	21	*101 + 102 + 11*	103.268
3	22	*101 + 102 + 21 + 22*	104.341
4	23	*101 + 102 + 21* + 11	105.377
5	24	*101 + 102 + 21 + 22*	106.393
6	25	*101 + 102 + 51*	107.435
7	26	*101 + 102 + 51 + 11*	108.470
8	27	*101 + 102 + 51 + 21*	109.543

Project *nano*

For the project, further methods and results are applied or achieved in cooperation with other groups, which are given here for the sake of completeness. For further details refer to Behrends et al. (2022).

First, the manufacturing process of the PtNPs is shown. In addition, details are given on the determination of the ratio of the physical thicknesses of the samples in the CT. The methods and results of the additional measurements of energy deposition and spot size with the pixel detector are also provided.

Manufacturing process and ROS verification of PtNPs

The fabrication of the tissue-like samples with and without surfactant-free PtNPs requires a few steps, which are schematically illustrated in Figure A.1. This includes the process of laser ablation in liquids, centrifugation of the PtNPs with size determination, and a gelation process. The manufacturing process was carried out by the Center for Nanointegration (CENIDE) from the University of Duisburg-Essen.

To ensure that the manufactured PtNPs generate ROS upon proton irradiation, the manufactured PtNPs (after step centrifugation, Figure A.1 (b)) are placed in water phantoms

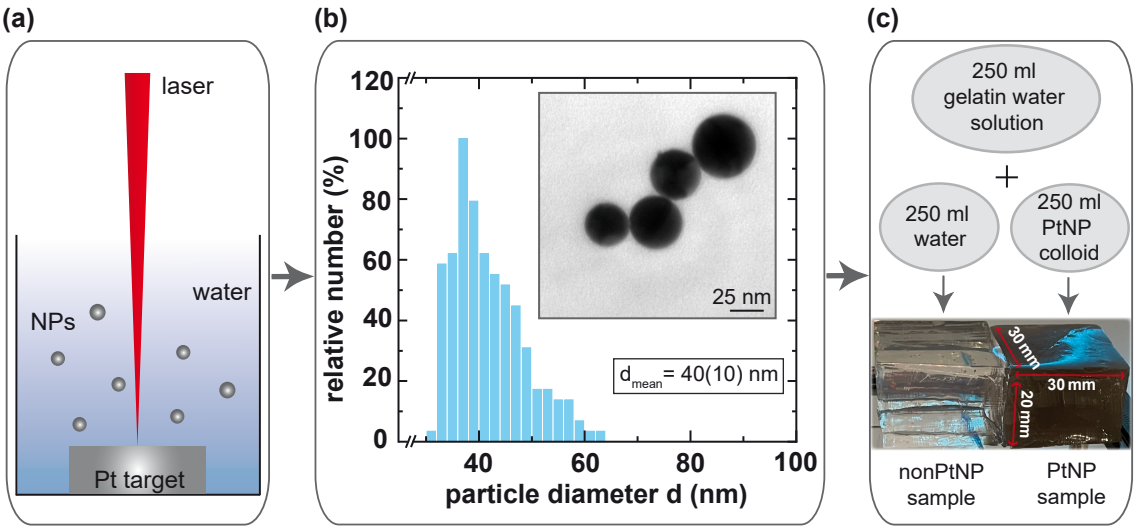

Figure A.1.: Scheme of the sample production workflow: **(a)** presents the process of pulsed laser ablation in liquids for NP synthesis. In **(b)**, the nanoparticles size distribution after centrifugation with the mean particle diameter of 1000 analyzed platinum nanoparticles (PtNPs) yielding $d_{\text{mean}} = 40(10)$ nm is given. In addition, a transmission electron micrograph of four PtNPs is provided. A scheme of the gelation process and a picture of the final samples is shown in **(c)**. Figure based on Behrends et al. (2022).

with different concentrations. In addition, samples without PtNPs are used as reference. A mono-energetic homogeneous proton field (100 MeV) with external dimensions of $10 \times 15\,\text{cm}^2$ covering the well plate with lateral uncertainties and an absorbed dose of 5 Gy in the entrance plateau is used to irradiate the samples. As an ROS dye, terephthalic acid (TA) was added to the samples in the well plate before irradiation to subsequently determine the number of ROS via a fluorescence signal. In general, the experiment was performed like the measurements in Zwiehoff et al. (2021). The effect of increasing PtNP concentration on generated 2-OH-TA is given in Figure A.2. Compared to the 2-OH-TA level, each concentration of PtNPs used shows an increased number of 2-OH-TA. Furthermore, the higher the concentration of PtNPs in the colloid, the higher is the 2-OH-TA production. The presence of PtNPs with the highest concentration of 300 $\frac{\mu g}{ml}$ achieves an ROS(2-OH-TA) production increase by about a factor of 2 compared to the PtNP-free reference.

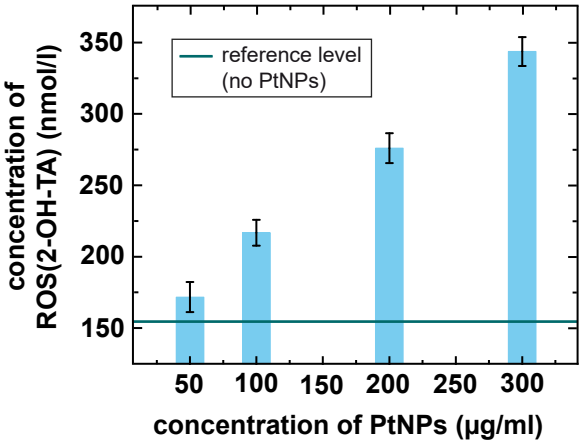

Figure A.2.: Produced 2-OH-TA concentration in the presence of the ROS dye terephthalic acid (TA) during proton irradiations of PtNPs with an absorbed dose of 5 Gy. 2-OH-TA is a measure of ROS, because during proton irradiation the hydroxyl radicals react with TA forming 2-OH-TA. The number of generated radicals increases with the PtNP concentration, with the horizontal line showing the 2-OH-TA level for irradiation without PtNPs. The error bars indicate the standard uncertainty on the nine independent samples for each concentration. Figure from Behrends et al. (2022).

Results of the CT analysis of the PtNP samples

Table A.4 gives the results of the thickness analysis of the samples in the CT images. From both CT windows, it follows a mean ratio of physical thicknesses $H = 0.997(21)$.

Table A.4.: Values of the physical thicknesses of the sample from the CT analysis to calculate H.

CT window	sample	single measurements (cm)					mean h (cm)	H
brain	PtNP1	1.84	1.76	1.76	1.76	1.80	1.828	0.996
	PtNP2	1.88	1.88	1.88	1.88	1.84		
	nonPtNP1	1.80	1.84	1.76	1.84	1.84	1.836	
	nonPtNP2	1.88	1.88	1.84	1.84	1.84		
lung	PtNP1	2.08	2.04	2.04	2.04	2.04	2.088	0.998
	PtNP2	2.16	2.12	2.16	2.12	2.08		
	nonPtNP1	2.08	2.08	2.00	2.08	2.08	2.092	
	nonPtNP2	2.16	2.16	2.08	2.08	2.12		

Measurements of the energy deposition downstream of the PtNPs with a pixelated semiconductor detector

A pixelated semiconductor detector as described in Schilling et al. (2022a,b) is used for the additional measurements of energy deposition and spot size downstream of the PtNP and nonPtNP samples.

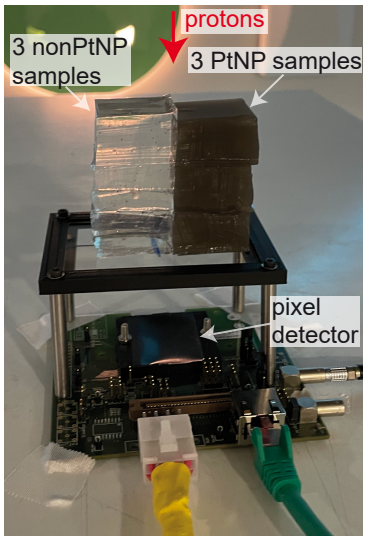

Figure A.3.: Setup including the semiconductor pixel detector for measurements of the deposited charge downstream of PtNP and nonPtNP samples. More details on the measurements as well as the adopted figure can be found in Behrends et al. (2022).

Data interpretation

The energy dependent ratio $E_{\mathrm{dep,ratio}}(E_0)$ with the initial proton energy E_0 is calculated to compare the energy deposition downstream of the PtNP and nonPtNP samples:

$$E_{\mathrm{dep,ratio}}(E_0) = \frac{\overline{E_{\mathrm{dep,nonPtNP}}}(E_0)}{\overline{E_{\mathrm{dep,PtNP}}}(E_0)}. \tag{A.1}$$

This would result in a value less than 1, when the protons deposit more energy in the PtNP sample, assuming that they have the same thickness.
The ratio of the mean spot sizes $\sigma_{\mathrm{spot,ratio}}(E_0)$ is calculated to investigate potential scattering effects of the protons at the PtNPs:

$$\sigma_{\mathrm{spot,ratio}}(E_0) = \frac{\overline{\sigma_{\mathrm{spot,nonPtNP}}}(E_0)}{\overline{\sigma_{\mathrm{spot,PtNP}}}(E_0)}. \tag{A.2}$$

Here, an increased proton scattering with PtNPs would result in a value less than 1.

Results of the energy deposition and spot size

In the following, the results of the pixel detector measurements are presented. Figure A.4 shows the distributions of the energy depositions in the sensor downstream of the PtNP and nonPtNP sample. The mean deposited energy, indicated by the dashed lines, is comparable considering the experimental uncertainty of 1.09% [Behrends et al. (2022)].

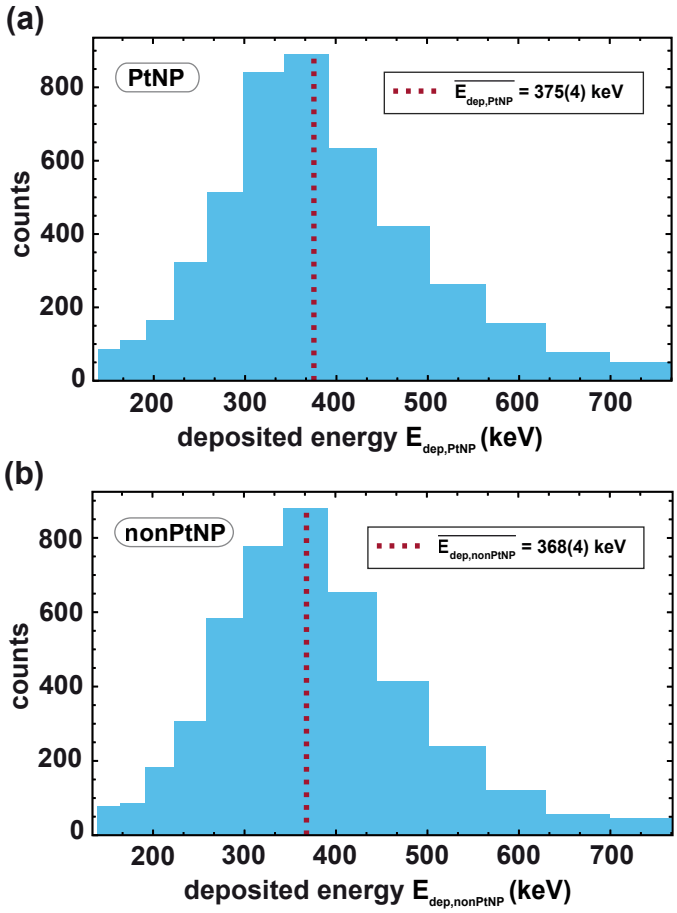

Figure A.4.: Distribution of the deposited energy in the pixel detector downstream of one PtNP (in **(a)**) and one nonPtNP sample (in **(b)**). The protons have an initial energy of 120 MeV and traversed an additional 56.2 mm water equivalent buildup. Figure based on Behrends et al. (2022).

Table A.5 provides the mean deposited energies downstream the various samples for all evaluated measurements. The ratio of the deposited energy downstream the nonPtNP sample and PtNP sample is given with its standard deviation derived from the experimental uncertainty of 1.09%. In addition, a second uncertainty analysis including the different sample thicknesses is written as the upper and lower limit of the $\pm 1\sigma$ confidence interval. Further, the spot sizes downstream of the samples evaluated on the two-dimensional array of the sensor are provided with their uncertainties.

Considering the uncertainties, it can be seen that the deposited energy and the spot size downstream of the PtNP and nonPtNP sample are comparable with one exception in each

case. This means that on a macroscopic scale, the protons do not deposit more energy in the presence of the PtNPs and there is also no increased lateral proton scattering by PtNPs. All details are in Behrends et al. (2022).

Table A.5.: Values of the ratio of the mean deposited energy and spot sizes during the pixel detector measurements. From Behrends et al. (2022).

energy (MeV)	setup	$\overline{E_{\text{dep,sample}}}$ (keV)		$E_{\text{dep,ratio}}$	$\sigma_{\text{spot,ratio}}$
		PtNP	nonPtNP		
100	3 samples stacked	510(6)	521(6)	$1.022(16)^{+0.036}_{-0.028}$	1.14(14)
		508(6)	520(6)	$1.024(16)^{+0.036}_{-0.028}$	1.02(10)
110	1 sample + absorber	556(6)	552(6)	$0.993(16)^{+0.013}_{-0.011}$	0.95(11)
		558(6)	555(6)	$0.995(16)^{+0.013}_{-0.011}$	1.13(11)
120	1 sample + absorber	377(5)	367(4)	$0.973(15)^{+0.007}_{-0.005}$	1.03(8)
		375(4)	368(4)	$0.981(16)^{+0.007}_{-0.005}$	0.96(5)
	4 samples stacked	382(5)	392(5)	$1.026(16)^{+0.029}_{-0.023}$	1.00(8)

Bibliography

Adrian, G., Konradsson, E., Lempart, M. et al., 2020. The FLASH effect depends on oxygen concentration. The British Journal of Radiology **93** (1106), 20190702. 55

Agostinelli, S., Allison, J., Amako, K. et al., 2003. Geant4—a simulation toolkit. Nuclear Instruments and Methods in Physics Research Section A: Accelerators, Spectrometers, Detectors and Associated Equipment **506** (3), 250–303. 25

Ahmad, R., Royle, G., Lourenço, A. et al., 2016. Investigation into the effects of high-Z nano materials in proton therapy. Physics in Medicine and Biology **61** (12), 4537–4550. 95

Al-Hallaq, H., Cao, M., Kruse, J. et al., 2019. Cured in a FLASH: Reducing Normal Tissue Toxicities Using Ultra-High-Dose Rates. International Journal of Radiation Oncology Biology Physics **104** (2), 257–260. 55

Attix, F.H., 2004. Introduction to radiobiological physics and radiation dosimetry. WILEY-VCH Verlag GmbH Co. KGaA. 5, 8

Bambynek, W., Crasemann, B., Fink, R.W. et al., 1972. X-Ray Fluorescence Yields, Auger, and Coster-Kronig Transition Probabilities. Reviews of Modern Physics **44** (4), 716–813. 78

Baumann, M. and Grégoire, V., 2009. Modified fractionation. In: Joiner, M.C. and van der Kogel, A. (Eds.), Basic Clinical Radiobiology. Hodder Arnold. 1, 2

Bäumer, C. and Farr, J.B., 2011. Lateral dose profile characterization in scanning particle therapy. Medical Physics **38** (6), 2904–2913. 34

Bäumer, C., Fuentes, C., Janson, M. et al., 2019. Stereotactical fields applied in proton spot scanning mode with range shifter and collimating aperture. Physics in Medicine and Biology **64** (15), 155003. 15, 28, 48, 49

Bäumer, C., Janson, M., Timmermann, B. et al., 2018. Collimated proton pencil-beam scanning for superficial targets: impact of the order of range shifter and aperture. Physics in Medicine and Biology **63** (8), 085020. 27, 28, 49

Bäumer, C., Koska, B., Lambert, J. et al., 2015. Evaluation of detectors for acquisition of pristine depth-dose curves in pencil beam scanning. Journal of Applied Clinical Medical Physics **16** (6), 151–163. 59

Bäumer, C., Plaude, S., Khalil, D.A. et al., 2021. Clinical Implementation of Proton Therapy Using Pencil-Beam Scanning Delivery Combined With Static Apertures. Frontiers in Oncology **11**, 599018. 14, 15, 28, 38, 49

Behrends, C., Bäcker, C.M., Schilling, I. et al., 2022. The radiosensitizing effect of platinum nanoparticles in proton irradiations is not caused by an enhanced proton energy deposition at the macroscopic scale. Physics in Medicine and Biology **67** (15), 155023. 59, 76, 80, 82, 83, 84, 89, 91, 92, 93, 96, 107, 108, 109, 110, 111, 112

Behrends, C., Bäumer, C., Verbeek, N. et al., 2021. Technical note: Providing proton fields down to the few-MeV level at clinical pencil beam scanning facilities for radiobiological experiments. Medical Physics **49** (1), 666–674. 12, 54, 58, 59, 65, 67, 68

Behrends, C., Bäumer, C., Verbeek, N. et al., 2023. Optimization of proton pencil beam positioning in collimated fields. Medical Physics *accepted and online available*. 28, 31, 34, 36, 40, 41, 42, 44, 46

Bentzen, S.M., 2009. Dose-response relationships in radiotherapy. In: Joiner, M.C. and van der Kogel, A. (Eds.), Basic Clinical Radiobiology. Hodder Arnold. 1

Berger, M., Coursey, J., Zucker, M. et al., 2010a. ESTAR, PSTAR, and ASTAR: Computer Programs for Calculating Stopping-Power and Range Tables for Electrons, Protons, and Helium Ions (version 1.2.3). National Institute of Standards and Technology, Gaithersburg, MD, [Online] Available: http://physics.nist.gov/Star [2022]. 53, 59, 62, 64, 71, 85

Berger, M.J., Hubbell, J.H., Seltzer, S.M. et al., 2010b. XCOM: Photon Cross Section Database (version 1.5). National Institute of Standards and Technology, Gaithersburg, MD, [Online] Available: http://physics.nist.gov/xcom [2022]. 94

Bethe, H., 1930. Zur Theorie des Durchgangs schneller Korpuskularstrahlen durch Materie. Annalen der Physik **397** (3), 325–400. 8

Beyreuther, E., Brüchner, K., Krause, M. et al., 2017. An optimized small animal tumour model for experimentation with low energy protons. PLOS ONE **12** (5). 53

Bichsel, H. and Hiraoka, T., 1989. Energy Spectra and Depth-Dose Curves for 70 MeV Protons. International Journal of Quantum Chemistry: Quantum Chemistry Symposium **23**, 565–574. 13, 69

Bloch, F., 1933. Zur Bremsung rasch bewegter Teilchen beim Durchgang durch Materie. Annalen der Physik **408** (3), 285–320. 8

Bohr, N., 1915. On the decrease of velocity of swiftly moving electrified particles in passing through matter. The London, Edinburgh, and Dublin Philosophical Magazine and Journal of Science **30** (178), 581–612. 12

Bortfeld, T., 1997. An analytical approximation of the Bragg curve for therapeutic proton beams. Medical Physics **24** (12), 2024–2033. 37, 59, 62, 85, 86

Bues, M., Newhauser, W.D., Titt, U. et al., 2005. Therapeutic step and shoot proton beam spot-scanning with a multi-leaf collimator: a Monte Carlo study. Radiation Protection Dosimetry **115** (1-4), 164–169. 15, 28, 49

Butterworth, K.T., McMahon, S.J., Currell, F.J. et al., 2012. Physical basis and biological mechanisms of gold nanoparticle radiosensitization. Nanoscale **4** (16), 4830. 77

Cerchez, M., Prasad, R., Aurand, B. et al., 2019. ARCTURUS laser: a versatile high-contrast, high-power multi-beam laser system. High Power Laser Science and Engineering **7**, E37. 55

Chaudhary, P., Marshall, T.I., Perozziello, F.M. et al., 2014. Relative Biological Effectiveness Variation Along Monoenergetic and Modulated Bragg Peaks of a 62-MeV Therapeutic Proton Beam: A Preclinical Assessment. International Journal of Radiation Oncology Biology Physics **90** (1), 27–35. 54

Cho, J., Gonzalez-Lepera, C., Manohar, N. et al., 2016. Quantitative investigation of physical factors contributing to gold nanoparticle-mediated proton dose enhancement. Physics in Medicine and Biology **61** (6), 2562–2581. 78, 95

Ciocca, M., Magro, G., Mastella, E. et al., 2019. Design and commissioning of the non-dedicated scanning proton beamline for ocular treatment at the synchrotron-based CNAO facility. Medical Physics **46** (4), 1852–1862. 48

Clasie, B., Depauw, N., Fransen, M. et al., 2012. Golden beam data for proton pencil-beam scanning. Physics in Medicine and Biology **57** (5), 1147–1158. 37, 62

Coleman, C.N. and Harris, J.R., 1998. Current Scientific Issues Related to Clinical Radiation Oncology. Radiation Research **150** (2), 125. 15

Cortés-Giraldo, M.A. and Carabe, A., 2015. A critical study of different Monte Carlo scoring methods of dose average linear-energy-transfer maps calculated in voxelized

geometries irradiated with clinical proton beams. Physics in Medicine and Biology **60** (7), 2645–2669. 63

Dahle, T.J., Rykkelid, A.M., Stokkevåg, C.H. et al., 2017. Monte Carlo simulations of a low energy proton beamline for radiobiological experiments. Acta Oncologica **56** (6), 779–786. 54, 71

Dollinger, G., 2011. Comment on "Therapeutic application of metallic nanoparticles combined with particle-induced x-ray emission effect". Nanotechnology **22** (24), 248001. 77, 78, 97

Dowdell, S.J., Clasie, B., Depauw, N. et al., 2012. Monte Carlo study of the potential reduction in out-of-field dose using a patient-specific aperture in pencil beam scanning proton therapy. Physics in Medicine and Biology **57** (10), 2829–2842. 15, 28, 49

Ehlert, J., Piel, M., Boege, F. et al., 2021. An experimental platform for studying the radiation effects of laser accelerated protons on mammalian cells. AIP Advances **11** (6), 065208. 55, 71, 72

Favaudon, V., Caplier, L., Monceau, V. et al., 2014. Ultrahigh dose-rate FLASH irradiation increases the differential response between normal and tumor tissue in mice. Science Translational Medicine **6** (245). 55

Favaudon, V., Labarbe, R. and Limoli, C.L., 2021. Model studies of the role of oxygen in the FLASH effect. Medical Physics **49** (3), 2068–2081. 55

Friedland, W., Jacob, P., Bernhardt, P. et al., 2003. Simulation of DNA Damage after Proton Irradiation. Radiation Research **159** (3), 401–410. 17

Galper, M.W., Saung, M.T., Fuster, V. et al., 2012. Effect of Computed Tomography Scanning Parameters on Gold Nanoparticle and Iodine Contrast. Investigative Radiology **47** (8), 475–481. 94

Geant4, 2020. Geant4 A simulation toolkit, Physics Reference Manual. Geant4 Collaboration. 25

Gerken, L.R.H., Gogos, A., Starsich, F.H.L. et al., 2022. Catalytic activity imperative for nanoparticle dose enhancement in photon and proton therapy. Nature Communications **13** (1). 78

Gerlach, S., Pinto, M., Kurichiyanil, N. et al., 2020. Beam characterization and feasibility study for a small animal irradiation platform at clinical proton therapy facilities. Physics in Medicine and Biology **65** (24), 245045. 54

Goodhead, D.T., Belli, M., Mill, A.J. et al., 1992. Direct Comparison between Protons and Alpha-particles of the Same LET: I. Irradiation Methods and Inactivation of Asynchronous V79, HeLa and C3H 10T½ Cells. International Journal of Radiation Biology **61** (5), 611–624. 53

Goodman, S.A., Auret, F.D. and Meyer, W.E., 1994. The effect of alpha-particle and proton irradiation on the electrical and defect properties of n-GaAs. Nuclear Instruments and Methods in Physics Research Section B: Beam Interactions with Materials and Atoms **90** (1-4), 349–353. 67

Gottschalk, B., 2009. On the scattering power of radiotherapy protons. Medical Physics **37** (1), 352–367. 8

Gottschalk, B., 2012. Physics of Proton Interactions in Matter. In: Paganetti, H. (Ed.), Proton Therapy Physics. CRC Press. 7, 8, 9, 10

Goudsmit, S. and Saunderson, J.L., 1940. Multiple Scattering of Electrons. Physical Review **57** (1), 24–29. 8

Granville, D.A. and Sawakuchi, G.O., 2015. Comparison of linear energy transfer scoring techniques in Monte Carlo simulations of proton beams. Physics in Medicine and Biology **60** (14), N283–N291. 63

Grassberger, C., Lomax, A. and Paganetti, H., 2014. Characterizing a proton beam scanning system for Monte Carlo dose calculation in patients. Physics in Medicine and Biology **60** (2), 633–645. 37, 62

Grewal, H.S., Ahmad, S. and Jin, H., 2021. Characterization of penumbra sharpening and scattering by adaptive aperture for a compact pencil beam scanning proton therapy system. Medical Physics **48** (4), 1508–1519. 51

Guan, F., Bronk, L., Titt, U. et al., 2015. Spatial mapping of the biologic effectiveness of scanned particle beams: towards biologically optimized particle therapy. Scientific Reports **5** (1). 54, 69

Hainfeld, J.F., Dilmanian, F.A., Slatkin, D.N. et al., 2008. Radiotherapy enhancement with gold nanoparticles. Journal of Pharmacy and Pharmacology **60** (8), 977–985. 77

Hainfeld, J.F., Slatkin, D.N. and Smilowitz, H.M., 2004. The use of gold nanoparticles to enhance radiotherapy in mice. Physics in Medicine and Biology **49** (18), N309–N315. 76

Hainfeld, J.F., Smilowitz, H.M., O'Connor, M.J. et al., 2013. Gold nanoparticle imaging and radiotherapy of brain tumors in mice. Nanomedicine **8** (10), 1601–1609. 76, 93

Han, X., Xu, K., Taratula, O. et al., 2019. Applications of nanoparticles in biomedical imaging. Nanoscale **11** (3), 799–819. 76, 93

Hanton, F., Chaudhary, P., Doria, D. et al., 2019. DNA DSB Repair Dynamics following Irradiation with Laser-Driven Protons at Ultra-High Dose Rates. Scientific Reports **9** (1). 53

Herrmann, T., Baumann, M. and Dörr, W., 2006. Klinische Strahlenbiologie: Kurz und Bündig. Vol. 4. Elsevier. 16, 17

Heuchel, L., Hahn, C., Pawelke, J. et al., 2022. Clinical use and future requirements of relative biological effectiveness: Survey among all European proton therapy centres. Radiotherapy and Oncology **172**, 134–139. 18

Highland, V.L., 1975. Some practical remarks on multiple scattering. Nuclear Instruments and Methods **129** (2), 497–499. 8

Hong, L., Goitein, M., Bucciolini, M. et al., 1996. A pencil beam algorithm for proton dose calculations. Physics in Medicine and Biology **41** (8), 1305–1330. 29, 30

Hyer, D.E., Hill, P.M., Wang, D. et al., 2014. A dynamic collimation system for penumbra reduction in spot-scanning proton therapy: Proof of concept. Medical Physics **41** (9), 091701. 50

International Atomic Energy Agency (IAEA), 2000. Absorbed Dose Determination in External Beam Radiotherapy. Technical Reports Series No. 398. 23

International Commission on Radiation Units and Measurements, 1993. Stopping Powers and Ranges for Protons and Alpha Particles (Report 49). Journal of the ICRU **os25** (2), NP–NP. 8, 62

International Commission on Radiation Units and Measurements, 2007. Prescribing, Recording, and Reporting Proton-Beam Therapy (Report 78). Journal of the ICRU **7** (2), NP–NP. 14

International Commission on Radiation Units and Measurements, 2014. Key Data For Ionizing-Radiation Dosimetry: Measurement Standards And Applications (Report 90). Journal of the ICRU **14** (1), NP.2–NP. 6, 38, 62

Ion Beam Applications (IBA), 2018. Proton Therapy System - Maintenance Manual. 19, 20

Ipe, N.E., 2012. Basic Aspects of Shielding. In: Paganetti, H. (Ed.), Proton Therapy Physics. CRC Press. 9

Jarlskog, C.Z. and Paganetti, H., 2008. Physics Settings for Using the Geant4 Toolkit in Proton Therapy. IEEE Transactions on Nuclear Science **55** (3), 1018–1025. 38, 62

Jermann, M., 2015. Particle Therapy Statistics in 2014. International Journal of Particle Therapy **2** (1), 50–54. 2

Johny, J., van Halteren, C.E.R., Can-Cakir, F. et al., 2022a. Sensitizer efficiency of ligand-free gold nanoparticles in proton therapy is ruled by surface chemistry and surface area. Journal of Materials Chemistry B - submitted. 79

Johny, J., van Halteren, C.E.R., Zwiehoff, S. et al., 2022b. Impact of Sterilization on the Colloidal Stability of Ligand-Free Gold Nanoparticles for Biomedical Applications. Langmuir **38** (43), 13030–13047. 96

Joiner, M.C., 2009. Quantifying cell kill and cell survival. In: Joiner, M.C. and van der Kogel, A. (Eds.), Basic Clinical Radiobiology. Hodder Arnold. 16

Joint Committee for Guides in Metrology, 2008. Evaluation of measurement data – Guide to the expression of uncertainty in measurement. JCGM **100**. 64

Karsch, L., Beyreuther, E., Passos, D.E. et al., 2019. Analysing Tumour Growth Delay Data from Animal Irradiation Experiments with Deviations from the Prescribed Dose. Cancers **11** (9), 1281. 54

Kern, A., Bäumer, C., Kröninger, K. et al., 2020. Determination of surface dose in pencil beam scanning proton therapy. Medical Physics **47** (5), 2277–2288. 60

Kim, J., Bar-Ness, D., Si-Mohamed, S. et al., 2018. Assessment of candidate elements for development of spectral photon-counting CT specific contrast agents. Scientific Reports **8** (1). 93

Kim, J.K., Seo, S.J., Kim, H.T. et al., 2012. Enhanced proton treatment in mouse tumors through proton irradiated nanoradiator effects on metallic nanoparticles. Physics in Medicine and Biology **57** (24), 8309–8323. 79

Kim, J.K., Seo, S.J., Kim, K.H. et al., 2010. Therapeutic application of metallic nanoparticles combined with particle-induced x-ray emission effect. Nanotechnology **21** (42), 425102. 77

Kimstrand, P., Traneus, E., Ahnesjö, A. et al., 2007. A beam source model for scanned proton beams. Physics in Medicine and Biology **52** (11), 3151–3168. 37

Koska, B. and Wulff, J., 2021. Commissioning of the Eye Treatment System at WPE. 86

Krämer, M. and Durante, M., 2010. Ion beam transport calculations and treatment plans in particle therapy. The European Physical Journal D **60** (1), 195–202. 23

Kroll, F., Brack, F.E., Bernert, C. et al., 2022. Tumour irradiation in mice with a laser-accelerated proton beam. Nature Physics **18** (3), 316–322. 55

Labarbe, R., Hotoiu, L., Barbier, J. et al., 2020. A physicochemical model of reaction kinetics supports peroxyl radical recombination as the main determinant of the FLASH effect. Radiotherapy and Oncology **153**, 303–310. 55

Lacombe, S., Porcel, E. and Scifoni, E., 2017. Particle therapy and nanomedicine: state of art and research perspectives. Cancer Nanotechnology **8** (1). 77, 78

Landau, L.D., 1944. On the energy loss of fast particles by ionization. Journal of Physics **8** (4), 201–205. 12

Langen, K., Polf, J. and Schulte, R., 2015. Imaging for Proton Therapy. In: Das, I.J. and Paganetti, H. (Eds.), Principles and Practice of Proton Beam Therapy. Published for the American Association of Physicists in Medicine by Medical Physics Publishing, Inc. 10

Lawrence, J.H., 1957. Proton irradiation of the pituitary. Cancer **10**, 795–798. 2

Le Sech, C., Kobayashi, K., Usami, N. et al., 2012. Comment on "Enhanced relative biological effectiveness of proton radiotherapy in tumor cells with internalized gold nanoparticles" [Appl. Phys. Lett. **98**, 193702 (2011)]. Applied Physics Letters **100** (2), 026101. 77, 78

Leo, W.R., 1994. Techniques for Nuclear and Particle Physics Experiments: A How-to Approach. Springer Berlin Heidelberg. 8, 9

Lewis, H.W., 1952. Range Straggling of a Nonrelativistic Charged Particle. Physical Review **85** (1). 12

Li, S., Penninckx, S., Karmani, L. et al., 2016. LET-dependent radiosensitization effects of gold nanoparticles for proton irradiation. Nanotechnology **27** (45), 455101. 77, 79, 96

Lomax, A., 2012. Physics of Treatment Planning Using Scanned Beams. In: Paganetti, H. (Ed.), Proton Therapy Physics. CRC Press. 12, 22

Lu, H.M. and Flanz, J., 2012. Characteristics of Clinical Proton Beams. In: Paganetti, H. (Ed.), Proton Therapy Physics. CRC Press. 15

Lühr, A., von Neubeck, C., Krause, M. et al., 2018. Relative biological effectiveness in proton beam therapy – Current knowledge and future challenges. Clinical and Translational Radiation Oncology **9**, 35–41. 18

Maes, D., Regmi, R., Taddei, P. et al., 2019. Parametric characterization of penumbra reduction for aperture-collimated pencil beam scanning (PBS) proton therapy. Biomedical Physics and Engineering Express **5** (3), 035002. 35, 48, 49

Mančić, A., Fuchs, J., Antici, P. et al., 2008. Absolute calibration of photostimulable image plate detectors used as (0.5–20MeV) high-energy proton detectors. Review of Scientfic Instruments **79** (7), 073301. 71

Meier, G., Leiser, D., Besson, R. et al., 2017. Contour scanning for penumbra improvement in pencil beam scanned proton therapy. Physics in Medicine and Biology **62** (6), 2398–2416. 49

Mesbahi, A., 2010. A review on gold nanoparticles radiosensitization effect in radiation therapy of cancer. Reports of Practical Oncology & Radiotherapy **15** (6), 176–180. 77

Metzner, E., Bäumer, C., Behrends, C. et al., 2022. Spectral fiber dosimetry with beryllium oxide for quality assurance in hadron radiation therapy. Journal of Instrumentation **17** (02), P02009. 48

Moignier, A., Gelover, E., Wang, D. et al., 2016. Theoretical Benefits of Dynamic Collimation in Pencil Beam Scanning Proton Therapy for Brain Tumors: Dosimetric and Radiobiological Metrics. International Journal of Radiation Oncology Biology Physics **95** (1), 171–180. 50

Molière, G., 1948. Theorie der Streuung schneller geladener Teilchen II Mehrfach-und Vielfachstreuung. Zeitschrift für Naturforschung A **3** (2), 78–97. 8

Montay-Gruel, P., Acharya, M.M., Petersson, K. et al., 2019. Long-term neurocognitive benefits of FLASH radiotherapy driven by reduced reactive oxygen species. Proceedings of the National Academy of Sciences **116** (22), 10943–10951. 55

Newhauser, W.D. and Zhang, R., 2015. The physics of proton therapy. Physics in Medicine and Biology **60** (8), R155–R209. 5, 8, 9, 10, 11, 12, 23, 24

Organization for Standardization Technical Specification, I., 2008. Nanotechnologies – Terminology and definitions for nano-objects – Nanoparticle, nanofibre and nanoplate. 76

Paganetti, H., 2012. Range uncertainties in proton therapy and the role of Monte Carlo simulations. Physics in Medicine and Biology **57** (11), R99–R117. 11

Paganetti, H., 2016. Proton Beam Therapy. In: Proton Beam Therapy. IOP Publishing. 22

Paganetti, H., Niemierko, A., Ancukiewicz, M. et al., 2002. Relative biological effectiveness (RBE) values for proton beam therapy. International Journal of Radiation Oncology Biology Physics **53** (2), 407–421. 18

Palmans, H., 2015. Proton Beam Interactions: Basic. In: Das, I.J. and Paganetti, H. (Eds.), Principles and Practice of Proton Beam Therapy. Published for the American Association of Physicists in Medicine by Medical Physics Publishing, Inc. 5, 7, 8, 9, 10

Parodi, K., Mairani, A., Brons, S. et al., 2012. Monte Carlo simulations to support start-up and treatment planning of scanned proton and carbon ion therapy at a synchrotron-based facility. Physics in Medicine and Biology **57** (12), 3759–3784. 70

Patel, D., Bronk, L., Guan, F. et al., 2017. Optimization of Monte Carlo particle transport parameters and validation of a novel high throughput experimental setup to measure the biological effects of particle beams. Medical Physics **44** (11), 6061–6073. 54, 69

Pawelke, J., Brand, M., Hans, S. et al., 2021. Electron dose rate and oxygen depletion protect zebrafish embryos from radiation damage. Radiotherapy and Oncology **158**, 7–12. 55

Perl, J., Shin, J., Schümann, J. et al., 2012. TOPAS: An innovative proton Monte Carlo platform for research and clinical applications. Medical Physics **39** (11), 6818–6837. 27

Physikalisch Technische Werkstätten (PTW), 1977. Beschreibung der PTW Extrapolationskammer - 23391. 60

Polf, J.C., Bronk, L.F., Driessen, W.H.P. et al., 2011. Enhanced relative biological effectiveness of proton radiotherapy in tumor cells with internalized gold nanoparticles. Applied Physics Letters **98** (19), 193702. 77

Porcel, E., Liehn, S., Remita, H. et al., 2010. Platinum nanoparticles: a promising material for future cancer therapy? Nanotechnology **21** (8), 085103. 79

Raschke, S., Spickermann, S., Toncian, T. et al., 2016. Ultra-short laser-accelerated proton pulses have similar DNA-damaging effectiveness but produce less immediate nitroxidative stress than conventional proton beams. Scientific Reports **6** (1). 53, 55, 57, 58, 72

Rogers, D.W.O., 2006. Fifty years of Monte Carlo simulations for medical physics. Physics in Medicine and Biology **51** (13), R287–R301. 25

Roth, M. and Schollmeier, M., 2016. Ion Acceleration – Target Normal Sheath Acceleration. CERN Yellow Reports **1**, 231 – 270. 54

Rudd, M.E., Kim, Y.K., Madison, D.H. et al., 1992. Electron production in proton collisions with atoms and molecules: energy distributions. Reviews of Modern Physics **64** (2), 441–490. 7

Rutherford, E., 1911. The scattering of α and β particles by matter and the structure of the atom. The London, Edinburgh, and Dublin Philosophical Magazine and Journal of Science **21** (125), 669–688. 7

Sabbas, A.M., Jette, D., Rozenfeld, M. et al., 1987. Collimated electron beams and their associated penumbra widths. Medical Physics **14** (6), 996–1006. 29, 30

Safai, S., Bortfeld, T. and Engelsman, M., 2008. Comparison between the lateral penumbra of a collimated double-scattered beam and uncollimated scanning beam in proton radiotherapy. Physics in Medicine and Biology **53** (6), 1729–1750. 15, 27, 28, 29, 30

Sanchez-Parcerisa, D., Sanz-García, I., Ibáñez, P. et al., 2021. Radiochromic film dosimetry for protons up to 10 MeV with EBT2, EBT3 and unlaminated EBT3 films. Physics in Medicine and Biology **66** (11), 115006. 71

Scher, N., Bonvalot, S., Tourneau, C.L. et al., 2020. Review of clinical applications of radiation-enhancing nanoparticles. Biotechnology Reports **28**, e00548. 76

Schilling, I., Bäcker, C.M., Bäumer, C. et al., 2022a. Measuring the Beam Energy in Proton Therapy Facilities Using ATLAS IBL Pixel Detectors. Instruments **6** (4), 80. 83, 110

Schilling, I., Bäcker, C.M., Bäumer, C. et al., 2022b. Characterization of pixelated silicon detectors for daily quality assurance measurements in proton therapy. Journal of Physics: Conference Series **2374** (1), 012178. 48, 83, 110

Schippers, M., 2012. Proton Accelerators. In: Paganetti, H. (Ed.), Proton Therapy Physics. CRC Press. 19, 20

Schippers, M., 2015. Proton Beam Production and Dose Delivery Techniques. In: Das, I.J. and Paganetti, H. (Eds.), Principles and Practice of Proton Beam Therapy. Published for the American Association of Physicists in Medicine by Medical Physics Publishing, Inc. 20, 54

Schlathölter, Lacombe, S., Eustache, P. et al., 2016. Improving proton therapy by metal-containing nanoparticles: nanoscale insights. International Journal of Nanomedicine **11**, 1549–1556. 79

Schlegel, W., Karger, C.P. and Jäkel, O. (Eds.), 2018. Medizinische Physik. Springer Berlin Heidelberg. 1

Schneider, T., Patriarca, A. and Prezado, Y., 2019. Improving the dose distributions in minibeam radiation therapy: Helium ions vs protons. Medical Physics **46** (8), 3640–3648. 53

Schuemann, J., Bagley, A.F., Berbeco, R. et al., 2020. Roadmap for metal nanoparticles in radiation therapy: current status, translational challenges, and future directions. Physics in Medicine and Biology **65** (21), 21RM02. 75, 76, 77, 100

Sicard-Roselli, C., Brun, E., Gilles, M. et al., 2014. A New Mechanism for Hydroxyl Radical Production in Irradiated Nanoparticle Solutions. Small **10** (16), 3338–3346. 78, 79, 95

Silvestri, A., Zambelli, V., Ferretti, A.M. et al., 2016. Design of functionalized gold nanoparticle probes for computed tomography imaging. Contrast Media and Molecular Imaging **11** (5), 405–414. 76, 93

Slopsema, R.L., Mamalui, M., Zhao, T. et al., 2013. Dosimetric properties of a proton beamline dedicated to the treatment of ocular disease. Medical Physics **41** (1), 011707. 18

Smeets, J., Roellinghoff, F., Prieels, D. et al., 2012. Prompt gamma imaging with a slit camera for real-time range control in proton therapy. Physics in Medicine and Biology **57** (11), 3371–3405. 10

Smith, B., Gelover, E., Moignier, A. et al., 2016. Technical Note: A treatment plan comparison between dynamic collimation and a fixed aperture during spot scanning proton therapy for brain treatment. Medical Physics **43** (8), 4693–4699. 51

Smith, C.L., Best, S.P., Gagliardi, F. et al., 2017. The effects of gold nanoparticles concentrations and beam quality/LET on dose enhancement when irradiated with X-rays and protons using alanine/EPR dosimetry. Radiation Measurements **106**, 352–356. 79

Sorriaux, J., Kacperek, A., Rossomme, S. et al., 2013. Evaluation of Gafchromic® EBT3 films characteristics in therapy photon, electron and proton beams. Physica Medica **29** (6), 599–606. 37

Tian, L., Hahn, C. and Lühr, A., 2022. An ion-independent phenomenological relative biological effectiveness (RBE) model for proton therapy. Radiotherapy and Oncology **174**, 69–76. 54

Titt, U., Zheng, Y., Vassiliev, O.N. et al., 2007. Monte Carlo investigation of collimator scatter of proton-therapy beams produced using the passive scattering method. Physics in Medicine and Biology **53** (2), 487–504. 51

Tobias, C.A., Lawrence, J.H., Born, J.L. et al., 1958. Pituitary Irradiation with High-Energy Proton Beams: A Preliminary Report. Cancer Research **18**, 121–134. 2

Tominaga, Y., Sakurai, Y., Miyata, J. et al., 2022. Validation of pencil beam scanning proton therapy with multi-leaf collimator calculated by a commercial Monte Carlo dose engine. Journal of Applied Clinical Medical Physics. 28

Trinkl, S., Mares, V., Englbrecht, F.S. et al., 2017. Systematic out-of-field secondary neutron spectrometry and dosimetry in pencil beam scanning proton therapy. Medical Physics **44** (5), 1912–1920. 72

Tschalär, C., 1968. Straggling distributions of extremely large energy losses. Nuclear Instruments and Methods **64**, 237–243. 13

Tschalär, C. and Maccabee, H.D., 1970. Energy-Straggling Measurements of Heavy Charged Particles in Thick Absorbers. Physical Review B **1** (7). 13, 69

Ueno, K., Matsuura, T., Hirayama, S. et al., 2019. Physical and biological impacts of collimator-scattered protons in spot-scanning proton therapy. Journal of Applied Clinical Medical Physics **20** (7), 48–57. 51

Usami, N., Furusawa, Y., Kobayashi, K. et al., 2005. Fast He^{2+} ion irradiation of DNA loaded with platinum-containing molecules. International Journal of Radiation Biology **81** (7), 515–522. 77, 79

Usami, N., Furusawa, Y., Kobayashi, K. et al., 2008. Mammalian cells loaded with platinum-containing molecules are sensitized to fast atomic ions. International Journal of Radiation Biology **84** (7), 603–611. 77, 79

van Goethem, M.J., van der Meer, R., Reist, H.W. et al., 2009. Geant4 simulations of proton beam transport through a carbon or beryllium degrader and following a beam line. Physics in Medicine and Biology **54** (19), 5831–5846. 70

van Luijk, P., van 't Veld, A.A., Zelle, H.D. et al., 2001. Collimator scatter and 2D dosimetry in small proton beams. Physics in Medicine and Biology **46** (3), 653–670. 51

Verbeek, N., Wulff, J., Bäumer, C. et al., 2020. Single pencil beam benchmark of a module for Monte Carlo simulation of proton transport in the PENELOPE code. Medical Physics **48** (1), 456–476. 37, 62

Vilches-Freixas, G., Unipan, M., Rinaldi, I. et al., 2020. Beam commissioning of the first compact proton therapy system with spot scanning and dynamic field collimation. The British Journal of Radiology **93** (1107), 20190598. 51

Waag, F., Streubel, R., Gökce, B. et al., 2021. Synthesis of gold, platinum, and gold-platinum alloy nanoparticle colloids with high-power megahertz-repetition-rate lasers: the importance of the beam guidance method. Applied Nanoscience **11** (4), 1303–1312. 80

Wälzlein, C., Scifoni, E., Krämer, M. et al., 2014. Simulations of dose enhancement for heavy atom nanoparticles irradiated by protons. Physics in Medicine and Biology **59** (6), 1441–1458. 78, 79, 95

Wang, D., Dirksen, B., Hyer, D.E. et al., 2014. Impact of spot size on plan quality of spot scanning proton radiosurgery for peripheral brain lesions. Medical Physics **41** (12), 121705. 51

Wang, D., Smith, B.R., Gelover, E. et al., 2015. A method to select aperture margin in collimated spot scanning proton therapy. Physics in Medicine and Biology **60** (7), N109–N119. 15, 28, 51

Weber, U. and Kraft, G., 2009. Comparison of Carbon Ions Versus Protons. The Cancer Journal **15** (4), 325–332. 53

Wilks, S.C., Langdon, A.B., Cowan, T.E. et al., 2001. Energetic proton generation in ultra-intense laser–solid interactions. Physics of Plasmas **8** (2), 542–549. 54

Wilson, R.R., 1946. Radiological Use of Fast Protons. Radiology **47** (5), 487–491. 1

Winterhalter, C., Lomax, A., Oxley, D. et al., 2018. A study of lateral fall-off (penumbra) optimisation for pencil beam scanning (PBS) proton therapy. Physics in Medicine and Biology **63** (2), 025022. 15, 27, 28, 39, 49

Wulff, J., 2010. Clinical dosimetry in photon radiotherapy A Monte Carlo based investigation. Ph.D. thesis, Philipps University Marburg. 25

Wulff, J., Baumann, K.S., Verbeek, N. et al., 2018. TOPAS/Geant4 configuration for ionization chamber calculations in proton beams. Physics in Medicine and Biology **63** (11), 115013. 38

Wulff, J., Koska, B., Heufelder, J. et al., 2023. Commissioning and validation of a novel commercial TPS for ocular proton therapy. Medical Physics **50** (1), 365–379. 21

Zeng, X., Sun, J., Li, S. et al., 2020. Blood-triggered generation of platinum nanoparticle functions as an anti-cancer agent. Nature Communications **11** (1), 567. 96

Zhang, R. and Newhauser, W.D., 2009. Calculation of water equivalent thickness of materials of arbitrary density, elemental composition and thickness in proton beam irradiation. Physics in Medicine and Biology **54** (6), 1383–1395. 23, 24, 59, 60

Zwiehoff, S., Johny, J., Behrends, C. et al., 2021. Enhancement of Proton Therapy Efficiency by Noble Metal Nanoparticles Is Driven by the Number and Chemical Activity of Surface Atoms. Small **18**, 2106383. 79, 80, 96, 97, 108

Danksagung

An dieser Stelle möchte ich all denen herzlich danken, die mich während meiner Promotion in unterschiedlichster Form unterstützt haben.
Besonders möchte ich mich bei meinem Doktorvater PD Dr. Christian Bäumer für die Ermöglichung der Mitarbeit an diesen interessanten Projekten, die Möglichkeit der Mitgestaltung der Themen und seine allzeitige Unterstützung bedanken. Ich konnte mich bei allen Fragestellungen stets an ihn wenden und habe viel fachlich und im Bereich des wissenschaftlichen Arbeitens von ihm gelernt. Mein herzlicher Dank gilt außerdem Jun.-Prof. Dr. Armin Lühr, der mich nach seinem Wechsel nach Dortmund seitens der TU betreut hat und mit dem ich strahlenbiologische Fragestellungen immer diskutieren konnte.
Darüber hinaus gilt ein großes Dankeschön Prof. Dr. Kevin Kröninger, der mich gerade zu Beginn meiner Promotion an der TU als organisatorischer Ansprechpartner in vielen Aspekten unterstützt hat. Er hat mir das Gefühl gegeben, als externe Doktorandin in seiner Arbeitsgruppe jederzeit willkommen zu sein. Er ermöglichte mir außerdem die Nutzung seines Rechenclusters für die Monte-Carlo-Simulationen. An dieser Stelle möchte ich mich herzlich bei der gesamten AG Kröninger des Instituts E4 für die Berücksichtigung und die Hilfe bei technischen Problemen bedanken.
Außerdem möchte ich mich bei der Klinikleitung Prof. Dr. Beate Timmermann für die Möglichkeiten der Forschung am WPE bedanken. Ein Dankeschön gilt allen Kollegen und Kolleginnen der Physik-Gruppe inklusiv der feinmechanischen Werkstatt des WPE. Besonders möchte ich mich bei Dr. Jörg Wulff und Dr. Maximilian Bäcker für einen stets regen Austausch der Forschungsthemen und für kritische Anmerkungen und Korrekturen in meinen Publikationen und dieser Dissertation bedanken. Weiterhin möchte ich meinen ehemaligen Doktorandenkollegen Dr. Nico Verbeek und Ajvar Kern für die Hilfe bei meinen anfänglichen Fragestellungen danken. Nico danke ich besonders für seine Hilfe und die Bereitstellung der Phasenraumparameter des WPE Protonenstrahls für die Quellen der TOPAS-Simulationen. Den derzeitigen Doktorandenkollegen Feline Heinzelmann und Johannes Esser möchte ich für die informativen Meetings und den gemeinsamen Austausch danken. Johannes danke ich besonders für das Korrekturlesen und die Unterstützung bei den Filmmessungen. Feline danke ich für die regelmäßigen

Spaziergänge in der Pause zum Quatschen und Kraft tanken.
Bei Dr. David Offenberg bedanke ich mich ebenfalls für die hilfreichen Kommentare zu dieser Arbeit.
Außerdem bin ich dankbar, dass ich Teil des Graduiertenkollegs *MERCUR-GK Präzisionsprotonentherapie* sein durfte, das viele inhaltliche Facetten und dauerhaft die Möglichkeit eines effizienten Austauschs geboten hat. Ich möchte mich bei allen Beteiligten des GKs bedanken, die mich während der gesamten Promotionsphase begleitet und motiviert haben. Ein Dank gilt allen Doktoranden für die angenehmen Abende im privaten Rahmen sowie für die gesamte Zeit, aus der auch Freundschaften entstanden sind. An dieser Stelle möchte ich besonders Isabelle Schilling, Sandra Zwiehoff und Maximilian Bäcker für den regen Austausch und den Spaß bei den Strahlzeiten mit erfolgreichen Messungen danken.
Außerdem möchte ich der AG von Prof. Dr. Oswald Willi der Heinrich-Heine-Universität Düsseldorf und insbesondere Dr. Jens Ehlert für die Zusammenarbeit im Bereich der Laser-beschleunigten Protonen des Projekts *micro* danken. Das Projekt *nano* zeichnet sich besonders durch die erfolgreiche Zusammenarbeit der verschiedenen Arbeitsgruppen aus: Dazu beigetragen haben Prof. Dr. Kevin Kröninger, Dr. Jens Weingarten und Isabelle Schilling mit den Pixeldetektormessungen und Prof. Dr.-Ing. Stephan Barcikowski, Dr. Christoph Rehbock und Sandra Zwiehoff mit den chemischen Analysen sowie der Herstellung der Platinnanopartikelproben.
Ich danke all meinen Freunden, besonders meinen Mädels, für viel Rückhalt und Ablenkung in dieser anstrengenden Lebensphase.
Herzlich danke ich meinen Eltern und meiner Schwester für die Rücksichtnahme in arbeitsintensiven Zeiten und Unterstützung zu jeder Zeit. Christian, dir danke ich ganz besonders für die ununterbrochene Stärkung jeglicher Art, die Motivationsreden, das Verständnis und die Ablenkung in stressigen Momenten. Danke dir für alles!

Publications related to this work

- **Behrends, C.**, Bäumer, C., Verbeek, N., Ehlert, J., Prasad, R., Wulff, J., Lühr, A., Timmermann, B., 2021. Technical note: Providing proton fields down to the few-MeV level at clinical pencil beam scanning facilities for radiobiological experiments. *Medical Physics* **49** (1), 666–674.

- **Behrends, C.**, Bäcker, C. M., Schilling, I., Zwiehoff, S., Weingarten, J., Kröninger, K., Rehbock, C., Barcikowski, S., Wulff, J., Bäumer, C., Timmermann, B., 2022. The radiosensitizing effect of platinum nanoparticles in proton irradiations is not caused by an enhanced proton energy deposition at the macroscopic scale. *Physics in Medicine and Biology* **67** (15), 155023.

- **Behrends, C.**, Bäumer, C., Verbeek, N., Wulff, J., Timmermann, B., 2023. Optimization of proton pencil beam positioning in collimated fields. *Medical Physics, accepted and online available*

- Zwiehoff, S., Johny, J., **Behrends, C.**, Landmann, A., Mentzel, F., Bäumer, C., Kröninger, K., Rehbock, C., Timmermann, B., Barcikowski, S., 2021. Enhancement of Proton Therapy Efficiency by Noble Metal Nanoparticles Is Driven by the Number and Chemical Activity of Surface Atoms. *Small* **18**, 2106383.

- Schilling, I., Bäcker, C. M., Bäumer, C., **Behrends, C.**, Kröninger, K., Timmermann, B., Weingarten, J., 2022. Characterization of pixelated silicon detectors for daily quality assurance measurements in proton therapy. *Journal of Physics: Conference Series* **2374** (1), 012178.

- Schilling, I., Bäcker, C. M., Bäumer, C., **Behrends, C.**, Hötting, M., Hohmann, J., Kröninger, K., Timmermann, B., Weingarten, J., 2022. Measuring the Beam Energy in Proton Therapy Facilities Using ATLAS IBL Pixel Detectors. *Instruments* **6** (4), 80.

- Metzner, E., Bäumer, C., **Behrends, C.**, Debbih, A. D., Döhler, D. D., van Goethem, M. J., van der Graaf, E. R., Kahle, P., Lühr, A., Teichmann, T., Timmermann, B.,Weinberger, D., Werner, T., Wulff, J., Kormoll, T., 2022. Spectral fiber

dosimetry with beryllium oxide for quality assurance in hadron radiation therapy. *Journal of Instrumentation* **17** (02), P02009.

- ▷ Johny, J., van Halteren, C. E. R., Zwiehoff, S., **Behrends, C.**, Bäumer, C., Timmermann, B., Rehbock, C., Barcikowski, S., 2022. Impact of Sterilization on the Colloidal Stability of Ligand-Free Gold Nanoparticles for Biomedical Applications. *Langmuir* **38** (43), 13030–13047.

- ▷ Johny, J., van Halteren, C. E. R., Can-Cakir, F., Zwiehoff, S., **Behrends, C.**, Bäumer, C., Timmermann, B., Rauschenbach, L., Tippelt, S., Scheffler, B., Schramm, A., Rehbock, C., Barcikowski, S., 2022. Sensitizer efficiency of ligand-free gold nanoparticles in proton therapy is ruled by surface chemistry and surface area. *Journal of Materials Chemistry B*, *submitted*

- ▷ Kretschmer, J., Brodbek, L., **Behrends, C.**, Kugel, F., Koska, B., Bäumer, C., Wulff, J., Timmermann, B., Poppe, B., Looe, H. K., 2022. Comprehensive investigation of lateral dose profile and output factor measurements in small proton fields from different delivery techniques. *Medical Physics, accepted and online available*

- ▷ Kugel, F., Wulff, J., Bäumer, C., Janson, M., Kretschmer, J., Brodbek, L., **Behrends, C.**, Verbeek, N., Looe, H. K., Poppe, B., Timmermann, B., 2022. Validating a double Gaussian source model for small proton fields in a commercial Monte-Carlo dose calculation engine. *Zeitschrift für Medizinische Physik, accepted and in press*

- ▷ Wulff, J., Koska, B., Heufelder, J., Janson, M., Bäcker, C. M., Siregar, H., **Behrends, C.**, Bäumer, C., Foerster, A., Bechrakis, N. E., Timmermann, B., 2022. Commissioning and validation of a novel commercial TPS for ocular proton therapy. *Medical Physics* **50** (1), 365–379.

Conference contribution of this thesis

- ▷ **Behrends, C.**, Bäcker, C. M., Schilling, I., Zwiehoff, S., Weingarten, J., Kröninger, K., Rehbock, C., Barcikowski, S., Wulff, J., Bäumer, C., Timmermann, B., Is the Radiosensitizing Effect of Platinum Nanoparticles in Proton Irradiation Due to An Enhanced Proton Energy Deposition? *American Association of Physicists in Medicine*. 64th Annual Meeting, Washington DC, 2022 (talk).